Université de Montréal

Development of MRI pulse sequences for the investigation of fMRI contrasts

Par

Marius Tuznik

Institut de Génie Biomédical, Département de physiologie,

Faculté des études supérieures

Mémoire présenté à la Faculté des études supérieures en vue de l'obtention du grade de maîtrise en sciences appliquées en génie biomédical

Août 2016

Abstract

Magnetic resonance imaging (MRI) is an important tool for the qualitative and quantitative investigation of brain physiology. The investigation of neuronal activation using this modality is made possible by the detection of concomitantly-arising hemodynamic changes in the brain's vasculature, such as localized increases of the cerebral blood flow (CBF) or the variation of the concentration of paramagnetic deoxyhemoglobin in venous vessels. To study the formation of functional contrasts that stem from these changes in MRI, two pulse sequences were developed in this thesis to carry out experiments in blood oxygenation level dependent (BOLD) and perfusion functional MRI (fMRI).

The first objective laid out in this work was the development of an echo planar imaging (EPI) sequence permitting the interleaved acquisition of images using gradient-echo EPI and spin-echo EPI to assess the performances of these imaging techniques in a BOLD fMRI experiment involving a visual stimulation paradigm in 4 healthy adult subjects. The second main objective of this thesis was the development of a pseudo-continuous arterial spin labelling (pCASL) sequence for the quantification of cerebral blood flow (CBF) at rest. This sequence was tested on 3 healthy adult subjects and compared to an externally-developed pCASL sequence to assess its performance.

The results of the BOLD fMRI experiment indicated that the performance of GRE-EPI was superior to that of SE-EPI in terms of the average percent effect size and t-score associated with stimulus-driven neuronal activation. The CBF quantification experiment demonstrated the ability of the in-house pCASL sequence to compute values of CBF that are within a range of physiologically-acceptable values while remaining inferior to those computed using the externally-developed pCASL sequence. Future experiments will focus on the optimization of the sequences presented in this thesis as well as on the quantification of the pCASL sequence's labelling efficiency.

Keywords: Pulse sequence design, functional MRI, Arterial spin labelling, gradient-echo and spin-echo, blood oxygenation level-dependent (BOLD) contrast

Résumé

L'imagerie par résonance magnétique (IRM) est un outil important pour l'investigation qualitative et quantitative de la physiologie du cerveau. L'investigation de l'activité neuronale à l'aide de cette modalité est possible grâce à la détection de changements hémodynamiques qui surviennent de manière concomitante aux activités de signalisation des neurones, tels l'augmentation régionale du débit sanguin cérébral (CBF) ou encore la variation de la concentration de désoxyhémoglobine dans les vaisseaux veineux. Pour étudier la formation de contrastes fonctionnels qui découlent de ces phénomènes, deux séquences de pulses ont été développées en vue d'expériences en IRM fonctionnelle (IRMf) visant l'imagerie du signal oxygéno-dépendant BOLD ainsi que de la perfusion.

Le premier objectif de cette thèse fut le développement d'une séquence de type écho-planar (EPI) permettant l'acquisition entrelacée d'images en mode échos de gradient (GRE-EPI) ainsi qu'en mode échos de spins (SE-EPI) pour l'évaluation de la performance de ces deux méthodes d'imagerie au cours d'une expérience en IRMf BOLD impliquant l'utilisation d'un stimulus visuel chez 4 sujets adultes sains. Le deuxième objectif principal de cette thèse fut le développement d'une séquence de marquage de spins artériels employant un module de marquage fonctionnant en mode pseudo-continu (pCASL) pour la quantification du CBF au repos. Cette séquence fut testée chez 3 sujets adultes en bonne santé et sa performance fut comparée à celle d'une séquence similaire développée par un groupe de recherche extérieur.

Les résultats de l'expérience portant sur le contraste BOLD indiquent une supériorité de la performance du mode GRE-EPI vis-à-vis celle du mode SE-EPI en termes des valeurs moyennes du pourcentage de l'ampleur d'effet et du score *t* associés à l'activité neuronale en réponse au stimulus. L'expérience visant la quantification du CBF démontra la capacité de la séquence pCASL développée au cours de ce projet de calculer des valeurs de la perfusion de la matière grise ainsi que du cerveau entier se retrouvant dans une plage de valeurs qui sont physiologiquement acceptables, mais qui demeurent inférieures à celles obtenues par la séquence pCASL développée par le groupe de recherche extérieur. Des expériences futures seront effectuées pour optimiser le fonctionnement des séquences présentées dans ce mémoire en plus de quantifier l'efficacité d'inversion de la séquence pCASL.

Mots-clés : Développement de séquences de pulses, IRM fonctionnelle, marquage de spins artériels, échos de gradient et échos de spins, contraste oxygéno-dépendent BOLD

Table of contents

List of figures

List of tables

List of abbreviations

AAPM:	American Association of Medical Physicists
AC-PC:	Anterior commissure – Posterior commissure
ACR:	American College of Radiology
ADC:	Analog-to-digital converter
ASL:	Arterial spin labelling
ATP:	Adenosine triphosphate
BET:	Brain extraction tool
BOLD:	Blood oxygen level-dependent
CASL:	Continuous arterial spin labelling
CBF:	Cerebral blood flow
CBV:	Cerebral blood volume
CMR_{glu}:	Cerebral metabolic rate of glucose
$CMRO_2$:	Cerebral metabolic rate of oxygen
CNR:	Contrast-to-noise ratio
DSC:	Dynamic susceptibility contrast
EPI:	Echo planar imaging
EPISTAR:	Echo planar imaging and signal targeting with alternative radiofrequency
FAIR:	Flow-sensitive alternating inversion recovery
FAST:	FMRIB's automatic segmentation tool
FID:	Free induction decay
FLASH:	Fast low angle shot
fMRI:	Functional magnetic resonance imaging
FWHM:	Full width at half-maximum
GRE:	Gradient-recalled echo
MPRAGE:	Magnetization-prepared rapid gradient echo
MRI:	Magnetic resonance imaging
PASL:	Pulsed arterial spin labelling
pCASL:	Pseudo-continuous arterial spin labelling
PICORE:	Proximal inversion with a control for off-resonance effects
PLD:	Post-label delay
Q2TIPS:	QUIPSS II with thin-slice TI_1 periodic saturation
QUIPSS II:	Quatitative imaging of perfusion using a single subtraction
RF:	Radiofrequency
ROI:	Region of interest
SAR:	Specific absorption rate
SE:	Spin-echo
SLR:	Shinnar-LeRoux
SNR:	Signal-to-noise ratio
SWI:	Susceptibility-weighted imaging
T:	Tesla
T1:	Longitudinal relaxation time
T2:	Transverse relaxation time
T2*:	Effective transverse relaxation time
TE:	Echo time
TI:	Inversion time
TR:	Repetition time

Introduction

Due to its ability to non-invasively produce high-resolution images of the human body with multiple types of contrasts in order to visualize biological structures of interest, magnetic resonance imaging (MRI) is often considered as one of the most important diagnostic tools in the field of medicine. However, its use is not restricted to anatomical imaging; discoveries made in the early 1990s have made it possible to use this modality to qualitatively and quantitatively probe brain physiology. (Ogawa *et al*, 1993) Numerous biological and physical phenomena in the human body make the detection of neuronal activity in the brain using MRI possible, such as neurovascular coupling, functional hyperemia and the changing magnetic properties of hemoglobin, the latter of which depend on the oxygenation state of this protein. These phenomena all contribute to the generation of what is known as blood oxygenation level-dependent or "BOLD" contrast in MRI. (Huettel *et al,* 2014)

During periods of brain activity, neurons will generate bioelectrical signals known as action potentials in order to engage in information processing and cell signalling. (Marieb, 2005) The creation of these signals will trigger molecular cascades that culminate in the release of factors that act upon the smooth muscle cells surrounding blood vessels proximal to the site of increased synaptic activity in an effort to regulate regional blood flow in the cerebral cortex. (Atwell *et al*, 2010) The net effect of this regulatory process is a large increase in cerebral blood flow towards the region of neuronal activation, a physiological process also known as functional hyperemia, as well as increases in the cerebral metabolic rates of glucose and oxygen consumption, which denote the utilization of nutrients necessary for cellular respiration and the production of adenosine triphosphate by neurons. The latter step ensures the continuation of signalling activities carried out by these cells. (Kim *et al*, 2006)

However, a quantity of oxygen that far surpasses the metabolic needs of the neurons is delivered to brain parenchyma at this time. (Fox *et al*, 1986) This phenomenon arises due to functional hyperemia and is responsible for driving out deoxyhemoglobin from the venous vasculature during periods of neuronal activation. This is of profound importance in functional magnetic resonance imaging (fMRI) as the differences between the magnetic properties of deoxygenated hemoglobin and the surrounding parenchymal tissue will generate magnetic field

distortions both in and around the blood vessels, which are in turn responsible for a hastened regional decay of MRI signal. (Kim *et al*, 2006) As deoxyhemoglobin is replaced by its oxygenated counterpart, the size of these distortions will get smaller and the longevity of regional MRI signal will increase, which translates to an increase of signal intensity at this location on the final image. This relationship between blood oxygen content and signal intensity is what gives the BOLD contrast its name.

Many different imaging techniques can be used to acquire images presenting BOLD contrast with fast imaging techniques such as echo planar imaging (EPI) being widely utilized due to the need for rapid collection of functional data. In particular, gradient-echo EPI (GRE-EPI) stands out as a particularly viable imaging method in BOLD fMRI due to its sensitivity to the field distortions generated by the presence of paramagnetic magnetic field perturbers such as deoxyhemoglobin. However, GRE-EPI will detect signal variations associated with fluctuations of the concentration of this protein in all types of blood vessels, from capillaries to large draining veins. (Harmer *et al*, 2012) This reduces its spatial specificity as it is accepted that only changes that take place in the microvasculature are specific to the sites of neuronal activity.

To tackle this issue, spin-echo EPI (SE-EPI) has been proposed as an alternative technique for BOLD fMRI experiments. This technique employs a radiofrequency pulse that eliminates the effects of magnetic field distortions around large vessels while still remaining sensitive to variations of deoxyhemoglobin levels in the microvasculature. This is due to the different molecular mechanisms implicated in the deoxyhemoglobin-mediated signal decay at two different scale sizes. The elimination of these effects, however, reduces the sensitivity of SE-EPI to BOLD signal as the changes in signal intensity arising from the capillaries are smaller than those generated by large vessels in the venous vasculature. (Budde *et al*, 2014)

Perfusion imaging can also be employed as an alternative to BOLD fMRI to detect neuronal activity in the cerebral cortex due to the relationship of linear proportionality between blood flow and the cerebral metabolic rate of glucose. (Faro *et al*, 2011) Arterial spin labelling (ASL) is commonly employed for this purpose and its mode of operation rests on the use of radiofrequency pulses to invert the magnetization of flowing blood water in the brain's feeding arteries in the neck and acquiring an image of the brain after a short delay to allow this tagged volume of blood to diffuse into the brain's extravascular space. (Wong, 2014)

A second measurement of the brain is subsequently acquired without blood tagging and the pairwise subtraction of these two images results in a difference in the magnetization which is proportional to the value of blood flow. ASL can be implemented in either a pulsed or continuous configuration, (PASL and CASL) depending on whether a long RF pulse is used to continuously invert blood water through a flow-driven process or if a short RF pulse is employed to tag all of the blood water in a given volume proximal to the imaging region. (Alsop *et al*, 2015) Recently, ASL sequences featuring a pseudo-continuous tagging mechanism have also been developed in order to combat the disadvantages associated with both PASL and CASL while conserving each technique's respective advantages. The pCASL sequence tags blood water using a flow-driven process similar to CASL in which the long radiofrequency pulse is replaced by a train of shorter and equally-spaced tagging pulses. (Wu *et al*, 2007; Dai *et al*, 2008)

In this thesis, two MRI pulse sequences were developed in order to study the generation of BOLD contrast using GRE-EPI and SE-EPI as well as to perform perfusion imaging in humans at rest. The first of these two sequences was an EPI sequence permitting the interleaved acquisition of functional data using both GRE-EPI and SE-EPI (GRESE-EPI) during a single scan session while the second was a pCASL pulse sequence operating in an unbalanced configuration. To validate the functionality of the GRESE-EPI sequence developed herein and to compare the performances of both types of EPI presented in this introduction, it was deployed in the context of a BOLD fMRI experiment involving a visual stimulation paradigm using optimal and matched echo times for both acquisition techniques. The assessment of the pCASL sequence's functionality was accomplished through a CBF quantification experiment in which values of blood flow were calculated in gray matter, white matter and in the whole brain in healthy adults at rest. These values were then compared to those obtained using an externally-developed pCASL sequence during the same scan session. This sequence was considered as a "gold standard" due to its proven efficacy in perfusion experiments carried out in vivo. (Tancredi *et al*, 2015) Other steps taken to design the pulse sequences described in this thesis, such as the design of radiofrequency pulses for combined GRE and SE imaging, as well as the steps taken to develop the tools needed for data analysis, such as the generation of cerebral venograms using susceptibility-weighted imaging for the evaluation of BOLD signal generation in the venous vasculature, will be presented in this thesis.

Chapter 1. Theoretical framework

In this chapter, the theoretical notions underpinning the phenomena central to this thesis will be introduced and explained in three sections. The first of these will be devoted to the particle physics that make magnetic resonance imaging (MRI) possible. In the second section, the processes by which images are created using MRI, such as slice selection, spatial encoding of MRI signals, creation of signal echoes and contrast generation, will be subject to exposition. In the third and final section, the topic of functional MRI (fMRI) will be broached. Two functional contrasts, perfusion contrast and blood oxygenation level-dependent (BOLD) contrast, will be studied in addition to commonly used imaging techniques employed in experiments in which these types of activation signals are studied.

1.1 Particle physics

MRI chiefly rests on the excitation of biological tissues placed in a strong magnetic field using radiofrequency (RF) waves. These RF pulses will perturb the orientation of protons in said tissues and this excitation process is responsible for signal generation. This signal will then be detected using a receiver coil as an induced electromotive force. Many other factors are involved in the imaging process, but before delving into their specifics, it is necessary to present the fundamental characteristics of atoms suitable for use in MRI as well as how they interact with various magnetic fields at the atomic and molecular levels.

1.1.1 Spin angular momentum and magnetic moment

Hydrogen H^1 atoms, referred to as protons in this work, are the main source of MRI signal in conventional body scans. This is due to its abundance in biological tissues, appearing in the form of water molecules. However, many other elements can be targeted in the context of MRI or magnetic resonance spectroscopy (MRS) experiments, such as fluorine ^{19}F, phosphorus ^{31}P and even sodium ^{23}Na, in order to achieve a better understanding of various physiological

processes involved in homeostasis as well as in various pathologies. (Ruiz-Cabello *et al*, 2011; Ouwerkerk, 2011; Sabouri, 2014)

Not every atom can be targeted using MRI or MRS. Only atoms whose nuclei are made up of an odd number of either protons or neutrons exhibit the necessary properties which make them viable for these experiments. Specifically, the composition of an atom's nucleus will determine whether or not the atom possesses spin angular momentum. This quantity is represented by S in equation 1.1:

$$S = \left(\frac{h}{2\pi}\right) m_s \tag{1.1}$$

In the equation above, h represents Planck's constant and m_s designates a quantum number which represents the atom's spin state. For protons and neutrons, m_s can take one of two values: ± ½. For atoms whose nuclei contain an even number of both nucleons, the values of m_s taken by all protons and neutrons will cancel out, bestowing upon the atom a net angular momentum of zero ($S = 0$.) This consequently prevents the element's use in MRI.

Protons, due to their electric charge and their non-null spin angular momentum, also possess a magnetic moment. This quantity, usually represented by μ, can be expressed as the product of S and the gyromagnetic ratio, γ:

$$\mu = \gamma S \tag{1.2}$$

The gyromagnetic ratio is a constant unique to every atom and is equal to 42.58 MHz/T for hydrogen ^{1}H. Due to their angular momentum, protons are also referred to as "spins" or "water spins" in the context of anatomical and functional MRI.

1.1.2 Magnetization vector

In the absence of a static magnetic field, i.e. a magnetic field which is invariant in time and space, protons exist in a degenerate state; these particles occupy the same energy stratum, regardless of what their spin angular momentum and magnetic moment may be. When a magnetic field fitting this description is applied to spins, as is the case in an MRI scanner,

Zeeman splitting occurs. Depending on their m_s values, protons will be divided into two distinct populations occupying two separate energy strata. (Huettel *et al*, 2014) The potential energy of protons in each one of these populations depends on not only m_s, but also on the gyromagnetic ratio and the external magnetic field's strength, represented by B_0 in equation 1.3:

$$E = -\gamma\left(\frac{h}{2\pi}\right)m_s B_0 \tag{1.3}$$

Using the Boltzmann distribution, it is also possible to obtain a ratio of the sizes of the two proton populations:

$$\frac{P^{e-}}{P^{e+}} = e^{\Delta E/k_b T} \tag{1.4}$$

Solving equation 1.4 reveals that while both populations are nearly equal in size, the low-energy proton population is slightly larger than its high-energy counterpart. This mismatch between population sizes leads to the sample becoming slightly magnetized at the macroscopic level. (Nishimura, 2010) This net magnetization is usually represented as a vector ($\vec{M}$) whose magnitude can be expressed as the sum of all magnetic moments within a given volume V:

$$\vec{M} = \frac{1}{V}\sum \vec{\mu} \tag{1.5}$$

It is also possible to represent both proton populations as being aligned with or against the magnetic field lines. In this model, the low-energy population corresponds to the protons aligned with the field lines; it is energetically advantageous for these particles to adopt this conformation, thus leading to the aforementioned mismatch between proton population sizes. For this reason, the magnetization vector is also oriented parallel to the external magnetic field. (Huettel *et al*, 2014)

Protons, as well as $\vec{M}$, do not remain static under the influence of a static magnetic field. Due to their angular momentum and their magnetic moment, protons will begin to rotate around the magnetic field lines in a manner reminiscent of a spinning top. This form of rotation is also known as precession. Protons undergo precession at a specific frequency, named "Larmor frequency," which depends on γ as well as on the magnetic field's strength.

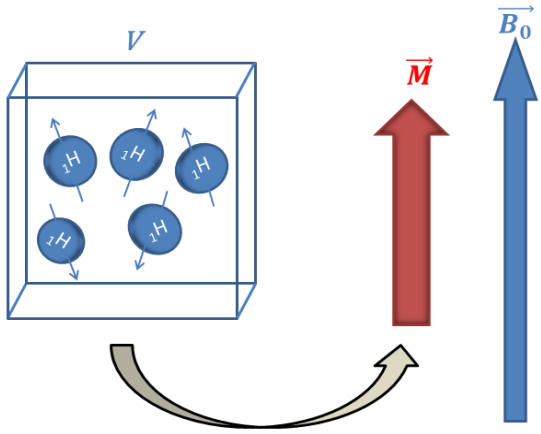

Figure 1: Graphical representation of the magnetization vector $\vec{M}$ arising from a given volume V. The sample becomes magnetized in the presence of an external static magnetic field B0 due to a surplus of protons aligned with the magnetic field lines.

1.1.3 Larmor frequency and nuclear magnetic resonance

The laws of classical mechanics can be used to derive a mathematical expression allowing for the computation of an atomic element's Larmor frequency. Any particle possessing angular momentum and a magnetic moment will experience torque when placed in a magnetic field, as described by equation 1.6:

$$\tau = \vec{\mu} \times \vec{B_0} \tag{1.6}$$

This torque can also be expressed as a variation of the angular momentum over time. The resulting cross product can be written as:

$$\frac{dS}{dt} = \vec{\mu} \times \vec{B_0} \tag{1.7}$$

By multiplying both sides of equation 1.7 by γ, it becomes possible to express the variation of the magnetic moment over time:

$$\frac{d\mu}{dt} = \gamma(\vec{\mu} \times \vec{B_0}) \tag{1.8}$$

Equation 1.8 is also valid at the macroscopic level and can be extended to the magnetization vector:

$$\frac{d\vec{M}}{dt} = \gamma(\overrightarrow{M} \times \overrightarrow{B_0}) \quad \textbf{(1.9)}$$

By solving this differential equation, which governs the rate of change of the magnetization vector over time, the relationship between the Larmor frequency and the magnetic field strength is obtained:

$$\omega_0 = \gamma B_0 \quad \textbf{(1.10)}$$

The Larmor frequency is of great import when attempting to discuss proton excitation. As mentioned at the beginning of this chapter, MRI signal is generated by using an RF pulse to alter the orientation of protons in a targeted volume. This is done to tip the magnetization vector away from the external magnetic field's lines, as $\overrightarrow{M}$ cannot be distinguished from $\vec{B}_0$ under normal circumstances. In order for excitation to occur, however, the central frequency of the RF pulse must be matched to the protons' Larmor frequency. When this condition, also known as the resonance condition, is met, energy is transferred from the RF pulse to the sample, prompting a number of protons on the lower energy stratum to ascend to the higher level. (Berman, 2012) At the macroscopic level, this corresponds to the magnetization vector moving away from $\vec{B}_0$ and into a plane orthogonal to the magnetic field lines.

1.1.4 Principles of excitation

It is also possible to explain the excitation process by making use of classical mechanics notions. From this point of view, the magnetization vector's descent into the transverse plane is due to the application of torque by the RF pulse. This pulse is a circularly-polarized electromagnetic wave whose magnetic field can be expressed as:

$$\vec{B}_1 = B_1\hat{x}\cos(\omega t) - B_1\hat{y}\sin(\omega t) \quad \textbf{(1.11)}$$

As $\vec{B}_1$'s central frequency is the same as the protons' precession frequency in the case of on-resonance excitation, it becomes possible to describe the interaction between the RF pulse and the magnetization vector in a rotating reference frame. The differences between this new model and the observer's reference frame are illustrated in figure 2, but the main advantage of

this new notation scheme is that $\overrightarrow{M}$, while still aligned with $\vec{B}_0$, can be considered static instead of undergoing precession.

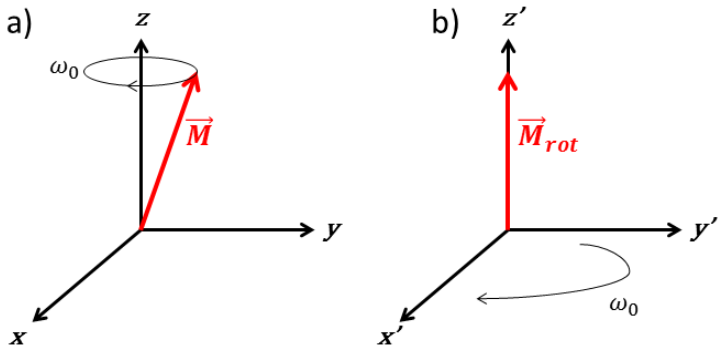

Figure 2: Graphical representation of the behaviour of the magnetization vector in a) the observer's reference frame and b) the rotating reference frame. The main magnetic field is aligned with the z axis in both models.

Equations 1.12a, 1.12b and 1.12c describe the passage from one reference frame to the other:

$$\hat{x}' = \hat{x}\cos(\omega t) - \hat{y}\sin(\omega t) \quad \textbf{(1.12a)}$$

$$\hat{y}' = \hat{x}\cos(\omega t) + \hat{y}\sin(\omega t) \quad \textbf{(1.12b)}$$

$$\hat{z}' = \hat{z} \quad \textbf{(1.12c)}$$

The RF pulse's effect on the net magnetization of the spin system can be described using a differential equation analogous to equation 1.9:

$$\frac{d\vec{M}_{rot}}{dt} = \gamma(\vec{M}_{rot} \times \vec{B}_{eff}) \quad \textbf{(1.13)}$$

In the equation above, the magnetic field term, $\vec{B}_{eff}$, encompasses not only the contribution of the RF pulse's magnetic field, $\vec{B}_1$, but also that of the main magnetic field $\vec{B}_0$. This new variable is dubbed the effective magnetic field and is described by equation 1.14:

$$\vec{B}_{eff} = B_1\hat{x}' + \left(B_0 - \frac{\omega}{\gamma}\right)\hat{z}' \quad \textbf{(1.14)}$$

In the case of on-resonance excitation, the longitudinal component of the effective field, i.e. the field component aligned with the z' axis of the rotating reference frame, is reduced to zero and the RF pulse's effect on $\vec{M}$ is maximized. The magnetization vector will then pivot around the x' axis, as depicted in figure 3, at an angle which depends on the RF pulse's maximum amplitude, the duration of its application, designated by τ in equation 1.15, and the protons' gyromagnetic ratio:

$$\theta = \gamma B_1 \tau \tag{1.15}$$

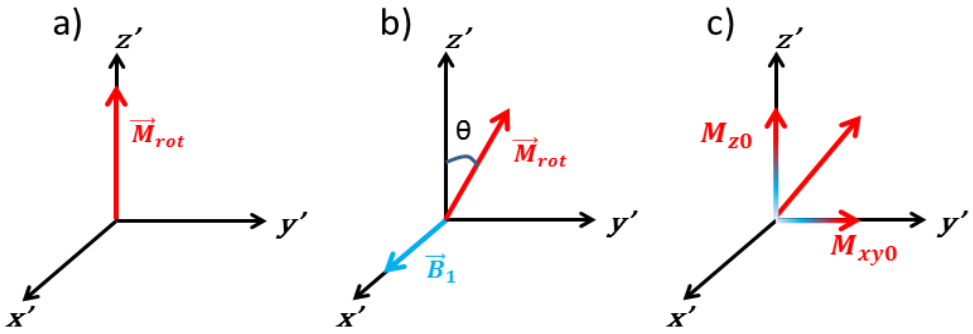

Figure 3: Graphical depiction of the excitation process in the rotating frame when the resonance condition is met. a) At rest, the magnetization vector is aligned with the longitudinal axis of the reference frame. b) The RF pulse, oriented along the $\hat{x}'$axis, tips the magnetization away from the $\hat{z}'$ axis with a given flip angle. c) The excitation process allows for the decomposition of $\vec{M}$ into its longitudinal and transverse components.

The transverse component of the magnetization vector, M_{xy}, can also be broken down into two more components respectively oriented along the x' and y' axes: M_x and M_y. Complex notation is commonly employed to represent the composition of this transverse component of the magnetization vector:

$$M_{xy}(t) = M_x(t) + iM_y(t) \tag{1.16}$$

The angle separating these two components is known as the phase angle and plays an important role in characterizing MRI signal behaviour:

$$\varphi = \tan^{-1}\left(\frac{M_y}{M_x}\right) \tag{1.17}$$

It is important to reiterate at this point that the net magnetization of a spin system cannot be detected unless it is tipped into the magnetic field's transverse plane; only the transverse component of the magnetization vector contributes to signal generation.

1.1.5 Relaxation mechanisms

Once excitation ceases, the system will begin to return to equilibrium through two relaxation mechanisms which govern the longitudinal magnetization's recovery rate and the transverse component's decay. These processes operate according to time constants which vary from one biological tissue to the next, but the molecular interactions at the heart of these phenomena are the same in every case.

The regrowth of the magnetization vector's longitudinal component is due to the dissipation of energy transferred to the protons by the RF pulse into the surrounding molecular lattice. (Berman, 2012) This process, known as longitudinal relaxation or spin-lattice relaxation, is governed by the T1 time constant and can be described by a first-order differential equation:

$$\frac{dM_z}{dt} = \frac{-(M_{z0} - M_0)}{\mathrm{T1}} \tag{1.18}$$

By solving the equation above, it becomes possible to calculate the magnitude of the longitudinal magnetization at a given time *t* following the excitation period:

$$M_z(t) = M_0 + (M_{z0} - M_0)e^{(-t/\mathrm{T1})} \tag{1.19}$$

Transverse magnetization decay, on the other hand, is caused by a loss of phase coherence brought on by naturally-occurring interactions between neighbouring spins. (Nishimura, 2010) These interactions are responsible for transient local variations in the magnetic field strength, which in turn influence the Larmor frequency of the surrounding spins, causing them to accumulate differing amounts of phase. This phenomenon, also called spin-spin relaxation or transverse relaxation, is governed by the T2 constant and can also be described as a first-order differential equation:

$$\frac{dM_{xy}}{dt} = \frac{-M_{xy}}{\mathrm{T2}} \tag{1.20}$$

The solution to this equation, in the case of a static and uniform B_0 is:

$$M_{xy}(t) = M_{xy0} e^{(-t/\mathrm{T2} - i\varphi)} \tag{1.21}$$

Molecular interactions are not the only contributors to transverse relaxation. Magnetic field inhomogeneities accelerate the dephasing process that leads to transverse magnetization decay. The non-uniformity of the main magnetic field can be attributed to improper shimming or even the heterogeneous chemical composition of the object to be scanned. In the latter case, field inhomogeneities are generated when structures presenting different values of magnetic susceptibility are juxtaposed. (Huettel *et al*, 2014) This is particularly evident at air-tissue boundaries within the human body, in locations such as the ear canals or regions proximal to the brain's frontal lobe. (Uludag *et al*, 2005)

Spins located in these regions will precess at rates which depend on the local magnetic field strength, thus impacting their phase accrual and hastening the loss of phase coherence between all spins. The resulting shortened relaxation time is governed by a new time constant, T2*, whose value can be determined by the following equation:

$$\frac{1}{\mathrm{T2}^*} = \frac{1}{\mathrm{T2}} + \frac{1}{\mathrm{T2}'} \tag{1.22}$$

The effects of field inhomogeneity-induced dephasing are contained in the term 1/T2', also referred to as R2'. This form of dephasing is noteworthy due to the fact that it is reversible; using certain imaging techniques, it is possible to reverse the loss of phase coherence prompted by susceptibility-induced field gradients, leading to a recovery of MRI signal in the affected regions. These techniques and their relevance in functional imaging will be detailed in the following sections of this chapter. The effects of pure T2 relaxation, on the other hand, are irreversible due to the random nature of the molecular interactions which generate microscopic fluctuations of the static magnetic field's strength. (Buxton, 2013)

1.1.6 Bloch equation

By combining equations 1.9, 1.18 and 1.20, it becomes possible to mathematically characterize the magnetization vector's behaviour in the presence of a magnetic field:

$$\frac{d\vec{M}}{dt} = \vec{M} \times \gamma \vec{B}_0 - \frac{(M_x \hat{x} + M_y \hat{y})}{\mathrm{T2}} - \frac{(M_z - M_0)\hat{z}}{\mathrm{T1}} \tag{1.23}$$

This equation is called the Bloch equation and can be solved in many different ways depending on the nature of the existing magnetic fields. In the previous sub-section, one such solution has been offered to describe the behaviour of transverse magnetization arising from a perfectly homogeneous object placed within a perfectly uniform static magnetic field. In practice, these conditions are not achievable and a spatially-varying field must be considered when solving the Bloch equation. (Nishimura, 2010) In addition to this, time-varying magnetic field gradients, generated by the scanner's gradient coils, are employed during the scan process for slice selection and spatial encoding of MRI signals. Their presence must also be accounted for when attempting to model the magnetization vector's behaviour.

A generic solution to the Bloch equation, i.e. when a time-varying non-uniform magnetic field is considered, can be represented as:

$$M(r,t) = M(r) e^{(-t/T2(r))} e^{-i\varphi} e^{-i\gamma \int_0^t \vec{G}(\tau)\cdot\vec{r} d\tau} \tag{1.24}$$

Only T2 relaxation is considered in the signal decay term and $\vec{G}(\tau) \cdot \vec{r}$ represents a linear, time-varying magnetic field gradient with an arbitrary orientation. (Nishimura, 2010) Here, $\vec{r}$ represents a vector with components of arbitrary length oriented in the x, y and z directions. If only the behaviour of the magnetization vector's transverse component is considered during signal acquisition, the total amount of signal produced by excited spins within a given volume can be expressed as:

$$S(t) = \iiint M(x,y,z)\, e^{(-t/T2(r))} e^{-i\varphi} e^{-i\gamma \int_0^t \vec{G}(\tau)\cdot\vec{r} d\tau} dx\, dy\, dz \tag{1.25}$$

1.2 Imaging principles

This section will be dedicated to describing the different processes by which an image is created using MRI, from signal detection methods to the aforementioned spatial encoding techniques. Signal echo production techniques and the contrast-generating mechanisms that make use of these echoes will also be discussed.

1.2.1 Signal detection

To understand how signal is detected in MRI, it is necessary to consider the magnetization vector's behaviour in the observer's reference frame following excitation. Once tipped into the transverse plane by an RF pulse, the net magnetization of a spin system will begin to die off in the transverse plane while continuing to precess around the reference frame's longitudinal axis. In this situation, the transverse magnetization's behaviour can be likened to that of a rotating bar magnet. (Huettel *et al*, 2014) A receiver coil can then be used to measure the temporal variation of magnetic flux caused by the rotation of the spin system's magnetization. As per Faraday's law of induction, such a variation will induce an electromotive force in a loop of wire made of a conductive metal:

$$\varepsilon = \frac{-d\varphi}{dt} \tag{1.26}$$

In order to detect the spin system's magnetization, however, the receiver coil must be tuned to the same frequency characterizing the precession of the targeted spin species. (Sabouri, 2014)

1.2.2 Selective excitation

When a substance of homogenous composition (e.g. a bottle of distilled water) is exposed to a perfectly uniform static magnetic field, all of the spins in the sample will precess at the same Larmor frequency. Consequently, the totality of these particles will be excited by an RF pulse whose central frequency satisfies the resonance condition. In conventional scan sessions, it is

preferable to restrict one's analysis to a specific region of the sample. In fMRI experiments targeting the brain, for example, the RF pulse must only excite protons in a subject's cranial region. The key to performing selective excitation in MRI lies in equation 1.10, which describes the directly proportional relationship between magnetic field strength and the Larmor frequency. If it becomes possible to introduce a controlled variation of $\vec{B}_0$'s magnitude in space, a relationship between a spin's position and its Larmor frequency can be established. To perform this operation, every MRI scanner is equipped with three pairs of gradient coils which are capable of generating linearly-varying magnetic fields in all directions of three-dimensional space. (Prince *et al*, 2006) These linear field gradients are then superposed onto $\vec{B}_0$ and the resulting magnitude at a given point is given by:

$$B(r) = B_0 + (\vec{G} \cdot \vec{r}) \tag{1.27}$$

In practice, a single one of these gradients can be used to obtain images of the object in the axial, coronal or sagittal planes depending on which gradient is used. As the human body is usually aligned with the magnetic field lines, i.e. the z-axis, when placed in the scanner, equation 1.27 can be rewritten to obtain:

$$B(z) = B_0 + G_z z \tag{1.28}$$

The RF pulse's central frequency can then be adjusted to excite a specific region of the object. Each excited region, known as a slice or slab, will also have a thickness which depends on the gradient's strength as well as on the pulse's bandwidth, the latter representing the range of Larmor frequencies targeted during excitation. The relationship between these variables is expressed in equation 1.29 and illustrated on figure 4:

$$\Delta z = \frac{\Delta\omega}{\gamma G_z} \tag{1.29}$$

Selective excitation also allows for a simplification of equation 1.25 by reducing the signal equation to a two-dimensional problem. This is first accomplished by integrating the net magnetization along the direction orthogonal to the image plane (e.g. the z-axis for an axial image):

$$M(x,y) = \int_{z_0-\frac{\Delta z}{2}}^{z_0+\frac{\Delta z}{2}} M_{xy0}(x,y,z)dz \quad \textbf{(1.30)}$$

The integral boundaries are set to correspond to those of the volume or slice of interest. (Nishimura, 2010) Inserting the left-hand term of equation 1.30 into equation 1.25 results in

$$S(t) = \int_0^x \int_0^y M(x,y)e^{-i\gamma \int_0^t (G_x(\tau)x + G_y(\tau)y)d\tau} dxdy \quad \textbf{(1.31)}$$

This reduction in complexity will serve to highlight a fundamental mathematical relationship which links signal acquisition to image creation later on in this chapter.

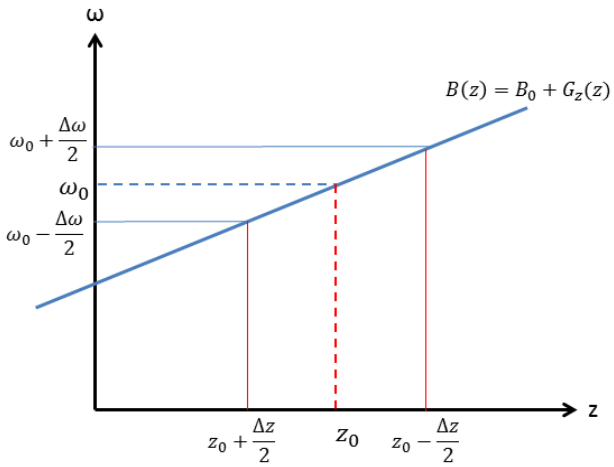

Figure 4: Graphical representation of the relationship between RF pulse bandwidth, gradient strength and slice thickness during selective excitation.

1.2.3 RF pulses and slice profiles

The RF pulse's central frequency and bandwidth play an important role in determining the location where excitation occurs in the sample and the resulting slice's thickness, but they are not the only factors at play during selective excitation. The pulse's envelope function, $B_1(t)$, helps determine the shape of the slice profile. The ideal slice profile should be that of a boxcar function; a rectangular profile ensures that all spins whose Larmor frequencies are within the specified frequency band will be excited uniformly while those whose precession rates are outside this range of values will remain unaffected by the pulse.

Due to excitation being discussed in terms of frequency ranges, it is important to keep in mind that these slice profiles are defined in the frequency domain; the RF pulse's envelope function, $B_1(t)$, must be calculated in the time domain. To retrieve the requisite envelope shape, the inverse Fourier transform of the function that describes the slice profile can be calculated. However, the assumption that envelope functions and slice profiles are related to each other by the Fourier transform is valid only when RF pulses are played out using small flip angles ($\theta < 90°$). This approximation breaks down for larger flip angles due to the non-linearity of the Bloch equations. The Fourier transform, being a linear operator, is ill-suited for the computation of the slice profiles associated with these pulses. (Bernstein *et al*, 2004):

For pulses respecting the small flip angle approximation, a rectangular slice profile can be obtained by making $B_1(t)$ a sinc function:

$$B_1(t) = A * sinc\left(\frac{\pi t}{t_0}\right) = A * t_0 * \frac{sin(\pi t/t_0)}{\pi t} \quad \textbf{(1.32)}$$

In the equation above, t_0 is equal to the time separating the central lobe's peak to the first point of zero-crossing and is inversely proportional to the pulse's bandwidth. As the duration of the sinc pulse's central lobe diminishes, the range of frequencies affected by the rectangular slice profile grows. In practice, it is not possible to achieve a perfectly rectangular slice profile, as this would require the use of a sinc function of infinite duration. Truncated waveforms must therefore be used when designing RF pulses, a limitation that will affect the slope of the transition band in the pulse's frequency response. The transition between the area targeted by the pulse and its surroundings, regions respectively referred to as the passband and the rejection band, is therefore done gradually, leading to undesirable perturbation of the spin system's magnetization outside the targeted slice. (Bernstein *et al*, 2004)

More sophisticated algorithms for the production of RF pulses for specific applications in MRI are also available, such as the Shinnar-LeRoux (SLR) algorithm. Using the SLR algorithm, RF pulse creation can be thought of as a filter design process whereby B_1 is determined using the knowledge of the shape of the pulse's frequency response. (Pauly *et al*, 1991) Two complex polynomials, $A(z)$ and $B(z)$, are required for this process. The first polynomial, $B(z)$, is computed using finite-impulse response (FIR) filter design methods to create a frequency response whose shape best approximates that of an idealized version that is set to $\sin(\theta/2)$, with θ being equal to

the flip angle with which the pulse is to be played out. (Pauly, 2006) Due to the finite length of the RF pulse, the filter's shape will contain ripples in the passband and in the rejection band in addition to presenting a sloped transition band. The second polynomial, *A(z)*, is computed using *B(z)* and must satisfy a normalization constraint. It has been found that the optimal solution to this problem is to select *A(z)* with a minimum phase, as this corresponds to the RF pulse which deposits the least amount of energy into the sample during its application. (Pauly *et al*, 1991; Bernstein *et al*, 2004) Once *A(z)* and *B(z)* have been determined, an inverse SLR transform is used to obtain the shape of the desired RF pulse in the time domain.

1.2.4 Frequency encoding

To create images using MRI, it is not enough to simply acquire the signal produced by selective excitation. It is necessary to spatially encode MRI signals in order to determine the spatial distribution of the magnetization at every point with coordinates *(x, y)* in the slice. The number of points to examine corresponds to the number of volume elements, or voxels, that make up the resulting image. Two mechanisms involving the use of magnetic field gradients are used for this purpose: frequency encoding and phase encoding. (Huettel *et al*, 2014)

As indicated by its name, frequency encoding seeks to resolve the spatial distribution of proton density along one axis of the imaging plane through the application of a magnetic field gradient during the signal detection period. As evidenced by equations 1.10 and 1.28, the introduction of a controlled variation of the magnetic field's strength along one direction of space makes it possible to determine a spin's position along this same axis based on its Larmor frequency. This spatial encoding process therefore makes it possible to associate a signal's amplitude to the voxel from which it originated due to the magnetization vector formed by the spins in each voxel along the frequency axis being characterized by a unique value of the Larmor frequency, as expressed by the relationship of linear proportionality between this quantity and the magnetic field strength. An analog-to-digital converter (ADC) is also used at this time to discretely sample the signal as it is being acquired. Due to the frequency-encoding gradient being deployed at the same time as the ADC, the former is also known as a readout gradient. (Huettel *et al*, 2014)

1.2.5 Phase encoding

Frequency encoding alone is not sufficient to properly determine the spatial distribution of spins in the slice. Another mechanism must be used in the second direction of the image plane to complete the spatial encoding process. Phase encoding seeks to establish a position-dependent relationship between a spin's location and the amount of phase accumulated by said spin after the temporary application of a magnetic field gradient (G_y) along one axis of the image plane. As is the case with frequency encoding, the presence of a magnetic field gradient results in a modification of the spins' Larmor frequencies and spins subjected to a stronger magnetic field will undergo faster precession than those exposed to a weaker field. Once the gradient is removed, the spins will return to their original Larmor frequency, but they will have accumulated different amounts of phase depending on their location along the phase-encoding axis; spins subjected to a strong magnetic field will have accumulated more phase than spins located in a weaker field due to their rapid precession. (Prince *et al*, 2006; Nishimura, 2010; Huettel *et al*, 2014)

1.2.6 K-space

In MRI, images are created by acquiring a given amount of signals characterized by different frequency and phase values due to the unique combination of G_x and G_y applied over each acquisition cycle necessary for spatial encoding. Therefore, a special notation scheme called k-space has been developed to relate these signals to the actual image. Owing its name to the variable used to denote the wavenumber, the concept of k-space is often illustrated as a two-dimensional matrix in which the signals are stored over the course of the acquisition period. This habitual representation of k-space is presented at figure 5. (Huettel *et al*, 2014) While the edges of this matrix contain high-frequency signals, i.e. information pertaining to edges and boundaries in the image, low-frequency signals which contain information on image contrast are found in its center. The size of this matrix is equal to the number of voxels in the image and is chosen by the scanner operator at the outset of the scan session. Each one of k-space's points can be described by a pair of coordinates, k_x and k_y, whose values are proportional to the time integrals of gradient field strength:

$$k_x(t) = \frac{\gamma}{2\pi}\int_0^t G_x(\tau)d\tau \quad \textbf{(1.33a)}$$

$$k_y(t) = \frac{\gamma}{2\pi}\int_0^t G_y(\tau)d\tau \quad \textbf{(1.33b)}$$

Using these definitions, it becomes possible to describe the signal acquisition process as filling k-space; applying magnetic field gradients for the purpose of spatially encoding signals generated by excitation is tantamount to varying k_x and k_y over the course of the scan. (Huettel *et al*, 2014) The number of phase-encoding steps required for image reconstruction corresponds to the total number of k_y coordinates in the matrix while each k_x coordinate represents a moment in time when the signal is digitized by the analog-to-digital converter during frequency encoding.

Another advantage of equations 1.33a and 1.33b is that they can be inserted into the signal equation to reveal a fundamental relationship between k-space and the resulting image. Rewriting equation 1.31 in this manner yields the following equation:

$$S(t) = \int_0^x \int_0^y M(x,y)e^{-i2\pi(k_x(t)x+k_y(t)y)}dxdy \quad \textbf{(1.34)}$$

The equation above indicates that the image can be obtained simply by calculating the inverse two-dimensional Fourier transform of k-space. (Nishimura, 2010)

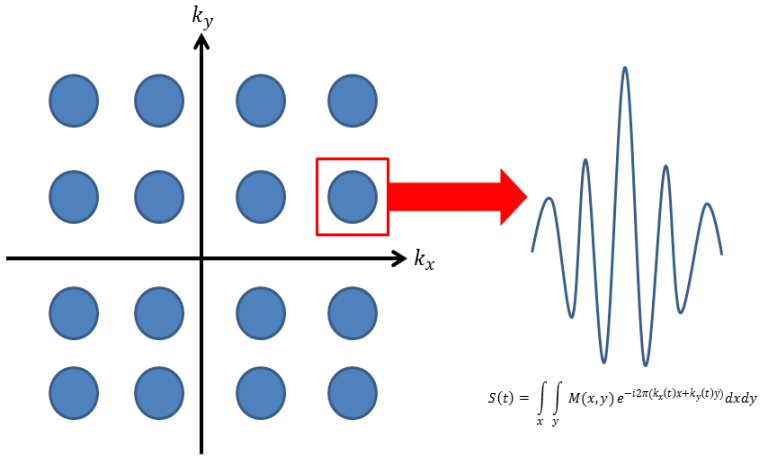

Figure 5: Graphical representation of k-space as a matrix containing M by N points, depending on the number of frequency and phase-encoding steps used to acquire an image. Each point of frequency space represents the entire signal waveform acquired at that moment using a specific combination of frequency encoding and phase encoding. Image adapted from (Huettel* et al, *2014.)

An important caveat must be added to the model of k-space described in the preceding paragraphs. While both the number of points in k-space and the number of voxels that make up the image may be equal, it is important to note that there is no 1:1 relationship between the voxel with coordinates *(x, y)* in the image and the point described by (k_x, k_y) in frequency space. Each point in k-space actually represents a snapshot of the entire signal which has been encoded with a specific combination of G_x and G_y, as depicted in figure 5. (Huettel *et al,* 2014)

1.2.7 Gradient echoes

Due to rapid signal decay owing to T2* relaxation, it is often impractical to acquire the MRI signal immediately after excitation for the purpose of image creation. To circumvent this problem, many techniques have been developed to generate signal echoes at a time of the scanner operator's choosing following excitation. The time separating the halfway point of the excitation event from the echo's peak is called the echo time (TE) and can also be defined as the time at which zero-crossing in k-space occurs.

One popular echo generation technique, illustrated at figure 6, involves the use of a magnetic field gradient along the frequency-encoding axis to successively induce spin dephasing and rephasing. To generate these gradient echoes, G_x is first played out for a period of time τ in order to hasten the loss of spin phase coherence. The gradient polarity is then reversed and its presence is maintained for a time equal to 2τ for the purpose of frequency encoding. The spins will then come back into phase at time τ after the gradient polarity is reversed, causing an echo of the original signal to be produced, albeit with a diminished amplitude due to T2* relaxation. This is due to the fact that the mechanisms allowing for the creation of gradient echoes cannot reverse the dephasing incurred by the presence of magnetic susceptibility-induced field gradients, leading signal decay to be governed by T2* instead of T2. (Brown *et al*, 2014)

Viewed differently, a gradient echo is formed when the area under the dephasing and readout gradient lobes illustrated on figure 6 become equal. (Nishimura, 2010) In k-space, this sequence of events can be depicted first as a shift in the $-k_x$ direction due to the application of the dephasing lobe, followed by a traversal of k-space in the $+k_x$ direction, with the echo occurring at

the moment of zero-crossing. The dephasing gradient is also known as a "prewinder" as it prepares the sequence for the acquisition of a full line of k-space.

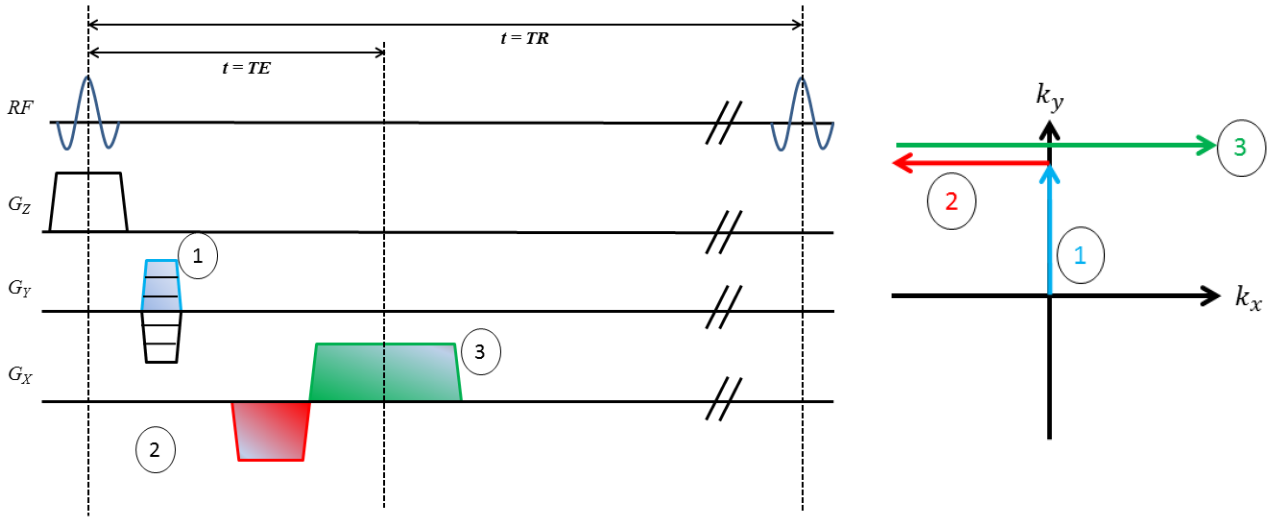

Figure 6: Left – Pulse sequence diagram illustrating the principle of gradient-echo generation. Right – Corresponding trajectory drawn in k-space by the spatial encoding gradients. The process is repeated until each line of k-space is filled and a gradient echo is generated when the green line crosses the k_y axis.

1.2.8 Spin echoes

Other echo generation techniques can be employed to eliminate the effects of susceptibility-induced spin dephasing, such as the use of RF pulses played out at TE/2 to reverse phase dispersion and generate what is known as a spin echo. These RF pulses are called refocusing pulses due to their effect on the spin system and are characterized by a flip angle of 180°. To understand this pulse's mode of operation, one may consider the behaviour of a group of spins located in a zone where the magnetic field strength is inhomogeneous and each spin will experience a position-dependent value of the magnetic field strength. Following excitation, each proton will accumulate an amount of phase φ_1 which depends on the local field strength over the course of the TE's first half. The refocusing pulse will then "flip" the magnetization over and the phase accumulated by spins over the TE's second half, φ_2, will be equal to $-\varphi_1$, nullifying the phase shift incurred during the first half of TE. At TE, all spins will come back into phase and a spin echo will be produced. The refocusing pulse therefore serves to reverse the phase accumulation that leads to T2*-governed signal decay, resulting in the production of an echo

whose amplitude is determined by T2 relaxation. (Uludag *et al*, 2005) A diagram representing the steps necessary for spin echo generation is presented at figure 7.

Contrary to gradient echo generating mechanisms, the prewinder gradient, appearing in red in figure 7, has the same polarity as the frequency encoding gradient. This is due to the fact that the refocusing pulse also inverts the k-space coordinate values, multiplying both k_x and k_y by -1. This spin-echo production mechanism, as well as its gradient-echo counterpart presented in figure 6, is an example of a simple MRI pulse sequence, a computer-controlled sequence of events played out with a specific timing on the scanner to generate images with a desired contrast. The elements that make up a pulse sequence are not restricted to those necessary for excitation and signal encoding, but may also include other mechanisms necessary for the modulation of a spin system's magnetization in order to produce an anatomical or functional contrast of interest. This terminology shall henceforth be used in the remainder of this dissertation to refer to the manifold imaging techniques destined for use in anatomical and functional MRI. (Prince *et al*, 2006)

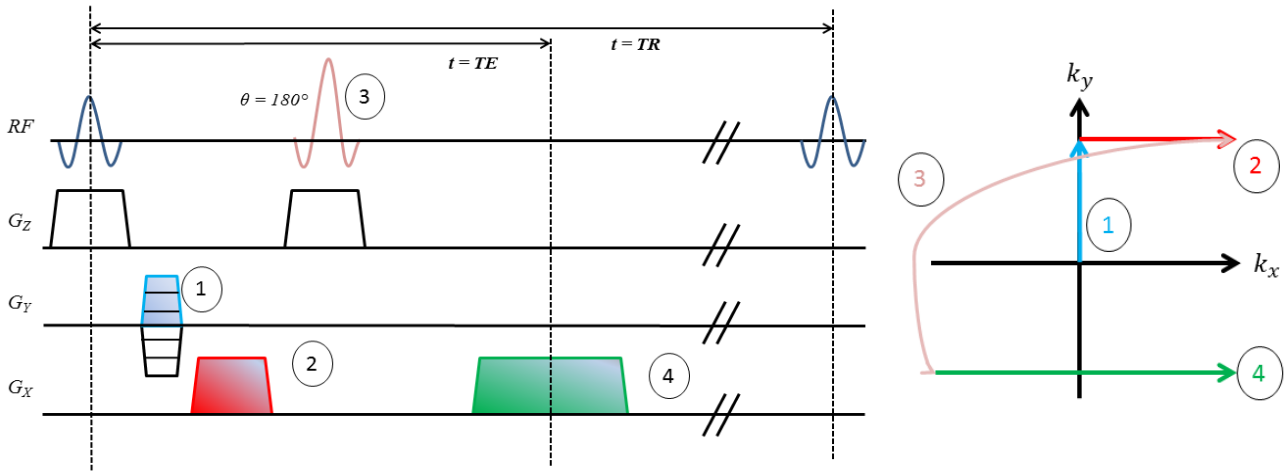

Figure 7: Left – Pulse sequence diagram illustrating the principle behind spin echo generation. Right – Corresponding trajectory drawn in k-space. It is important to note that the application of a 180° refocusing pulse will cause a phase reversal in frequency space, multiplying the (k_x, k_y) coordinates by -1 at that time. The process is repeated until each line of k-space is filled.

1.2.9 Contrast generation

One of MRI's main strengths is its ability to produce images with different contrasts simply by varying two parameters that control the timing of signal acquisition in a pulse sequence. The first parameter is the previously-discussed TE and the second is the repetition time (TR), defined as the time interval separating two successive acquisition cycles. Three of the best-known and most-utilized contrasts are proton density (PD), T2-weighting and T1-weighting.

As indicated by its name, PD contrast reflects the concentration of protons within a given sample. To obtain images with this type of contrast, a short TE is used to mitigate the effects of T2/T2* relaxation along with a long TR to allow the magnetization to fully relax before the next excitation pulse is applied. The two other contrasts are used to differentiate biological tissues or other substances based on their longitudinal or transverse relaxation time constants. To obtain a T2-weighted image, a pulse sequence harbouring a spin-echo production mechanism must be used to eliminate T2* relaxation effects. A long TR is then employed for the same reasons outlined earlier for PD imaging, as well as a TE set to the T2 values of the tissues to be examined. T1-weighting, on the other hand, is generated by using short TE and TR values so as to repeatedly excite the tissues before the longitudinal magnetization can return to its steady-state value. (Prince *et al*, 2006)

Other types of contrast can be obtained in MRI by directly acting upon the phase of water spins over the course of the acquisition period. Diffusion weighting, used to render a pulse sequence sensitive to molecular motion, is one example. To generate this contrast, two gradient waveforms with matched moments are applied between the excitation and readout periods in order to apply position-dependent phase shifts to mobile spins that will precipitate the loss of phase coherence and result in signal attenuation. The degree to which the signal is attenuated depends on both the mobility of the spins and the physical parameters of the diffusion gradient lobes (e.g. rise times, amplitude, etc.), which are played out with the same polarity on both sides of the refocusing pulse in spin-echo imaging and with opposing polarities in gradient-echo imaging. (Bernstein *et al*, 2004)

1.3 Functional magnetic resonance imaging

Now that the sequence of events leading to image creation in MRI have been presented, it becomes possible to explain how this imaging process can be used to detect neuronal activation in the brain. The final section of this chapter will be devoted to myriad topics pertaining to fMRI, from basic principles of neurophysiology to the different pulse sequences used to acquire images with physiological contrasts that denote brain activation.

1.3.1 Basics of neurophysiology

To understand how neuronal activity can be detected in MRI, it is necessary to examine how brain function impacts other physiological systems such that MRI signal generation and tissue relaxation times will be affected. The phenomena responsible for the alteration of signal decay times originate at the cellular level with neurons, the functional units of the human body's nervous system, playing an important role in these processes.

Neurons are cells specialized in the reception, transmission and generation of bioelectrical and chemical signals as a means to convey and process information. Many types of neurons exist and while they may differ from one another by their shapes, their location in the nervous system and their roles in signal processing, every neuron possess a set of common structures that allows them to participate in signaling tasks. Among these are dendrites and axons, cytoplasmic projections that emerge from the cell body to respectively engage in signal reception and transmission. While dendrites are usually found in large quantities on neurons, each such cell possesses but a single axon whose length far surpasses that of the dendrites'. (Marieb, 2005) An example of a neuron along with its structural components is presented on figure 8.

Neurons communicate with each other by generating electrical signals called action potentials which travel along the axon and trigger the release of chemical messengers called neurotransmitters into synapses, cellular junctions in which a neuron's axon terminals are in close proximity to a target nerve cell's dendrites. Myelin, a proteolipidic substance which gives the nervous system's white matter its distinct coloration, is often apposed on the axons by glial

cells in the nervous system to increase the conduction speed of action potentials. The binding of neurotransmitters to receptors on the post-synaptic neuron's membrane will modulate the cell's electrical activity by altering its resting potential. The resulting post-synaptic potentials can either be excitatory in nature and depolarize the neuron's membrane, increasing the likelihood of action potential production, or inhibit the generation of such signals through hyperpolarization. (Huettel *et al*, 2014) Because neurons form numerous synapses with other nerve cells, they must integrate the entirety of the incoming signals to determine their net result on the cell's firing activity. In other words, all excitatory and inhibitory post-synaptic potentials will be summed up by the target neuron and their combined effect will determine whether or not an action potential is produced. (Marieb, 2005; Huettel *et al*, 2014)

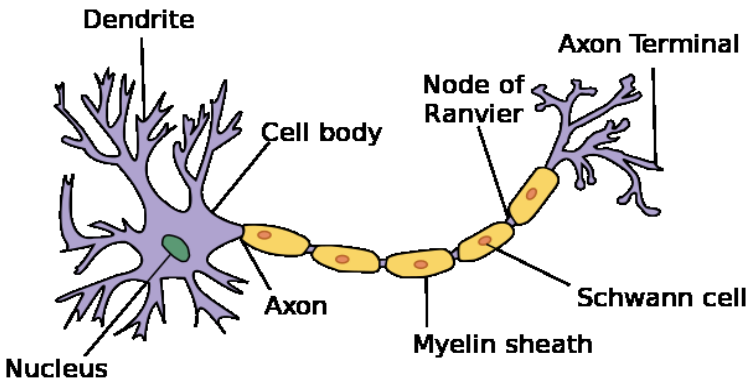

Figure 8: Picture of a neuron and its structural components. Image sourced from [1].

Action potentials are generated when the neuron's electric potential at the axon hillock is elevated from its resting value, valued between -40 and -70 mV due to the intracellular compartment's negative charge, over a given threshold. When the aforementioned threshold is crossed, voltage-dependent ion channels will open, leading to an influx of Na^+ into the neuron until the transmembrane voltage reaches +30 mV. At this point, the sodium ion channels will close and K^+ ions will begin to move down their concentration gradient and exit the cell via their respective ion channels. While this step restores the electrical potential to its resting value, the intra- and extracellular concentrations of Na^+ and K^+ must also be restored to their resting values. For this purpose, specialized proteins called sodium-potassium pumps are used to actively transport these ions against their concentration gradients. (Marieb, 2005) For this process to occur, however, energy must be furnished to the pumps in the form of adenosine triphosphate

(ATP). These molecules are created through a catalytic process called glycolysis, which converts glucose into ATP at a normal rate of two ATP molecules per molecule of glucose. This reaction's output can be amplified through the addition of oxygen. When oxygen is available, pyruvate, a by-product of glycolysis, is ushered into the mitochondria, where it will be processed in a chain of biochemical reactions in order to produce 36 molecules of ATP. The oxygen required for this catalytic process is extracted from the bloodstream, in which it travels while bound to hemoglobin molecules sequestered in red blood cells. (Habas, 2002; Marieb, 2005)

1.3.2 Vasculature of the brain and neurovascular coupling

In the brain, the main sites of neuronal activity reside in the cerebral cortex, a folded layer of gray matter made up of neuronal cell bodies, dendrites, axon terminals and demyelinated axons that covers the surface of the cerebrum. Possessing a thickness of 2 to 3 millimeters, (Shipp, 2007) the cerebral cortex is divided into multiple areas that control many of the individual's vital faculties, such as cognition, voluntary motor control and sensory perception. This structure is also heavily vascularized to allow for the delivery of oxygen and other nutrients such as glucose to neurons implicated in these tasks. Due to the brain's inability to store glucose, continuous perfusion of the cortex is necessary to restore electrochemical equilibrium following the generation of action potentials. (Huettel *et al*, 2014) Perfusion is defined as the volume of blood traversing a mass of tissue during a given time and is commonly expressed in units of mL/100g/min.

To reach the cerebral cortex, oxygenated blood must first travel through two pairs of feeding arteries after exiting the heart and aorta: the internal carotids, which climb up the neck and pass through the skull's temporal bones to reach the brain, and the vertebral arteries, which run parallel to the spine before entering the skull through the foramen magnum. At the lower extremity of the pons, the vertebral arteries will fuse together before splitting into two posterior cerebral arteries at the base of the mesencephalon. These vessels will then form an anastomosis called the circle of Willis with the middle and anterior cerebral arteries, which emanate from the internal carotids. The circle of Willis, which surrounds the pituitary gland and optic chiasma, is

involved in regulating arterial blood pressure in the brain and is presented on figure 9. (Marieb, 2005)

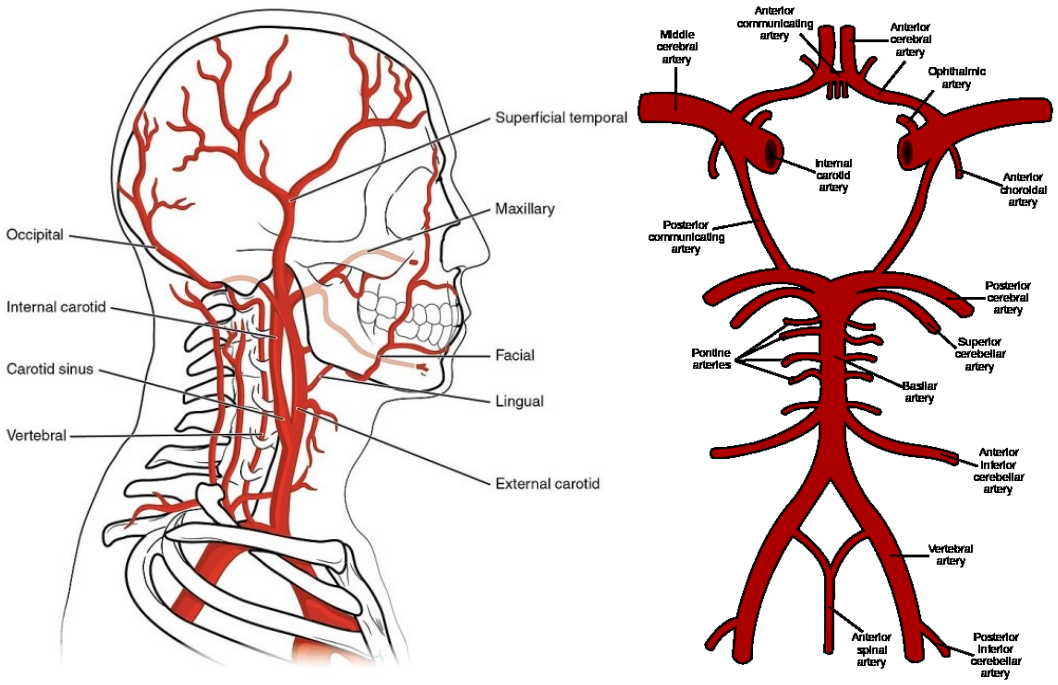

Figure 9: Vascular anatomy of the arterial circulation in the neck, face and upper thorax in humans. Left – Image of the internal and carotid arteries in the neck. Right- Illustration of the Circle of Willis, basilar arteries, posterior cerebral arteries, middle cerebral arteries and anterior cerebral arteries. Images sourced from [2] and [3].

These three pairs of cerebral arteries emit pial branches that run across the cortical surface before penetrating the cortex at multiple locations. The diameter of these intracortical branches diminishes over the course of their descent, transforming into arterioles and, ultimately, capillaries. The latter vessels form intricate networks called capillary beds where the exchange of gases, nutrients and cellular waste between the bloodstream and parenchymal tissue takes place. As oxygen is released into the extracellular space, the newly-deoxygenated blood flows out of the capillaries and into the venous side of the brain's circulatory system. Passing through veinules and cerebral veins, the blood will be drained into large channels called sinuses. Three such channels, the superior and inferior sagittal sinuses and the straight sinus, converge at the back of the brain and a final pair of channels, the transverse sinuses, directs the blood out of the skull and into the jugular veins in the neck. (Marieb, 2005)

It is important to keep in mind that the relationship between the nervous and circulatory systems is not one-sided; neurons do not passively receive the nutrients that are ferried to them by the circulatory system. The nervous system is capable of acting upon vascular tone to regulate blood flow in the cerebral cortex during periods of heightened neuronal activity. (Habas, 2002; Atwell *et al*, 2010) The resulting alterations in blood vessel geometry will trigger regional increases in cerebral blood flow (CBF) and cerebral blood volume (CBV). This anatomo-functional correlation between the nervous and circulatory systems is known as neurovascular coupling and makes functional hyperemia, i.e. a stimulation-mediated elevation in CBF, possible. Specifically, the nervous system's regulation of blood flow in the cerebral cortex ensures the delivery of oxygenated blood to regions of increased neuronal activity in the cerebral cortex during information processing. (Habas, 2002)

1.3.3 Physiological origin of BOLD contrast

In fMRI, periods of neuronal activation are imaged by detecting concomitant hemodynamic changes in the cerebral cortex. Specifically, the arrival of highly-oxygenated arterial blood at the sites of neuronal activity will modulate the lifetime of MRI signal in these regions. To understand how relaxation times are impacted by functional hyperemia, it becomes necessary to examine the magnetic properties of hemoglobin. As mentioned in sub-section 1.3.1, hemoglobin is a protein specialized in the transport of oxygen throughout the circulatory system. This faculty is conferred onto it by ferrous ion-containing heme groups (Marieb, 2005; Berman, 2012), which are also responsible for the coloration of the red blood cells. A single hemoglobin molecule contains four such groups, with each one being able to form a reversible bond with one O_2 molecule. The formation of these bonds will affect the protein's electronic structure, altering its overall magnetic susceptibility. (Pauling *et al*, 1936)

In its deoxygenated form, hemoglobin is paramagnetic; it will be attracted to an external magnetic field such as B_0. When bound to oxygen, hemoglobin becomes diamagnetic and will be weakly repelled by B_0. Oxyhemoglobin is also isomagnetic relative to many types of soft tissue in the body, including the cerebral cortex. It can therefore be deduced that the extraction of oxygen from the bloodstream, which is necessary for ATP synthesis and, consequently, normal

function of the sodium-potassium pumps, will cause a shift of the blood's magnetic susceptibility as it passes through the capillaries. (Habas, 2002) This in turn will generate microscopic magnetic field distortions both inside the vessel and in the surrounding tissue. (Uludag *et al*, 2005; Buxton, 2013) As outlined in sub-section 1.1.5, spins subjected to position-dependent frequency shifts caused by susceptibility-induced field gradients will progressively fall out of phase with each other, which leads to shortened relaxation times and hastened signal decay.

It would be impossible to discern periods of neuronal activation from the resting state if all of the oxygen supplied to the neurons during a period of increased neuronal activity were to be consumed. In this scenario, the susceptibility-induced field distortions caused by the presence of paramagnetic deoxyhemoglobin in the microvasculature would persist and no functional contrast would be formed. In reality, functional hyperemia delivers a quantity of oxygen that far exceeds the amount needed by neurons for aerobic glycolysis. Experiments investigating brain function using positron emission tomography have shown that while changes in CBF and the cerebral metabolic rate of glucose (CMR_{glu}) are coupled, a mismatch exists between CBF and the cerebral metabolic rate of oxygen ($CMRO_2$). (Fox *et al*, 1986) This results in a displacement of venous blood in the microvasculature by oxygen-rich arterial blood. Assuming that oxygen saturation of arterial blood is equal to 1, the relationship between changes in CBF, $CMRO_2$ and venous oxygenation (Y) can be described by the following equation (Kim *et al,* 2006):

$$\frac{\Delta Y}{(1-Y)} = 1 - \frac{(\Delta CMRO_2/CMRO_2+1)}{(\Delta CBF/CBF+1)} \tag{1.35}$$

It is important to remember that CBV increases alongside CBF due to the distention of the blood vessels caused by the influx of arterial blood. (Kim *et al*, 2012) The relationship between changes in these quantities is given by Grubb's power law:

$$\frac{\Delta CBV}{CBV} = \left(\frac{\Delta CBF}{CBF}\right)^{\alpha} - 1 \tag{1.36}$$

The exponent α is a flow-volume conversion term. For changes of CBF and CBV measured in arterioles, veinules and capillaries, α is valued at 0.38. (Grubb, 1974) However, as MRI signals are impacted by shifting concentrations of deoxyhemoglobin, experiments measuring changes in venous CBV instead of total CBV during periods of neuronal activity have

found α to be closer to 0.23. (Chen *et al*, 2009) The changes brought on by functional hyperemia are graphically represented in figure 10.

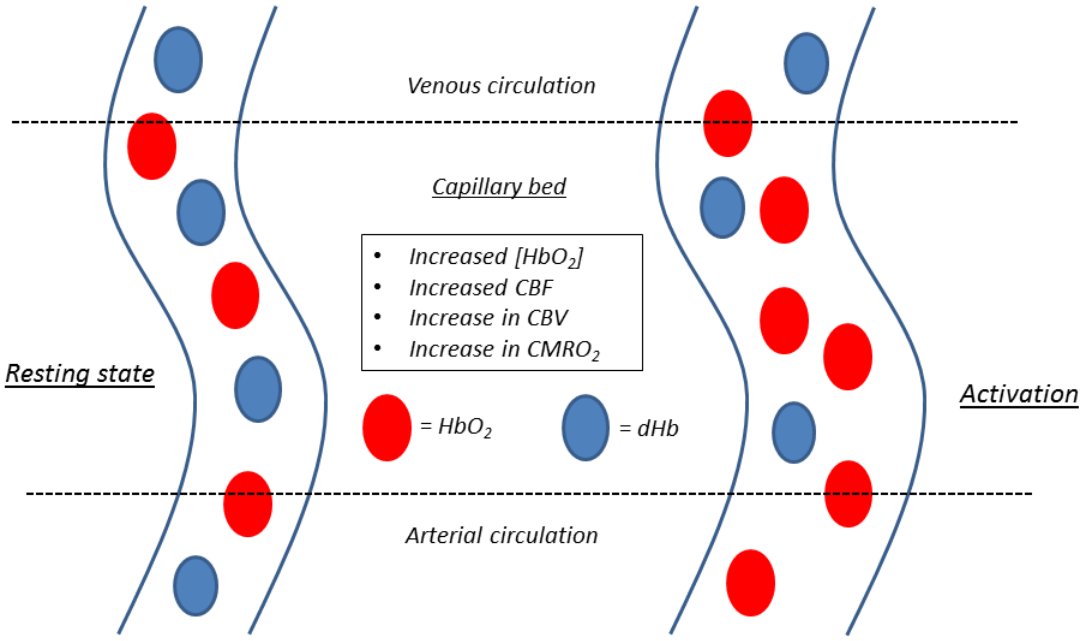

Figure 10: Graphical representation of the physiological changes brought on by functional hyperemia in the brain's vascular network. Figure adapted from (Jezzard* et al, *2005)

This reduction of the concentration of intravascular deoxyhemoglobin eliminates the susceptibility-induced magnetic field distortions and lengthens the transverse relaxation time in the voxels within the region of interest, prompting a temporary increase in MRI signal intensity in these areas. While an elevation of venous CBV will contribute to a shortening of said relaxation times due to a rise of the concentration of deoxyhemoglobin, the increase in venous oxygenation brought on by functional hyperemia is dominant factor behind the increase of the region MRI signal's longevity. (Uludag *et al*, 2005; Kim *et al*, 2012) It can therefore be understood that hemoglobin acts as a contrast agent whose effect on MRI signal intensity will depend on its oxygenation state. The resulting contrast is commonly referred to as the blood oxygenation level-dependent (BOLD) signal.

1.3.4 Physics of BOLD contrast generation

Alterations of T2 and T2* in regions of the cerebral cortex solicited during information processing hinge on the extent to which phase coherence between spins in these areas is affected by concomitantly-arising hemodynamic changes. Spin dephasing is influenced not only by variations of the concentration of intravascular deoxyhemoglobin, but also by the shape and spatial extent of the susceptibility-induced magnetic field distortions in and around the vessels. (Jezzard *et al,* 2005; Kim *et al*, 2006; Buxton, 2013) To understand the modulatory effect of functional hyperemia on MRI signal attenuation, it is helpful to decompose the BOLD signal into its extravascular and intravascular components and analyze each one separately.

Outside a blood vessel, a spin located at a distance of r from the vessel's center will experience a Larmor frequency shift of:

$$\Delta\omega_{out} = 2\pi\omega_0\Delta\chi_0 Hct(1-Y)\left(\frac{R}{r}\right)^2(\sin\theta)^2(\cos 2\varphi) \qquad \textbf{(1.37)}$$

The contributory elements to equation 1.37 include not only the radius and orientation of the blood vessel, respectively expressed by R and θ, the latter variable representing the angulation of the vessel with respect to the magnetic field lines, but also physiological parameters such as venous blood oxygenation (Y) and hematocrit (Hct). The φ angle is formed by the projection of $\vec{B}_0$'s field lines into the blood vessel's axial plane and the vector separating the spin from the blood vessel's center in this same plane. A graphical representation of the vessel and the geometric parameters influencing the spatial distribution of frequency shifts is offered at figure 11. (Kim *et al*, 2006; Berman, 2012)

A closer examination of equation 1.37 also reveals that the frequency shift engendered by these distortions is maximized when the vessel is perpendicular to the main magnetic field (θ = 90°) and non-existent for vessels parallel to $\vec{B}_0$ (θ = 0°). All these factors contribute to the distortions adopting a dipole-like shape around the vessel, as depicted in figure 12. (Buxton, 2009; Buxton, 2013) Additionally, spins located at an angle of φ = ± 45° experience no frequency shift as the magnetic field will remain undistorted in these directions.

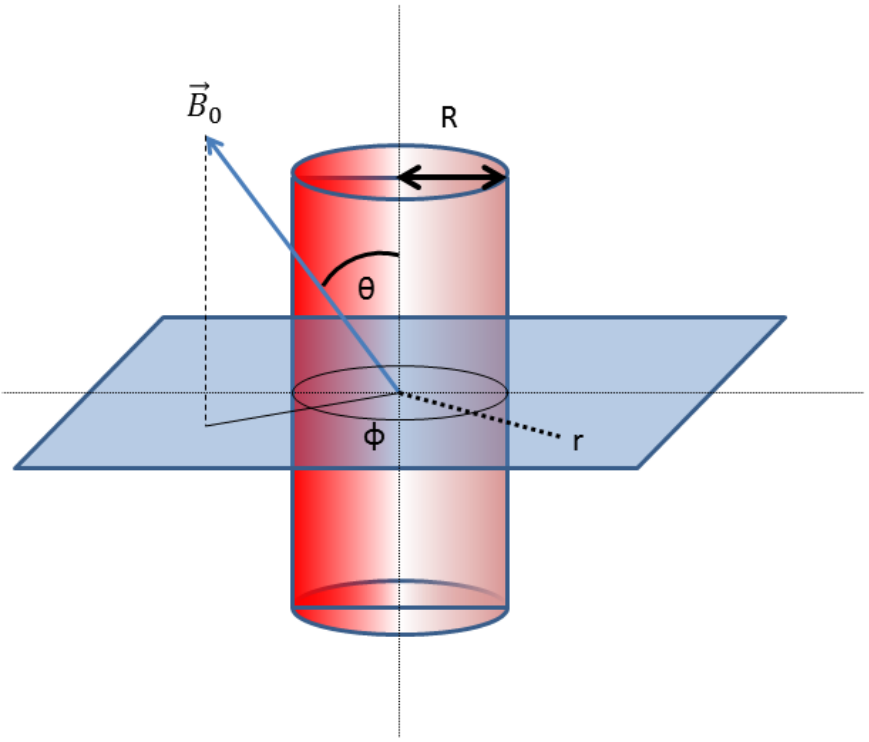

Figure 11: Diagram of a venous blood vessel modelled as a cylinder of infinite length with a radius of* R *oriented at an angle* θ *with the main magnetic field lines. Given a susceptibility difference of* Δχ *between the interior of the vessel and its surroundings, a spin located at a distance* r *from the center of the vessel's lumen and oriented at an angle* φ *from the projection of* B_0 *into the vessel's axial plane will experience a frequency shift given by Eq. 1.37. Figure adapted from (Kim* et al*, 2006; Berman, 2012)

The resulting loss of phase coherence between spins in the extravascular compartment, however, is tempered by the Brownian motion of water molecules. The movement of spins in their environment can be mathematically described as a Gaussian random walk process with a mean centered at $x = 0$ and a variance that can be expressed by:

$$\sigma^2 = 2Dt \qquad \textbf{(1.38)}$$

D represents the diffusion coefficient and t, the time length over which random walk is chronicled. To estimate the distance travelled by one particle during the time that separates excitation from signal acquisition, t can be substituted by the imaging technique's TE. However, this form of the distribution's variance is applicable only for movement along one axis of space. When motion in all three dimensions is considered, the distance travelled by the particle can be

estimated using $6Dt$. (Uludag *et al*, 2005) As the frequency shift perceived by the spin does not change as it travels along the length of the vessel, only movement in the vessel's axial plane will be considered when discussing dephasing. In this case, the travelled distance can be estimated by $4Dt$. (Buxton, 2009)

The diffusion coefficient also affects the characteristic diffusion time, τ_D, which represents the time needed for a spin to traverse a distance comparable to the size of the magnetic field distortions generated around the vessels due to the presence of intravascular deoxyhemoglobin:

$$\tau_D = \frac{R^2}{D} \tag{1.39}$$

If τ_D is found to be much longer than TE, spins can effectively be considered static and will therefore be subjected to what can be considered a constant frequency shift. Conversely, when τ_D is much shorter than TE, spins will dynamically average the magnetic field by sampling all of the frequency shifts generated around the blood vessel. This will cause all spins located in the regions of field inhomogeneity to accumulate approximately the same amount of phase. When all spins possess the same phase history, signal attenuation is lessened due to a reduced loss of phase coherence; molecular diffusion will effectively narrow the phase distribution of these spins over the course of the TE. (Uludag *et al*, 2005; Kim *et al*, 2006)

Molecular diffusion also plays an important role in MRI signal attenuation in the intravascular compartment. When bound to deoxyhemoglobin, erythrocytes will generate steep susceptibility-induced field gradients in their immediate surroundings. Because of the size of these field perturbers, τ_D will be short enough to allow blood water spins to dynamically average the magnetic field offsets as they diffuse in and out of the red blood cells. At any point inside the vessel, the frequency shift experienced by blood water spins is expressed by:

$$\Delta\omega_{in} = 2\pi\omega_0\Delta\chi_0 Hct(1-Y)((\cos\theta)^2 - 1/3) \tag{1.40}$$

The frequency shifts generated by multiple randomly-oriented blood vessels within a voxel will be summed, leading to a regional decrease of T2*. (Kim *et al,* 2012)

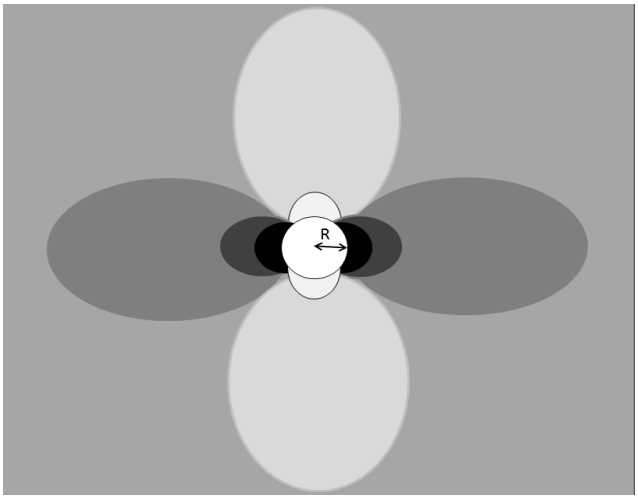

Figure 12: Graphical representation of the magnetic field distortion pattern generated by the passage of paramagnetic deoxyhemoglobin within a blood vessel. The bright and dark regions represent regional increases and decreases of the magnetic field strength. **B_0** ***remains undistorted along lines oriented at ± π/4.*** **R** ***represents the vessel's radius. Figure adapted from (Buxton, 2009)***

The contribution of the susceptibility effects produced by the fluctuating concentration of deoxyhemoglobin during periods of neuronal activation to the transverse relaxation time of a voxel is encompassed by the time constant $R2_{dHb}$. This time constant is added to brain tissue's intrinsic relaxation rate, R2, to obtain the effective relaxation rate R2*, as per equation 1.22. Using Monte Carlo simulations, $R2_{dHb}$ has been found to be equal to:

$$R2_{dHb} = k * vCBV * \{\omega_0 \Delta\chi_0 (1 - Y)\}^{\gamma} \quad \textbf{(1.41)}$$

Where k and γ are constants and $vCBV$ represents the volume fraction occupied by venous blood in the voxel. The value attributed to γ depends on the field strength and takes into account the dephasing effects originating in both the intravascular and extravascular compartments. For B_0 with a magnitude of 1.5 T, γ is equal to 1.5 whereas a value of 1.3 is used when studying the dephasing effect in a pixel for a magnetic field strength of 3 T. (Berman, 2012) However, the values taken on by γ will also differ depending on the preponderant mechanism of spin dephasing responsible for signal attenuation. When only static dephasing (τ_D << TE) is considered, γ is equal to 1. In the motional narrowing regime (τ_D >> TE), γ is equal to 2. (Kim *et al*, 2006)

The static dephasing regime can also be more formally defined by the product of a spin's τ_D and the characteristic frequency of the magnetic field perturber, $\delta\omega_0$. In the context of BOLD signal generation, the blood vessels act as the field perturbers and can be modelled as cylinders of infinite length. (Yablonskiy *et al*, 1994) For this geometry, the characteristic frequency is equal to the frequency shift experienced by a spin located on the surface of a vessel placed in a magnetic field with an orientation of $\theta = 0°$:

$$\delta\omega_0 = 2\pi\gamma B_0 \Delta\chi_0 Hct(1 - Y) \quad \textbf{(1.42)}$$

A spin is considered to have entered the static dephasing regime if the following condition is met:

$$\delta\omega_0 * \tau_D \gg 1 \quad \textbf{(1.43)}$$

Another key difference between the static dephasing and motional narrowing regime is that the effects of static dephasing can be reversed through the application of a 180° refocusing RF pulse. When spin-echo imaging techniques are employed, spins experiencing a constant field offset will accumulate an amount of phase φ_1 over the first half of TE, before the refocusing pulse is applied. During the second half, the spins will accumulate an amount of phase φ_2 which is equal to $-\varphi_1$, thus rendering their net phase gain equal to zero. In the motional narrowing regime, however, the stochastic nature of molecular diffusion will impact a spin's phase accrual. In this situation, it is possible that the average field experienced by the spin during its random walk over the first half of TE will not be equal to that experienced during the second half. When φ_1 is not equal to φ_2, the dephasing effects are only partially cancelled out by the refocusing pulse. (Uludag *et al*, 2005) This incomplete rephrasing manifests itself as a shortening of the tissue's T2 whereas the effects of static dephasing are encompassed by R2', as described in sub-section 1.1.5. The difference between these contributions to the effective relaxation rate makes it possible to describe $R2_{dHb}$ as the sum of two new relaxation rates (Buxton, 2013):

$$R2_{dHb} = \Delta R2 + R2' \quad \textbf{(1.44)}$$

The difference between these two forms of additional relaxation has important implications for BOLD contrast generation in T2*- and T2-weighted images and will directly

impact the sensitivity and specificity of gradient-echo and spin-echo imaging techniques in BOLD fMRI.

1.3.5 Gradient-echo and spin-echo BOLD fMRI

In BOLD fMRI experiments, GRE imaging techniques are commonly employed due to their ease of implementation and their high sensitivity towards T2* effects generated by deoxyhemoglobin. The latter feature results in an elevated BOLD contrast-to-noise ratio (CNR), an advantage which is counterbalanced by the diminished spatial specificity of GRE BOLD relative to SE BOLD. (Norris, 2012)

Due to the anatomical and physiological correlation between brain parenchyma and capillary beds, it is accepted that signal change detected in the extravascular space surrounding the brain's microvasculature is specific to the site of neuronal activity. (Lee *et al,* 2002; Glielmi *et al*, 2010) However, spins located in and around macroscopic vessels will also contribute to BOLD contrast generation when gradient-echo imaging techniques are employed. This is due to functional hyperemia driving out the deoxygenated blood from capillaries and veinules and into large draining veins which may be distal to the sites of synaptic activity. Detection of signal change in these regions reduces the specificity of gradient-echo imaging techniques in BOLD fMRI. (Harmer *et al*, 2012) However, due to the proportional relationship between the radii of these vessels and τ_D, spins located in the susceptibility-induced field distortions generated by large draining veins will primarily undergo static dephasing. As a result, the additional relaxation effects perceived by spins at these locations can be eliminated using a refocusing pulse, rendering spin-echo imaging more specific to the microvasculature at the expense of decreased sensitivity towards BOLD signal. (Norris *et al*, 2002)

It has been shown that around capillaries, dynamic averaging is the main contributor to the increase of the relaxation rate; ΔR2 becomes maximal for vessels with radii between 5 and 8 μm. (Bandettini *et al*, 1994; Jezzard *et al*, 2005; Buxton, 2009) Past this size, ΔR2 begins to decrease while R2' continues to grow, eventually reaching a point where all additional relaxation in the extravascular compartment is caused by static dephasing. However, the extravascular

BOLD effect around vessels such as capillaries will scale quadratically with $\vec{B}_0$'s magnitude, as opposed to signal changes occurring around draining veins, which increase linearly alongside the magnetic field strength. The latter phenomenon results in an improved sensitivity for spin-echo BOLD at ultra-high fields. (Lee *et al*, 1999; Harmer *et al*, 2012; Budde *et al*, 2014)

While spin-echo imaging is thought to permit a better localization of the regions of activation due to the removal of the effects of static dephasing, it is important to remember that BOLD signal presents an intravascular component that cannot be refocused. This is a potentially confounding factor in spin-echo BOLD as signal change can still be detected within large draining veins, even if the extravascular effect around these vessels is eliminated. (Uludag *et al*, 2005) Large fluctuations in signal intensity arise from within the vessels during periods of neuronal activity due to the quadratic relationship between blood water T2 and venous oxygenation. (Kim *et al*, 2006; Buxton, 2013) This relationship is a product of the dynamic averaging of magnetic field offsets generated around red blood cells by spins in blood plasma and can be expressed as:

$$\frac{1}{T2} = A_0 + K(1 - Y)^2 \qquad \textbf{(1.45)}$$

In the equation above, A_0 is an invariant constant while K also scales quadratically with the magnitude of $\vec{B}_0$. At low magnetic field strengths (e.g. 1.5 T), it has been shown that intravascular signal change in macroscopic vessels is the dominant mechanism behind BOLD contrast generation. (Boxerman *et al*, 1995; Oja *et al*, 1999) In BOLD fMRI experiments carried out at ultra-high field strengths, however, the T2 of blood water is much shorter than conventionally employed TEs, which are set to the T2 or T2* of gray matter to maximize functional SNR for spin-echo and gradient-echo imaging techniques (Bandettini *et al*, 1994; Bernstein *et al*, 2004), significantly reducing its contribution to the overall BOLD signal.

Various solutions have been proposed to lessen the impact of the intravascular BOLD effect in fMRI studies in which high spatial specificity is required. Post-processing methods involving the creation of cerebral venograms from susceptibility-weighted images of the brain can be used to locate and exclude large draining veins from future analyses. Diffusion weighting can also be used to reduce the impact of the intravascular BOLD effect by inducing velocity-

dependent phase shifts for water molecules flowing through the circulatory system, accelerating signal decay in this compartment. (Lee *et al,* 1999; Duong *et al*, 2003)

1.3.6 Echo planar imaging

Due to the transient nature of the hemodynamic response to neuronal activation, fast imaging techniques are used in functional MRI experiments to rapidly generate images of the brain. Echo planar imaging (EPI) is among the most common of these techniques and allows for the creation of images within milliseconds. To fill the entirety of k-space, EPI makes use of a train of readout gradients with rapidly-alternating polarities in order to produce several signal echoes in quick succession. (Huettel *et al*, 2014) Phase encoding is accomplished by either applying a constant gradient G_y over the course of the readout period or, more frequently, through a series of gradient "blips" applied between each one of the readout gradient train's lobes. Using the latter phase-encoding scheme results in a zipper-like traversal of k-space, in which the lines of the acquisition matrix are filled in a back-and-forth manner. This trajectory and its corresponding pulse sequence diagram are depicted at figure 13. (Bernstein *et al*, 2004)

Despite permitting a substantial increase in acquisition speed, EPI is prone to a number of artifacts due to its design. The rapid flipping of gradient polarity during the readout period, for example, generates eddy currents which will delay the generation of gradient fields and add phase shifts to the acquired data by modulating $\vec{B}_0$'s magnitude. These phenomena introduce asymmetry between even and odd lines of k-space, resulting in the formation of Nyquist ghosts on the image. These ghosts are low-intensity copies of the target structures that are shifted by one-half of the field of view relative to the actual structures within the image. For this reason, these artifacts are also called N/2 ghosts, with N being equal to the size of k-space in the phase-encoding direction. (Giannelli *et al*, 2010)

Images acquired using EPI are also susceptible to geometric distortion, which causes the target structures to appear stretched, compressed or sheared on the images. Broad magnetic field gradients formed within the magnetized object that encompass multiple voxels are responsible for this phenomenon. These large zones of magnetic field inhomogeneity will apply a constant field offset for all spins within a voxel and modify the resonance frequency of the targeted spin

species in a given region. Because the spatial encoding process depends on the alteration of Larmor frequencies through the use of the scanner's field gradients only, the uniform field offset brought on by large-scale magnetic field inhomogeneity leads to errors during the spatial encoding process and results in inaccurate mapping of the acquired signals. (Uludag *et al*, 2005)

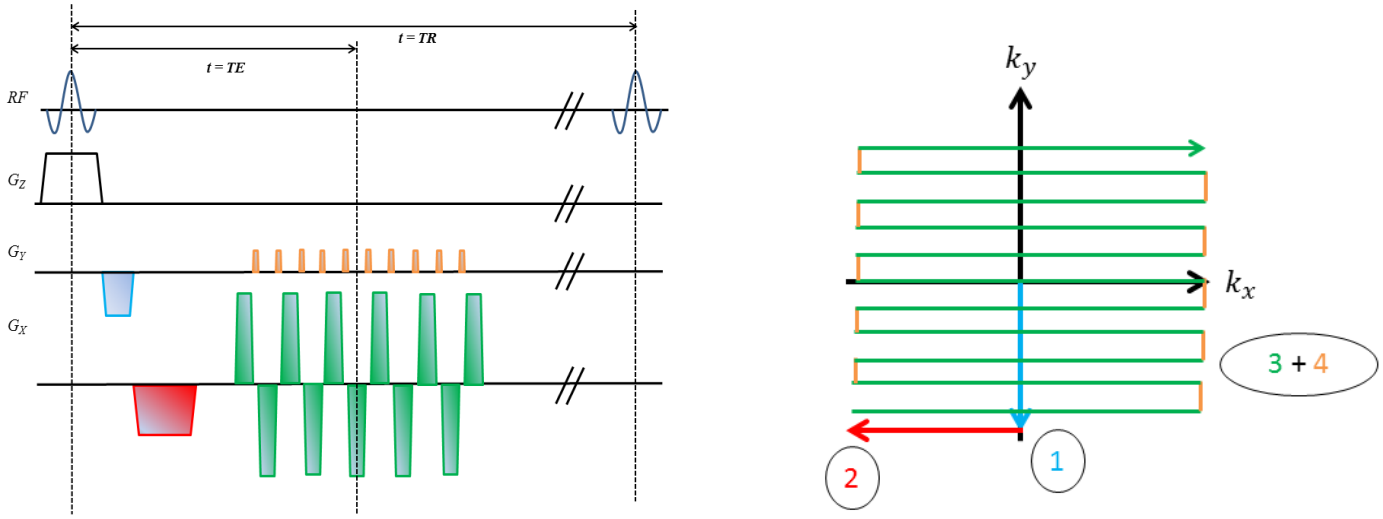

Figure 13: Left – Pulse sequence diagram depicting GRE echo-planar imaging (EPI). Right – Corresponding k-space trajectory. EPI allows for the acquisition of the entirety of k-space in a single TR due to the successive generation of echoes produced by rapid gradient flipping.

1.3.7 Perfusion imaging and arterial spin labelling

While BOLD signal detection methods have been widely adopted in fMRI to investigate brain activity, perfusion can also be used as an indicator of neuronal activation due to changes in CBF being linearly correlated with changes in CMR_{glu}. (Faro *et al*, 2011) Changes in CBF have also been shown to be well-correlated with BOLD signal changes in brain parenchyma during episodes of neuronal activity, making perfusion-based methods more specific to the sites of synaptic activity. (Glielmi *et al,* 2010) Different methods have been proposed for detecting changes in CBF using MRI, such as dynamic susceptibility contrast (DSC) imaging and arterial spin labelling (ASL). The former approach involves the injection of a paramagnetic contrast agent such as gadolinium into the bloodstream, which will affect transverse relaxation times, much like deoxyhemoglobin, consequently affecting signal intensity on the resulting images. (Shiroishi *et al*, 2015)

The contrast agent's impact on the relaxation times is proportional to its concentration, which is in turn related to the blood volume. By combining this estimation of blood volume with knowledge of tracer kinetics, it becomes possible to obtain a measurement of CBF. However, DSC presents many disadvantages, the most notable of which being its invasiveness as well as the vulnerability of the analysis technique used for CBF quantification to noise. (Wong, 2014; Shiroishi *et al*, 2015)

In ASL, blood water itself is used as the tracer; RF pulses are used to label (or "tag") blood water spins, i.e. invert their longitudinal magnetization, as they flow through the arterial compartments of the circulatory system. A post-label delay (PLD) is then played out to allow the tagged spins, whose longitudinal magnetization will decay according to the T1 value of blood, to enter the brain's microvasculature and diffuse into extravascular space before acquiring the images. As rapid image acquisition is required in ASL due to the short T1 values of blood, EPI is often used for this purpose. (Alsop *et al*, 2015; Mota Nunes, 2015) Because tagged and untagged water spins are mixed together in the imaging slab during a spin tagging experiment, there is a decrease of MRI signal intensity relative to a scan where no tagging occurs due a decrease in the overall longitudinal magnetization of tissue water. (Liu *et al*, 2007)

In the following measurement period, a second set of brain images are acquired without spin tagging; this is known as the control condition. The two sets of images are then subtracted to remove the signal emanating from static tissues in order to obtain an image of the signal difference (ΔM) caused by the presence of tagged spins. ΔM is directly proportional to CBF, which can be quantified using mathematical models describing the exchange of water spins between the intra- and extravascular compartments. (Buxton *et al*, 1998; Debacker, 2014; Alsop *et al*, 2015) The facility with which physiological information is obtained using perfusion-based methods is an advantage over BOLD fMRI, in which the functional contrast borne out of susceptibility-induced signal changes depends on a multitude of physiological parameters.

ASL methods can be classified according to how their tagging schemes are implemented. Pulsed and continuous ASL (PASL and CASL) were the original methods by which changes in CBF were imaged in MRI, but pseudo-continuous ASL (pCASL) has emerged as a viable alternative in recent years. The functionality of these three methods will be explored in the following sub-section alongside their advantages and drawbacks.

1.3.8 CASL

Continuous spin tagging was the first method proposed for conducting ASL and relies on the use of lengthy inversion pulses applied concomitantly with a linear magnetic field gradient of constant amplitude oriented in the direction of blood flow. For cerebral imaging, a magnetic field gradient is applied along the length of the body as the internal carotids and vertebral arteries are parallel to $\vec{B}_0$. The frequency of the RF pulse is tuned so as to affect flowing spins at a region upstream from the imaging slab during the tagging experiment. In the presence of a magnetic field gradient, this results in the formation of a labelling plane whose thickness is dependent on the aforementioned gradient's amplitude. In the control experiment, the frequency shift applied to the inversion pulse is multiplied by -1 in order to place the labelling plane outside the skull, at a location that is symmetrically opposed to the one occupied during the tagging period with respect to the center of the imaging slab. (Bernstein *et al*, 2004; Debacker, 2014) This process is illustrated on figure 14.

The longitudinal magnetization of arterial spins is modulated by a process known as adiabatic flow-driven inversion. To understand this technique, it is helpful to utilize the notation scheme presented in sub-section 1.1.4 to describe the effect of the inversion pulse in the rotating frame of reference. In this referential, the tagging pulse's B_1 acts as $\vec{B}_{eff}$'s transverse component, as expressed by equation 1.14. As blood water spins flow in the direction in which the magnetic field gradient is applied, they will experience a sweep of resonance frequencies which will in turn impact the longitudinal component of the effective magnetic field. Spins located far away from the labelling plane will experience a Larmor frequency offset large enough to dwarf the tagging pulse's effect, keeping their magnetization parallel to $\vec{B}_0$. As they move closer to the labelling plane, $\vec{B}_{eff}$'s longitudinal component will begin to shrink, tipping the effective magnetic field into the transverse plane. The resonance condition is fulfilled as spins pass through the labelling plane's center and $\vec{B}_{eff}$ begins to adopt an antiparallel conformation with respect to $\vec{B}_0$ as the spins move further away. The magnetization vector will follow the rotation of the effective magnetic field only if the adiabatic condition, which states that changes in $\vec{B}_{eff}$'s orientation must remain small over the course of one period of precession, is fulfilled. Mathematically, this condition can be expressed as:

$$1 \ll \frac{\gamma|\vec{B}_{eff}|}{|d\Psi/dt|} \quad \textbf{(1.46)}$$

In this equation, the denominator represents the rate of change in $\vec{B}_{eff}$'s orientation and Ψ represents the angle formed between $\vec{B}_{eff}$ and the z-axis of the rotating referential. (Bernstein *et al*, 2004)

Unfortunately, hardware constraints limit the duration over which RF pulses can be applied, hampering the implementation of CASL sequences on conventional scanner hardware. Although lengthy inversion pulses help ensure the delivery of large quantities of tagged blood to the microvasculature, resulting in an increased ASL SNR, they are also responsible for high specific absorption rates (SAR) due to the significant amount of energy deposited into biological tissues during the scan session. Additionally, these RF pulses are responsible for the generation of magnetization transfer (MT) effects, which degrade image quality and compromise CBF quantification if not properly controlled for. (Detre, 2008)

Water spins bound to macromolecules have a large frequency spectrum and can be excited by the application of an off-resonance RF pulse. In CASL, this occurs due to the tagging pulse producing off-resonance excitation in the imaging slab in the presence of a weak magnetic field gradient. The longitudinal magnetization of spins in the so-called macromolecular pool becomes saturated and is then exchanged with spins in the liquid pool, i.e. unbound water spins, resulting in MRI signal attenuation. MT effects appear on both the tag and control images and if the control scan is performed as described earlier in this section, they can be removed by image subtraction for a single-slice experiment. Advanced correction techniques are needed for multi-slice CASL, as MT effects will normally only be removed for one imaging plane; all slices other than the one at the center of the imaging slab will be marred by these effects and the corresponding subtraction images will present an additional amount of attenuation due to MT effects. (Bernstein *et al*, 2004; Debacker, 2014)

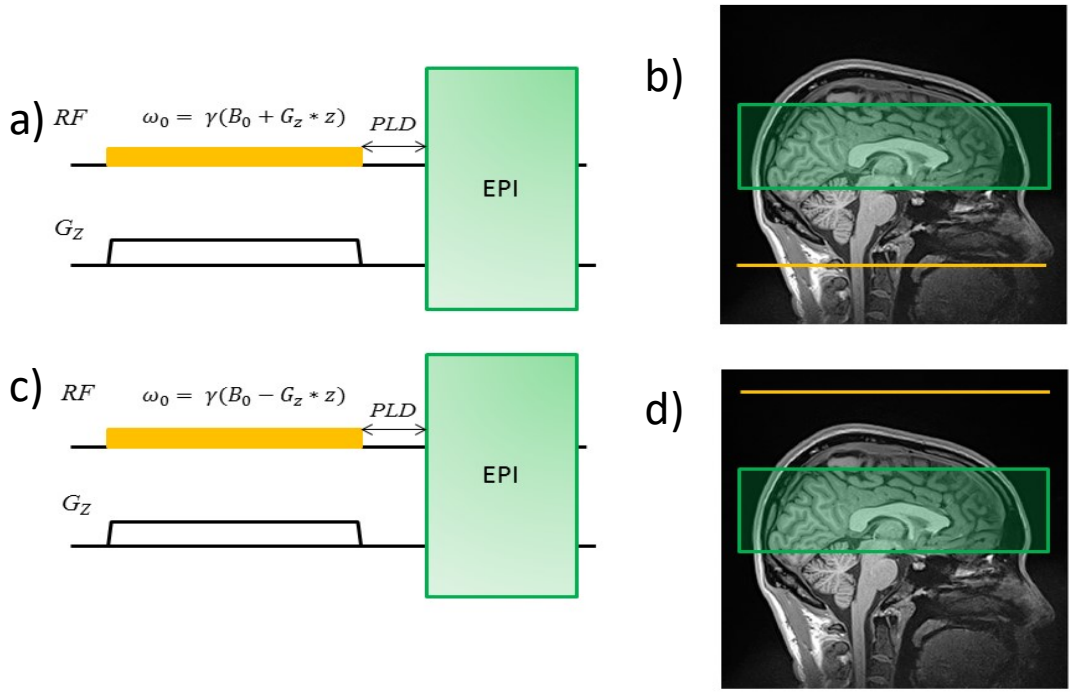

Figure 14: Illustration of the CASL technique. a) Simplified pulse sequence of the tagging experiment used in CASL. EPI designates the readout module incorporated into the CASL sequence. b) Graphical representation of the elements used for perfusion imaging using CASL. The labelling plane is shown in orange and is positioned in a region upstream from the organ to be imaged. The image volume is shown in green. c) Simplified pulse sequence of CASL's control experiment. The resonance frequency of the tagging pulse is adjusted to as to place the labelling plane in a region that is symmetrically opposed to its position during the tagging experiment relative to the center of the image volume, as shown in d). Figure adapted from (Debacker, 2014)

1.3.9 PASL

In contrast to CASL, pulsed spin tagging methods make use of RF pulses with a short duration to adiabatically invert blood water spins in a given volume. These pulses, which are often characterized by a hyperbolic secant shape, are amplitude-modulated and frequency-modulated to meet the adiabatic condition stated in equation 1.46. This will also render the pulses impervious to B_1 inhomogeneity, allowing for a uniform inversion of spins across the labelling area. Many different types of PASL sequences exist, such as EPISTAR, FAIR and PICORE, and differ from each other in terms of the design of their labelling and control experiments. (Bernstein *et al*, 2004)

In EPISTAR, a slice-selective inversion pulse will affect spins in an area located directly upstream from the imaging slab during the tagging experiment. This labelling area is shifted to a

region directly downstream from the region of interest during a control acquisition, much like in the CASL sequence described in the previous section. Care must be taken to make sure that the edges of the labelling region and the imaging slab do not overlap; while it is desirable for these regions to be contiguous, the imperfect slice profiles of the inversion and excitation pulses makes it necessary to verify their spacing. The tagging process used in PICORE is the same as for EPISTAR, but the inversion pulse is played out in the absence of the slice-selection gradient during the control measurements, leaving the spins unaffected. FAIR is different from these methods and uses a non-selective RF pulse to invert all spins during the tagging session while a slice-selective pulse is applied at the level of the imaging slab during the control period. Despite the differences between these techniques, their performance has been found to be comparable, with minor caveats. (Wong *et al*, 1997) Diagrams illustrating the tagging and control periods of a PICORE-type PASL sequence are presented at figure 15.

Pulsed spin tagging also overcomes the principal limitations of CASL, such as the elevated SAR associated with its use as well as its vulnerability to MT effects. (Wong, 2014; Debacker, 2014) The use of short inversion pulses in the tagging experiment will result in less energy being deposited into the patient's biological tissues, as opposed to CASL, where pulses on the order of a few seconds are required for adiabatic flow-driven inversion. The avoidance of MT effects in PASL makes this technique especially well-suited for multi-slice perfusion imaging. The short duration of the pulses used in PASL also grant this sequence the advantage of being easier to implement on MRI scanners due to the facility with which the hyperbolic secant pulses can be played out on conventional scanner hardware.

Similarly to CASL, a delay, known as the inversion time TI, is inserted between the end of the tagging period and the start of the image acquisition period to grant the inverted spins enough time to enter the imaging slab. However, the temporal width, i.e. duration, of the bolus of blood generated using pulsed tagging is not as well-defined as in CASL, leading to possible errors in CBF quantification due to a lack of knowledge of tracer kinetics. Specifically, if the duration of the tagged bolus remains unknown, it becomes difficult to select an appropriate delay time that allows for the complete evacuation of the bolus from the labelling region and into the imaging slab. Unlike continuous tagging, where the duration of the bolus is equal to that of the tagging pulse, the application of a short 180° inversion pulse in PASL results in the creation of a

bolus with fixed volume, whose kinetics depends on the subject's physiology. Changes in global blood flow, for example, will alter the duration of the bolus in a way that is unknown to the experimenter. Additionally, blood flow can vary from one feeding artery to the next within the labelling region, further modifying tracer dynamics and complicating CBF quantification. (Buxton, 2009)

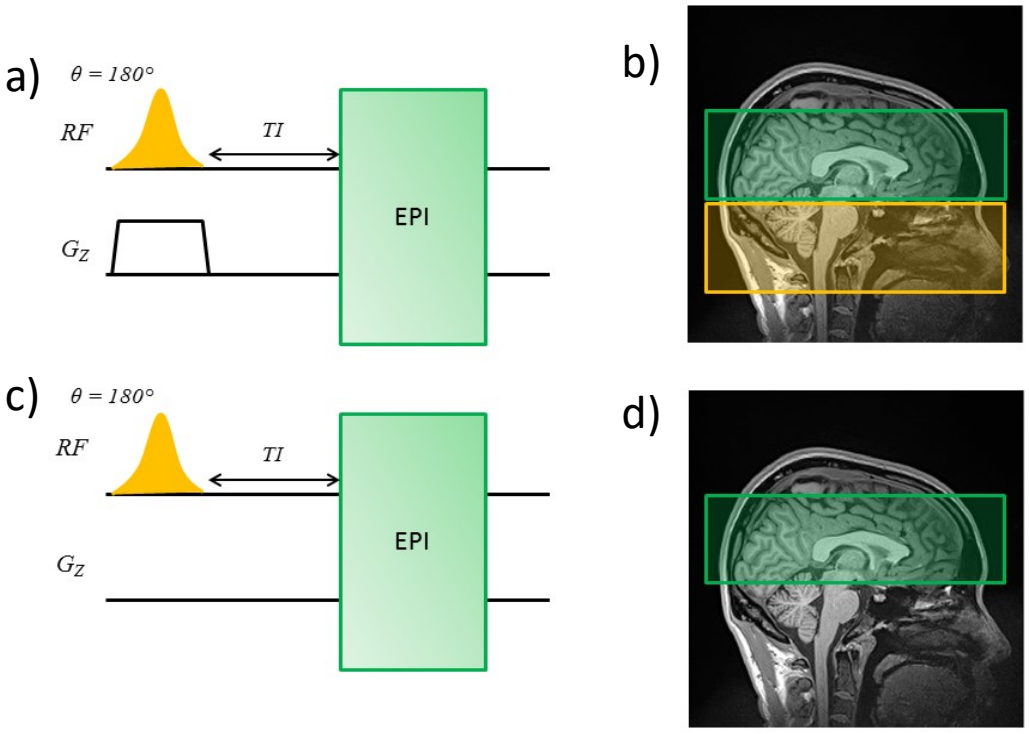

Figure 15: Illustration of a PICORE-type PASL technique. a) Simplified pulse sequence diagram of the tagging experiment used in a PICORE sequence. An inversion pulse is played out with a flip angle of 180° in order to modulate the longitudinal magnetization of flowing spins in a volume located upstream from the imaging slab. EPI designates the readout module incorporated into the sequence. b) Graphical representation of the elements used for spin tagging using this sequence. The image volume is shown in green while the tagging volume is displayed in orange. c) In PICORE-type PASL, the slice-selective gradient is either turned off (as shown above) or shifted in time to prevent the inversion pulse from affecting blood water spins during the control experiment, leading to the absence of the tagging volume in d). Figure adapted from (Debacker, 2014)

To remedy this problem, techniques such as QUIPSS II and Q2TIPS have been developed to give the blood bolus a precisely-defined duration by "cutting off" the tail end of the bolus. In QUIPSS II, a 90° RF pulse is applied at a time TI_1 from the peak of the inversion pulse at the level of the tagging region to saturate the magnetization of spins located in this area. The imaging process begins at time TI_2 from the peak of the inversion pulse. Both inversion times are defined by the user at the outset of the experiment. In Q2TIPS, the single saturation pulse is

replaced by a train of similar pulses applied to the extremity of the labelling region closest to the imaging slab. These pulses demonstrate both better B_1 homogeneity and selectivity than the single saturation pulse used in QUIPSS II, making Q2TIPS an advantageous choice for perfusion imaging experiments using PASL. (Luh *et al*, 1999)

Despite this modification, the bolus created using pulsed tagging is generally shorter than the one created using continuous tagging, leading to a smaller volume of tagged blood penetrating the imaging slab, which results in a lower SNR for this form of ASL. PASL, however, still retains the advantage of being characterized by a greater inversion efficiency than CASL due to the latter's inversion process being sensitive to variations in blood flow velocity. (Pollock *et al*, 2009; Wong, 2014)

1.3.10 PCASL

Pseudo-continuous ASL is a reinvention of CASL which conserves the benefits of this technique while overcoming its principal limitations. The name of this technique comes from the fact that the long inversion pulse used for adiabatic flow-driven inversion is broken down into a train of short, equally-spaced RF pulses. Similarly, the constant field gradient also undergoes a transformation into a series of slice-selection and spoiler gradients with uneven moments and alternating polarities. The imbalance between the slice-selection gradient lobes and the spoiler gradient lobes, the latter of which are played in the time separating two tagging pulses, is necessary to replicate the conditions needed for spin tagging in CASL. Specifically, the average gradient strength associated with the gradient waveform used during the tagging portion of a pCASL sequence must be made equal to the amplitude of the constant gradient deployed in CASL. A similar condition exists for the average B_1 value generated by a pCASL sequence's train of labelling pulses, dictating that it must be equal to the amplitude of B_1 associated with the inversion pulse used for continuous spin tagging. (Wu *et al*, 2007; Dai *et al*, 2008)

During the labelling experiment, off-center inversion of flowing spins will cause them to experience a phase shift in the time separating two successive tagging pulses due to the imbalance between the moments of the slice-selection and spoiler gradients. For the longitudinal magnetization of flowing spins to be inverted as they pass through the labelling plane, the phase

of each RF pulse must be synced to the spins' phase accumulation schedule. As the phase shift applied to blood water spins is position dependent, the phase increment added to each tagging pulse is a function of the distance separating the labelling plane from the isocenter of the scanner's magnet. (Wu *et al*, 2007; Dai *et al*, 2008; Jahanian *et al*, 2011) A simplified pulse sequence depicting the tagging portion of a pCASL experiment is presented at figure 16.

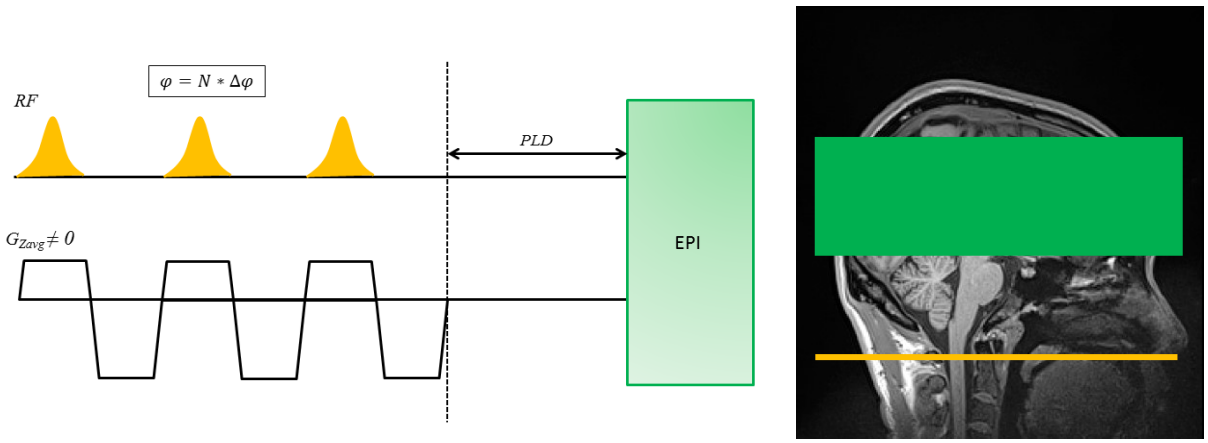

Figure 16: Illustration of a pCASL sequence's tagging mechanism. Left - The long RF pulse and magnetic field gradient used for flow-driven adiabatic inversion of blood water spins are respectively replaced by a train of short and equally-spaced tagging pulses and a waveform composed of slice-selection and spoiler gradients with unequal moments and alternating polarities. The average gradient strength produced at this time is similar to the gradient amplitude used in CASL. A phase increment is successively added to each tagging pulse to ensure that their phase schedule matches that of the flowing spins. EPI designates the readout module incorporated into the pulse sequence. Right- Graphical representation of the elements used for spin tagging in a pCASL sequence. The labelling plane appears in orange while the image volume is shown in green. Figure adapted from (Debacker, 2014)

The control experiment can be carried out in one of two ways depending on whether the pCASL sequence is implemented in the balanced configuration or in the unbalanced configuration. This appellation refers to the discrepancies between the shapes of the gradient waveforms used during the labelling and control measurements. In the unbalanced configuration, the spoiler gradient's moment is adjusted so as to produce an average gradient strength of zero over one peak-to-peak RF pulse cycle. Additionally, the phase of each tagging pulse is set to alternate between 0° and 180° in order to obtain a mean B_1 value of zero during this time. This modification is made to ensure that no inversion occurs during a control measurement while still controlling for MT effects. (Dai *et al*, 2008) In the balanced configuration, the gradient waveform does not change between the labelling and control measurements, thereby generating a non-null G_z during the control period. To ensure that the RF pulse train does not perturb the

longitudinal magnetization of flowing spins at this time, additional phase offsets of 180° are added to the phase increment normally applied to each pulse in the labelling condition. (Shin *et al*, 2012)

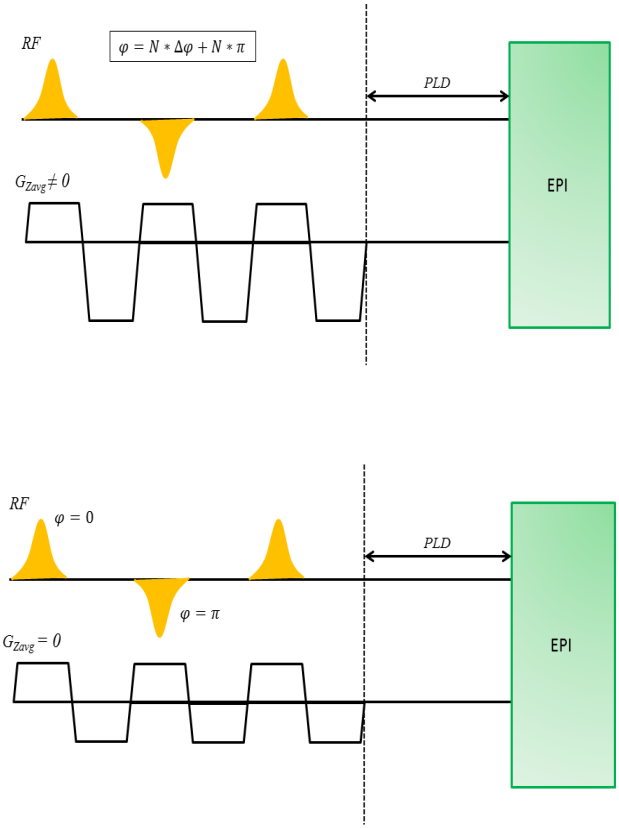

Figure 17: Pulse sequence diagrams of the control experiments carried out in balanced (top) and unbalanced (bottom) pCASL sequences. In the balanced variant, the gradient waveform does not change between the tagging and control measurements. The phase of each tagging pulse is incremented by the same amount as in the tagging experiment, but with an added offset term of N*π, with N representing the Nth pulse in the train. In the unbalanced conformation, the moments of the spoiler gradients is adjusted in order to produce an average gradient strength of 0 during the control experiment. Additionally, the phase of each successive tagging pulse is made to alternate between 0° and 180° at this time. Figure adapted from (Debacker, 2014)

Due to the similarity between the tagging mechanisms utilized in CASL and pCASL, the latter technique is characterized by the same advantages that CASL possesses compared to PASL, such as heightened SNR and precise control over the temporal width of the tagged bolus. The use of strong slice-selection gradients in pCASL also mitigates the problem of off-resonance excitation which leads to the apparition of MT effects on the final images. (Wong, 2014)

Similarly to PASL, pCASL is easily implemented on MRI scanners due to its use of short RF pulses for spin tagging and is suitable for multi-slice imaging. However, because this technique's labelling process is contingent on the presence of flowing spins, its inversion efficiency can be compromised by variations in blood flow velocity. (Jung *et al*, 2010) The inversion efficiency can also be negatively affected by off-resonance effects, such as the formation of susceptibility gradients, at the level of the labelling plane, with balanced pCASL sequences being particularly sensitive to these phenomena. (Wu *et al*, 2007) Perfusion imaging experiments carried out in mice have shown that unbalanced pCASL offers a better performance in terms of SNR gains than balanced pCASL, (Duhamel *et al*, 2011) but tests carried out in humans have shown that the performances of both variants are comparable and not significantly different from each other. (Mota Nunes, 2015)

Chapter 2. Methodology

In this chapter, the steps taken to design, implement and validate the pulse sequences necessary for this project shall be described in addition to the development of analysis tools required for the pursuit of the objectives put forth in this work.

2.1 Pulse sequence development for investigation of BOLD contrast

2.1.1 Alternating gradient-echo and spin-echo EPI ("GRESE-EPI")

To investigate the performance of GRE and SE imaging techniques in terms of their ability to detect BOLD signal changes, an EPI sequence permitting the interleaved acquisition of image volumes using GRE-EPI and SE-EPI was created. A timing diagram of this sequence, which will henceforth be referred to as gradient-recalled echo and spin-echo EPI or GRESE-EPI in this thesis, is illustrated on figure 18.

A SE-EPI sequence provided by Siemens Healthcare (Erlangen, Germany) was used to construct the GRESE-EPI sequence in the Siemens IDEA pulse sequence programming environment. The implementation of this imaging technique's principal functionalities reposed on two key factors: the transformation of the SE-EPI sequence into a working GRE-EPI sequence and the addition of a mechanism in the sequence's code which would allow the final product to alternate between these two imaging techniques at runtime.

The first step taken to transform the SE-EPI sequence into a GRE-EPI imaging technique was the removal of all elements needed to refocus the magnetization at TE/2 such as the refocusing pulse, its accompanying slice-selection gradient and the crusher gradients that are played before and after the 180° RF pulse used to ensure that the magnetization is perfectly refocused. These elements are then replaced with a delay of equivalent duration in order to preserve the value of TE originally selected for SE-EPI. However, due to the refocusing pulse's effect on the k-space trajectory, as depicted on figure 7, the polarity of the gradients deployed after this event must be adjusted to reflect the changes made to the SE-EPI sequence during its conversion into a GRE-EPI sequence. Specifically, the polarity of the phase blips and the readout

train must allow for the proper traversal of k-space after the application of the phase correction module and prewinder gradients, respectively shown in red and blue in figure 18. The combined effect of these gradients results should result in the signal acquisition process beginning at one of the corners of the acquisition matrix. The phase correction gradients also play an important role in minimizing the intensity of Nyquist ghosts liable to appear on images acquired using EPI. The energy calculation formula was also updated to take into account the removal of the refocusing pulse from the acquisition periods during which GRE-EPI is to be employed. This is necessary to ensure that the SAR is properly calculated at the outset of each scan.

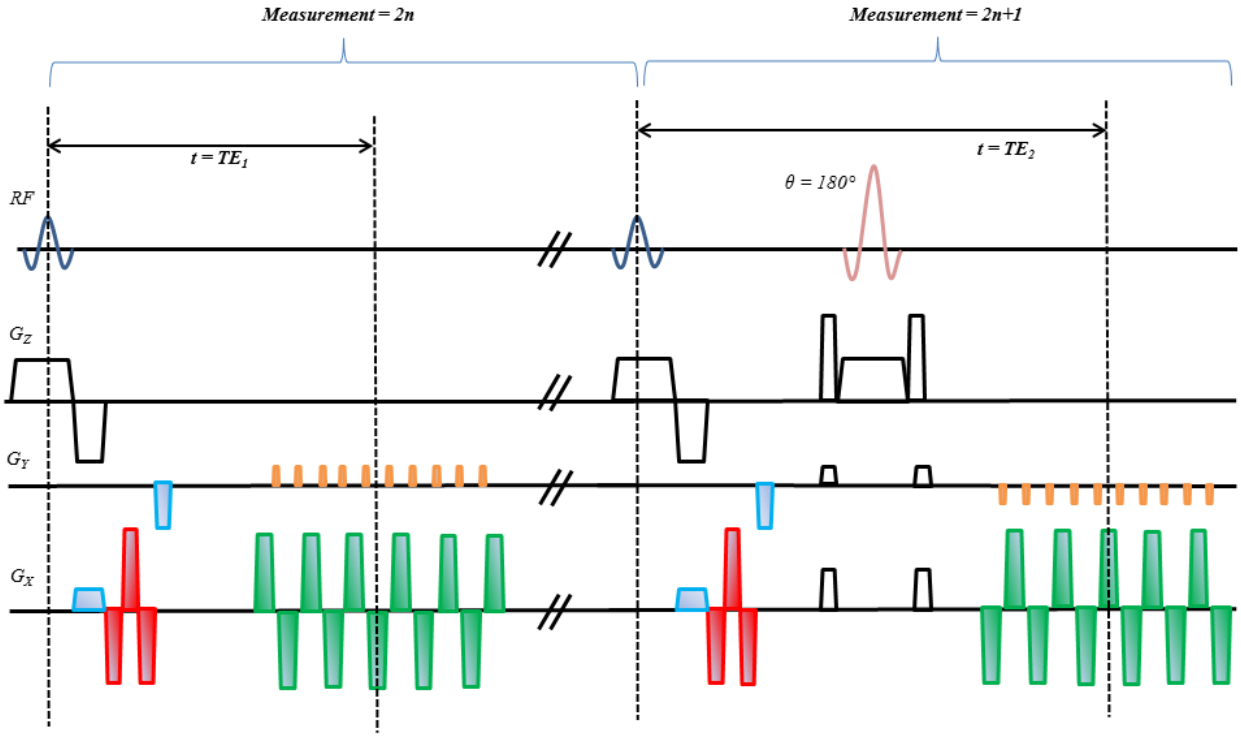

Figure 18: Pulse sequence diagram of the GRESE-EPI sequence developed in this work. This sequence allows for the interleaved acquisition of GRE and SE data by switching between SE-EPI and GRE-EPI during odd-numbered and even-numbered measurement periods, respectively. The measurement number is given by (n+1), where n represents the current repetition and is equal to n = 0, 1, 2, …, N. It is also possible to set the TE for each imaging technique used in GRESE-EPI independently from each other. The TEs used for GRE-EPI and SE-EPI are represented by the variables TE_1 and TE_2. In the diagram shown above, the readout gradients are shown in green and the phase blips are orange. The gradients used for advanced phase correction appear in red and the prewinders are colored blue. The slices-selection gradients are shown as line drawings, as are the crusher gradients which bracket the 180° refocusing pulse.

To switch between SE-EPI and GRE-EPI, a series of conditional statements were used to flip the polarities of the readout and phase-encoding gradients when necessary, in addition to

controlling the application of the refocusing pulse and its accompanying slice-selection and crusher gradients. Using information retrieved from the sequence's repetition counter, it was possible to retain the its original SE imaging functionality during odd-numbered measurement periods while applying the necessary modifications for its transformation into a GRE-EPI sequence during even-numbered measurement periods.

The sequence was then modified even further to allow the user to set separate TE values for its GRE-EPI and SE-EPI components, as indicated by the variables TE_1 and TE_2 in figure 18. This was done by adjusting the delay time played out between the end of the prewinder gradient played out on the phase-encode axis and the beginning of the readout train (in green on figure 18). As the echo time is defined as the time separating the peak of the excitation pulse from the moment at which the center of k-space is acquired, the delay time can be computed using the following equation:

$$Fill\ time = TE_{GRE} - \left(\frac{RF_{duration}}{2} + t_{PhaseCorr} + t_{Prewinder} + \left(\left(\frac{NumRowsKspace}{2}\right) * EchoSpacing + \left(\frac{EchoSpacing}{2}\right)\right)\right) \quad \textbf{(2.1)}$$

The TE value used in this calculation is the value set by the user at the outset of the scan. The durations of the phase correction and prewinder gradients are represented by $t_{PhaseCorr}$ and $t_{Prewinder}$ in the equation above. The time taken to reach the center of k-space from the start of the readout period is obtained by first dividing the total number of rows in the acquisition matrix by 2 and multiplying this number by the time separating the center of one readout gradient lobe from the next, a quantity also known as the echo spacing. A delay of one-half of the echo spacing is then added to this quantity in order to arrive at the center of k-space. This modification was made to control the TE during even-numbered measurement periods, i.e. for GRE-EPI. The TE for SE-EPI could be set using the scanner's normal protocol editor.

Once this development process was completed, GRESE-EPI was used in a pilot BOLD fMRI experiment to test its imaging capabilities. Before the sequence could be installed on the scanner, however, its functionality was validated using the sequence simulation tools and the POET protocol editor available in IDEA to ensure that all elements necessary for image acquisition were played out with the correct values and timing.

2.1.2 Pilot fMRI scans

For this experiment, two healthy young adults (1 male and 1 female between 18 and 35 years of age) were recruited for a BOLD fMRI experiment involving a visual stimulation paradigm. In this block-design trial, a flashing black-and-white checkerboard was used as the stimulus in order to evoke activation in the brain's occipital lobe while a gray background of uniform intensity was used as the control condition. The blocks were presented in a regular alternating manner with the stimulation and resting periods each being 30 seconds long. The parameters used in the fMRI scan protocol are laid out in table 1. Informed consent was obtained in each case and both scans were conducted on a Siemens Magnetom Trio 3T scanner (Erlangen, Germany) at the McConnell Brain Imaging Center at the Montreal Neurological Institute. A 32-channel head coil was used as the receiver element in both scans and the TE for GRE-EPI and SE-EPI were matched.

Table 1: Table of the scan parameters used for the pilot experiments involving GRESE-EPI

Parameters	***Values***
TE (for GRE-EPI and SE-EPI)	36 ms
TR	2000 ms
Receiver bandwidth	2441 Hz/pixel
Flip angle	90°
Matrix size	64 x 64
Field of view	192 mm x 192 mm
Slice thickness	3 mm
Number of slices	30
Distance factor	50% of the slice thickness
Measurements	300
Total scan time	10 minutes

The fMRI scans were preceded by the acquisition of a set of high-resolution T1-weighted anatomical images using an MPRAGE sequence to assist with the positioning of the imaging slab over each participant's visual cortex. The parameters used for this scan were the following: TE = 2.98 ms, TR = 2300 ms, flip angle = 9°, field of view = 240 mm x 256 mm, matrix size =

240 x 256, receiver bandwidth = 238 Hz/pixel, GRAPPA factor = 2, slice thickness = 1 mm, number of slices = 176, distance factor = 50%.

To generate the activation maps, functions available in the Neurolens software package (Montreal, Québec, Canada) were used. However, before computing each subject's activation maps, the raw 4D data was split into two separate 4D datasets containing the image volumes acquired using GRE-EPI and SE-EPI. Each dataset was then subjected to motion correction and spatial filtering using a Gaussian kernel with a FWHM of 6 mm. Once these pre-processing steps were completed, general linear model (GLM) analysis was performed in order to produce t-maps indicating brain activation in response to the visual stimulus.

To carry out this type of analysis for the GRE and SE datasets separately, the duration of the rest and stimulation periods in the original block trial were halved to 15 seconds, reducing the effective scan time for each imaging technique to 5 minutes. A double gamma function was used to model the hemodynamic response function (HRF) and the resulting t-maps were corrected using false discovery rate (FDR) with a threshold of 0.001. The raw EPI images and the corresponding corrected activation maps are shown on figures 19 and 20 for subjects 1 and 2. 3 contiguous slices retrieved from the center of one image volume are shown for both the GRE-EPI and SE-EPI datasets for both subjects.

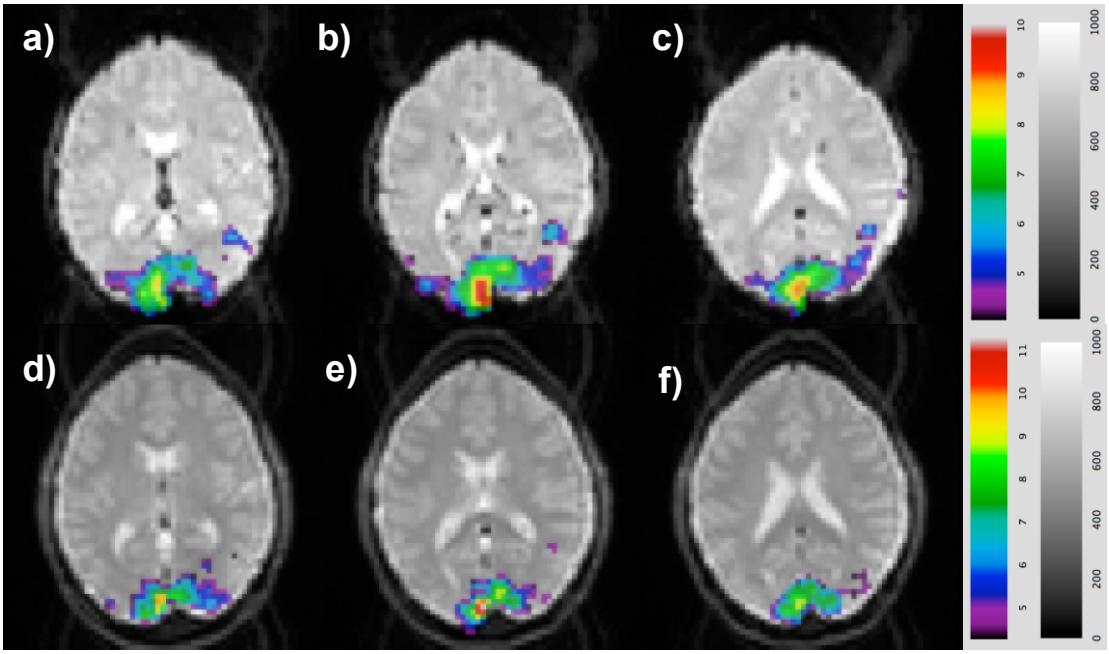

Figure 19: Examples of images acquired using GRESE-EPI for Subject 1 during a pilot fMRI scan involving a visual stimulus. The overlaid activation maps were corrected for FDR with a threshold of 0.001. 3 contiguous slices retrieved from the center of one image volume are shown here for GRE data (a, b, c) and SE data (d, e, f). The color bars indicate the t-score values and the greyscale bar indicates the signal intensity of the underlying images.

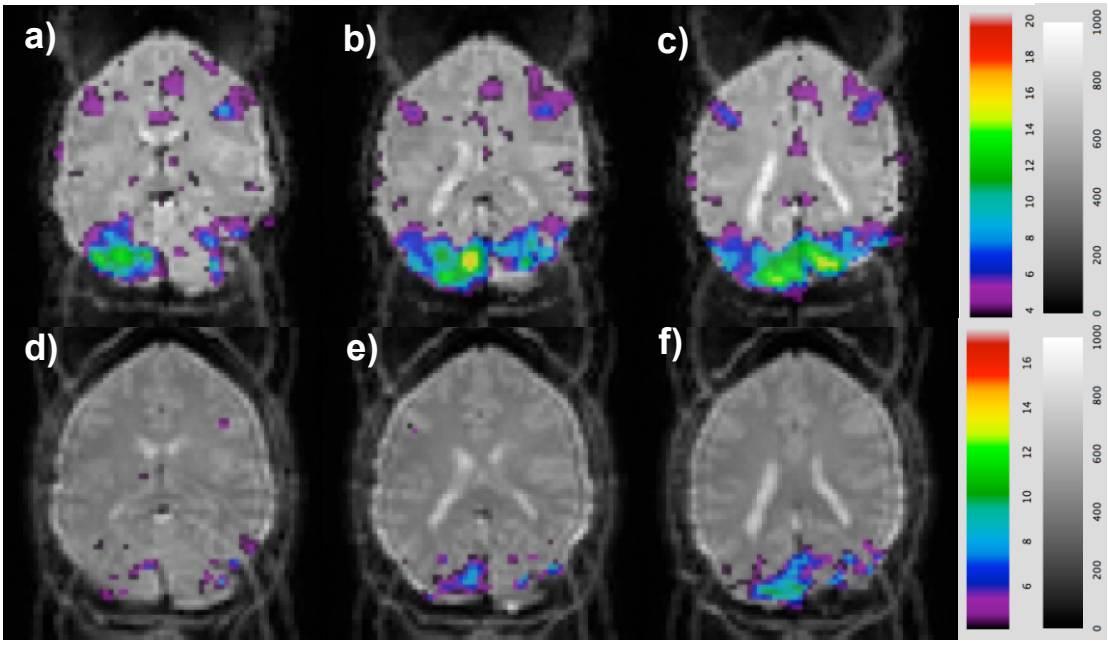

Figure 20: Examples of the images acquired using GRESE-EPI for Subject 2 during a pilot fMRI scan involving a visual stimulus. The overlaid activation maps were corrected for FDR with a threshold of 0.001. 3 contiguous slices retrieved from the center of one image volume are shown here for GRE data (a, b, c) and SE data (d, e, f). The color bars indicate the t-score values and the greyscale bar indicates the signal intensity of the underlying images.

A cursory examination of the activation maps reveals that the results are in accordance with the theoretical underpinnings of BOLD contrast generation in GRE and SE imaging. While no quantitative analysis was performed at this point to examine the magnitude of BOLD signal change, it is possible to see that the spatial extent of the region of activation in GRE data is greater than in the corresponding SE datasets. This may be a reflection of GRE-EPI's sensitivity to large draining veins and venous chambers such as sinuses, where static dephasing dominates over the dynamic averaging of the magnetic field by diffusing spins. It is important to keep in mind that these experiments were carried out at B_0 = 3 T and, as such, the intravascular component of the BOLD signal is not negligible and may compromise the spatial specificity of SE BOLD.

Before using this sequence on other subjects in order to further investigate the performance of GRE-EPI and SE-EPI in BOLD fMRI, the slice profiles of the excitation and refocusing pulses used in GRESE-EPI were tested for a possible mismatch. It has been shown that for pulse sequences optimized for SE-EPI, the excitation pulse is often made larger than the refocusing pulse to ensure that the magnetization is perfectly refocused in the sample; the final slice profile is obtained through the multiplication of the slice profiles associated with the excitation and refocusing pulses. The use of mismatched slice profiles has been shown to be problematic for pulse sequences employed in combined GRE and SE imaging. In imaging techniques involving the acquisition of both types of echoes before and after the refocusing pulses during a single TR, the use of excitation and refocusing pulses with unmatched slice profiles can lead to errors in the signal magnitude due to the extraneous modulation of the longitudinal magnetization of spins located outside the targeted slices. (Schmeideskamp *et al*, 2012) While GRESE-EPI does not fall into this category of combined GRE and SE imaging methods, it is worthwhile to explore this topic as both gradient echoes and spin echoes are acquired during the same scan, albeit during different measurement periods.

2.2 Excitation pulse design using the SLR algorithm

2.2.1 Slice profile simulation

To first evaluate the extent of the potential disparity between the expected and actual values of the slice thickness associated with the excitation pulse in GRESE-EPI, its slice profile was simulated by solving the Bloch equation. In this work, a set of MATLAB (Mathworks, Natick, MA, USA) functions developed by Dr. Brian Hargreaves (available at: http://mrsrl.stanford.edu/~brian/bloch/) were used to analytically determine the spatial distribution of the magnetization in the aftermath of selective excitation.

This Bloch equation simulator makes use of the hard pulse approximation, which states that any RF pulse can be broken down into a series of rectangular pulses of infinitesimal width interspersed with periods of free precession. In this manner, excitation can be understood as the sequential application of these Dirac pulses to the spin system in order to the tip the magnetization vector into the transverse plane. This operation can also be understood as a rotation of the magnetization vector around a transverse axis with a given orientation which depends on the flip and phase angles of each Dirac pulse. To simulate the slice profile of the excitation pulse used in GRESE-EPI, whose waveform in the time domain is presented at figure 21, its magnitude and phase data was imported into MATLAB from IDEA's RF pulse library, whereupon they were used to model the pulse as an array of complex quantities.

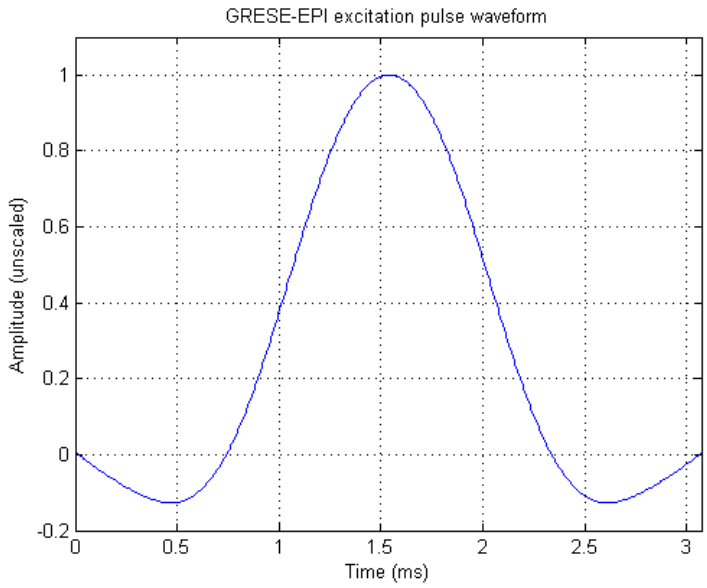

Figure 21: Waveform of the excitation pulse originally used in GRESE-EPI. The pulse was constructed as an array of complex quantities in MATLAB using its magnitude and phase data, imported from IDEA's RF pulse library. The amplitude of the pulse was left unscaled in this figure.

Before running the simulation, however, it is important to ascertain that the pulse is being played out with the correct flip angle; pulses exported from the RF pulse library in IDEA are generic and can be set to any flip angle within the sequence code or protocol editor. To correct for any irregularities in its value, a scaling factor was introduced into the simulation tool's code and applied to the θ produced by each Dirac pulse in order to play out the entire excitation pulse with its correct flip angle. This scaling factor is obtained by dividing the user-defined flip angle, which is equal to 90° for fMRI experiments involving GRESE-EPI, by the sum of each Dirac pulse's θ, which is equal to the pulse's actual flip angle:

$$Scale = \frac{\theta_{user}}{\sum_{i=1}^{n} \theta_i} \qquad \textbf{(2.2)}$$

The flip angles of each Dirac pulse were calculated using equation 1.15 with τ being set to the step time separating each pulse from the next in the waveform. As the excitation pulse is played out for 3.072 ms in GRESE-EPI and is composed of 512 points, the step time was found to be equal to 6 µs.

Other inputs required by the simulator included the T1 and T2 values of the tissue of interest in the scan, which are equal to 1820 ms and 99 ms for gray matter for B_0 = 3 T, (Stanisz *et al*, 2005), as well as information on the gradient lobe used for selective excitation. While oblique slices are used in this work to cover specific anatomical regions of the cerebral cortex during a functional scan, which requires the combined use of multiple magnetic field gradients with different orientations, the slice-selection gradient was modelled as a rectangular gradient lobe with an amplitude of 6.667 mT/m played out along the z-axis to simplify this analysis. This value of the gradient strength was obtained through IDEA's sequence simulator when GRESE-EPI was simulated for axial slices featuring a thickness of 3 mm using the scan protocol outlined in table 1.

The pulse profile's width was investigated over a length of 6 mm; an array of positions spanning -3 mm to 3 mm with steps of 0.01 mm was created for this purpose and the result of the simulation is presented at figure 22.

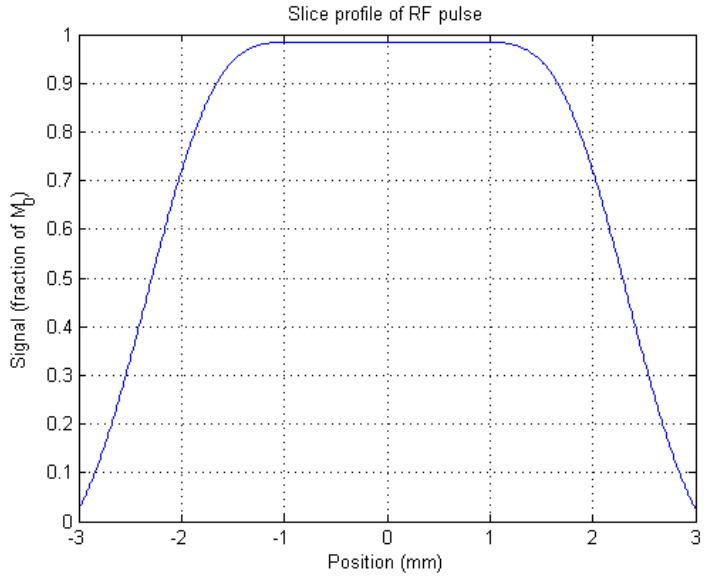

Figure 22: Slice profile of the excitation pulse used in GRESE-EPI obtained using the Bloch equation simulator developed by Dr. Brian Hargreaves.

The slice thickness is defined as the FWHM of the slice profile. For the profile illustrated in figure 22, this parameter is approximately equal to 4.6 mm, which is 53.33% larger than the expected slice thickness of 3 mm. To combat the effects of this newly-discovered discrepancy

between the expected and actual values of this parameter, it was decided that a new excitation pulse with a sharper profile would be created for combined GRE and SE imaging using GRESE-EPI.

2.2.2 Creation of the RF pulse using the SLR algorithm

To design a new excitation pulse for use in GRESE-EPI, MATPULSE, a MATLAB program that allows for the creation of RF pulses using the SLR algorithm, was employed. (Matson, 1994) MATPULSE makes use of GUIs to allow the user to create an RF pulse for a specific application (e.g. excitation, refocusing, etc.) with a set of desired parameters.

As stated in section 1.2.3, FIR filter design methods are employed to generate the polynomials required for SLR pulse generation. MATPULSE gives the user the choice between two such methods: the Parks-McClellan algorithm and the least-squares method. The Parks-McClellan algorithm provides a solution to the filter design problem by minimizing the maximum error between the ideal filter shape and the pulse's frequency response. (Agilent Technologies, 2000) This filter design method is also called the equiripple method due to the fact that the amplitudes of the ripples in the passband and rejection band of the pulse's frequency response are held constant throughout these regions. Pulses created using this FIR filter design method can also present large fluctuations in the value of B_1 at their extremities known as "Conolly wings" which are responsible for the narrow transition band of the frequency responses of the corresponding RF pulses. (Pauly *et al*, 1991)

The least-squared filter design method generates a polynomial by minimizing the weighted squared error between the ideal and approximate frequency responses. (Agilent Technologies, 2000) Pulses created using this algorithm present an improved performance in terms of ripple amplitude in the rejection band when compared to similar pulses generated using the Parks-McClellan algorithm. (Henry, 2000) The amplitude of these ripples will progressively decrease as one moves towards regions distal to the foot of the slice's transition band. This is particularly helpful when trying to minimize cross-talk between adjacent slices in the imaging slab. This advantage, however, comes at the expense of a widened transition band. (Henry, 2000)

The values of parameters such as pulse duration, bandwidth and ripple amplitudes used to create the excitation pulse were selected according to particular design criteria while respecting key physical constraints imposed by the scanner's hardware. One particular criterion used in RF pulse design is the time-bandwidth product $T\Delta f$, a dimensionless variable indicative of the pulse's selectivity. (Bernstein *et al*, 2004) The sharpness of the slice profile is directly proportional to this parameter and values equal or superior to 10 are recommended for the creation of RF pulses using MATPULSE. However, limitations imposed on the pulse's duration and bandwidth hamper the creation of pulses with elevated values of $T\Delta f$. While RF pulses with long durations offer sharper slice profiles (Zhao *et al*, 2005), it is preferable to minimize the length of the excitation period if the pulse is to be used in fMRI. Not only will this permit the use of shorter TEs, but it also becomes possible to ignore the effects of relaxation if the duration of the excitation pulse is shorter by several orders of magnitude than the relaxation times of the tissues of interest. (de Graaf *et al*, 2013) Durations inferior to 5 ms are generally recommended for this purpose. (Bernstein *et al*, 2004; Kim *et al*, 2013)

Sharp slice profiles can also be obtained by increasing the pulse's bandwidth. However, an increase in this value is accompanied by an increase of the pulse's peak B_1 value if its duration is fixed. This parameter is therefore limited by the maximum amplitude of B_1 that can be delivered using the scanner's transmission coil. The body transmit coil of a Siemens Magnetom Trio 3T MRI scanner was used for all experiments conducted in this work and is capable of delivering a value of B_{1Max} of 23.4 μT. (Andronesi *et al*, 2010)

The width W of a slice profile's transition band is calculated using the following design equation:

$$T\Delta f W = D_\infty \quad \textbf{(2.3)}$$

D_∞ is an empirically-derived measure whose value depends on the amplitude of the ripples in the passband and the rejection band. (Pauly *et al*, 1991) In MATPULSE, the user is free to select the values of the ripple amplitudes, expressed as percentages, once $T\Delta f$ has been set, allowing W to be calculated automatically. However, it is not possible to optimize these three parameters simultaneously, forcing a trade-off between the amount of ripple in the pulse's frequency response and its width. (Henry, 2000)

Putting all these factors into consideration, an excitation pulse was created using the least-squares FIR filter design algorithm with a duration of 4.004 ms, a bandwidth of 2.8 kHz ($T\Delta f$ = 11.21) and passband and rejection band amplitudes of 3% and 5.5%, respectively. The pulse's shape in the time domain is presented on figure 23.

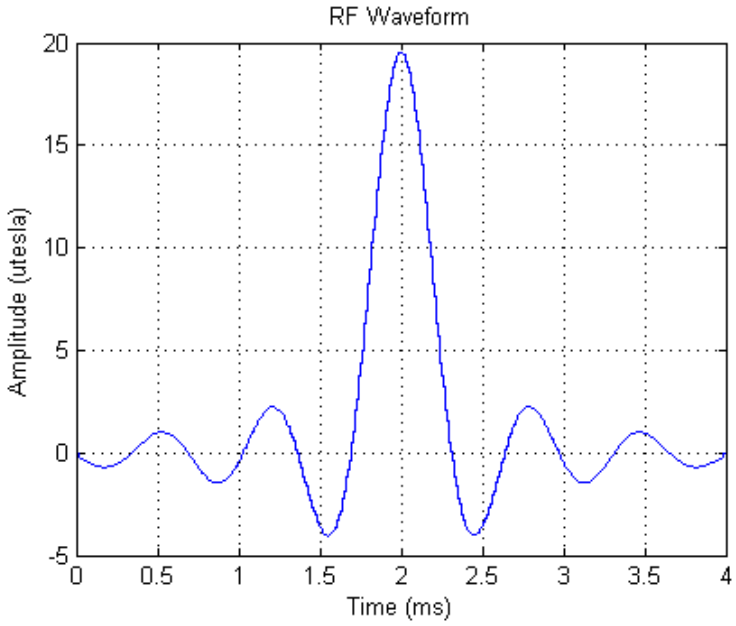

Figure 23: Waveform of the excitation pulse created using MATPULSE.

The pulse's peak amplitude is 19.52 μT, which respects the design criterion imposed by the scanner's physical limitations. Using supplementary functions available in MATPULSE, the amplitude of the waveform was rescaled to ensure that its flip angle would be equal to 90°, bringing its value of B_{1Max} up to approximately 20 μT.

MATPULSE is also equipped with its own Bloch equation simulator in order to visualize an RF pulse's slice profile as it arises during a scan. To do so, the simulator requires both the pulse's B_1 values and the value of G_z used during selective excitation assuming that the slice is acquired with a transverse, coronal or sagittal orientation. To obtain the value of G_z computed at runtime for GRESE-EPI using the experimental protocol outlined in section 2.1.2, the sequence was simulated using POET after replacing the stock excitation pulse with the SLR pulse and simulating the scan protocol shown in table 1 for the acquisition of transverse slices. The amplitude of the slice-selection gradient was found to be equal to 21.9422 mT/m. The effects of

relaxation were not taken into consideration for this simulation and the resulting slice profile is presented at figure 24.

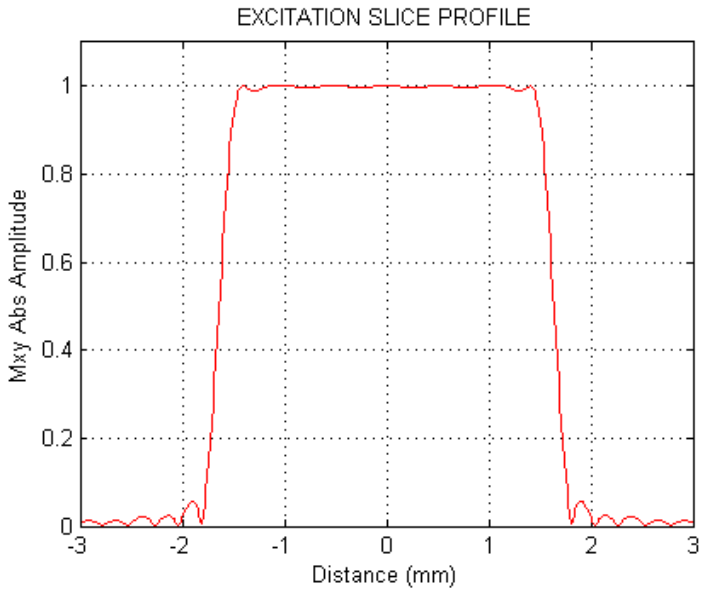

Figure 24: Slice profile of the excitation pulse created using MATPULSE. This profile was obtained by using the Bloch equation simulator available in MATPULSE.

The slice profile of this newly-created pulse was also simulated using the Bloch equation simulator presented in the previous section and is presented in figure 25. The relaxation times were the same as in the previous simulation and the slice-selection gradient was once again modelled as a rectangle function. As the SLR pulse is made up of 512 points and was played out for 4 ms in the pulse sequence, the step time used for this simulation was equal to 7.8125 µs. The FWHM for each of these slice profiles is situated at around 3.28 mm, which is an improvement over the excitation pulse originally used in GRESE-EPI and offers a mismatch of 9.3% between the expected and actual values of the slice thickness.

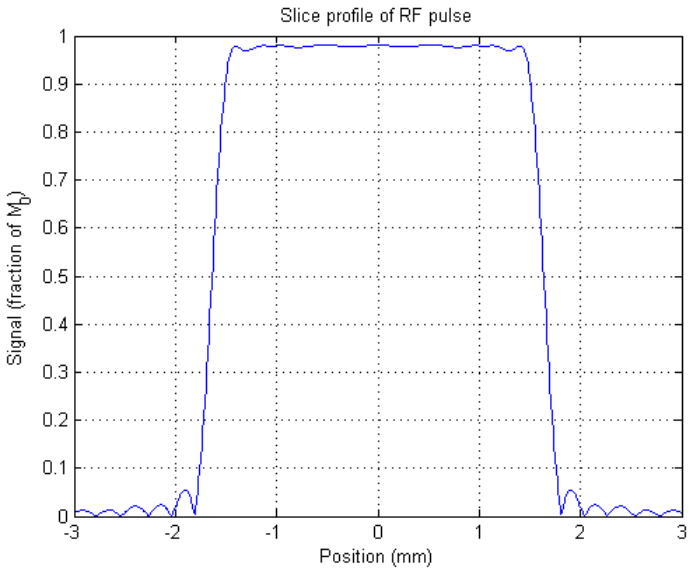

Figure 25: Slice profile of the excitation pulse created using MATPULSE. This slice profile was obtained by using the Bloch equation simulator developed by Dr. Brian Hargreaves.

2.2.3 Slice thickness measurements

The Bloch equation simulations presented in the previous sections unfortunately do not take into account imperfections that may arise during an actual scan session, such as gradient hysteresis, eddy current generation or even B_0 and B_1 inhomogeneity. To verify that the slice thickness derived from the simulated profiles was correct, a direct measurement of this parameter was made. One way to measure the slice thickness is to use a phantom harbouring either a ramp or wedge made of a material whose MR signal-producing qualities differ from the medium in which they are immersed in, e.g. plastic ramps or wedges placed in a container of doped water. (Lerski, 1989) A projection image of this inclined surface is acquired and the slice profile can be obtained by tracing its line profile in the case of a ramp or by differentiating its edge response function in the case of a wedge. (McRobbie *et al*, 2002)

For this work, a streamlined version of this so-called "wedge method" which makes use of the ACR MRI Accreditation phantom (J.M. Specialty Parts, San Diego, CA, USA), pictured at figure 26, was employed. (Papp, 2014; American College of Radiology, 2015)

Figure 26: Picture of the ACR phantom used in this thesis to obtain measurements of the width of the slice profiles destined for use in GRESE-EPI.

This phantom contains a pair of "hot" ramps, i.e. slits carved into plastic blocks filled with an aqueous signal-producing solution (< 12.18 mM $NiCl_2 \cdot 6H_2O$; 76 mM NaCl), that are inclined with an angle of 5.71° with respect to a horizontal slice passing through the slits found at the center of the yellow box shown in figure 27. (American College of Radiology, 2015) Using a pulse sequence harbouring the RF pulse whose profile width is to be investigated, a single slice is acquired at this position, resulting in the production of an axial image of the phantom on which two bright zones can be seen on the dark zone representing the plastic block the ramps are carved into at the center of the image.

To measure the length of each of these bright zones, as seen on figure 28, the upper limit of the image viewer's window must be adjusted to half of the average value of the signal intensity detected on the ramps. To obtain the average signal intensity in both ramps, ROIs were manually drawn on the center of these regions. The slice thickness is then calculated using the following formula, where *a* and *b* represent the length of each ramp seen in figure 28:

$$\frac{a*b}{5(a+b)} \qquad \textbf{(2.4)}$$

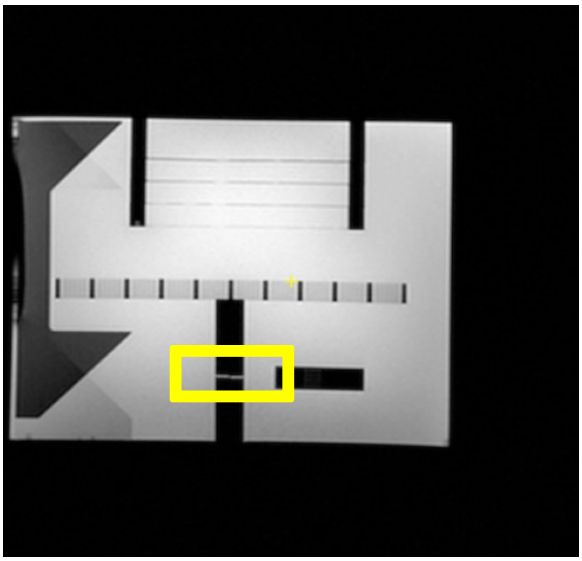

Figure 27: Sagittal view of the ACR phantom. In order to perform a measurement of the slice thickness, the slice must be placed at the center of the yellow box shown above in order to produce an image of the signal-producing portion of the crossed ramps.

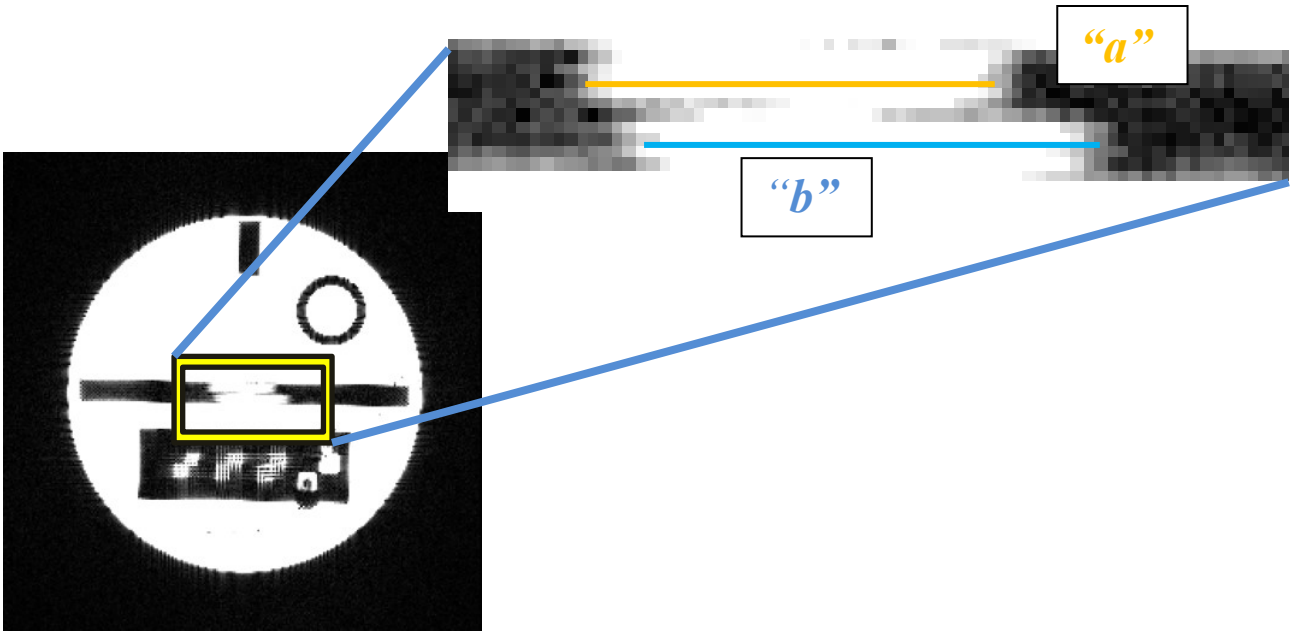

Figure 28: Close-up of the signal-producing portion of the crossed ramps, as viewed during an experiment seeking to evaluate the slice thickness. The lengths of ramps "a" and "b" are represented by the orange and blue bars in the zoomed-in picture of the ramps.

To measure the slice thickness associated with the SLR excitation pulse, a MiniFLASH sequence provided by Siemens Healthcare was used and the enclosed excitation pulse was replaced by the SLR excitation pulse created in section 2.2.2. The MiniFLASH sequence is a

GRE imaging technique similar to the one presented in the pulse sequence diagram in section 1.2.7, but also includes spoiler and rewinder gradients applied along the slice-selection and phase-encoding axes after frequency encoding ends to prevent the apparition of banding artifacts on the image. (Bernstein *et al*, 2004)

This empirical method of measuring the slice thickness was also used to evaluate the thickness of the refocusing pulse employed in GRESE-EPI. To do so, the MiniFLASH sequence was converted into a SE-type sequence ("MiniSE"). To convert the MiniFLASH sequence into an SE imaging technique, the refocusing pulse used in GRESE-EPI was first imported into the sequence code and a slice-selection gradient was designed using the same parameters as those used in the EPI sequence. The timing of the elements needed for the spatial encoding and digitization of MR signals was then altered to accommodate the insertion of the elements needed for the refocusing of the magnetization at TE/2. Similarly to GRESE-EPI, the energy calculation formula was updated to reflect the insertion of the new RF pulse within the sequence and the polarity of certain gradients in the sequence was flipped to account for the phase reversal brought on by the refocusing pulse.

Also added to the MiniSE sequence were two crusher gradients placed on each side of the slice-selection gradient associated with the refocusing pulse in a manner similar to what is used for GRESE-EPI. This was done to apply phase dispersion to spins within a voxel in order to prevent the contamination of the spin echo signal with stimulated echoes that may arise from imperfect refocusing, i.e. when $\theta_{refoc} \neq 180°$. A phase dispersion of 4π is considered sufficient for this purpose and the crusher gradients were played out along the slice-selection axis due to the dimensions of the slice being greater along this direction than in the image plane. (Bernstein *et al*, 2004) The gradient moment needed to meet this design criterion is given by:

$$A_{crush} = \frac{4\pi}{2\pi * \gamma * \Delta z} \quad \textbf{(2.5)}$$

For a slice thickness of 3 mm, A_{crush} is equal to 15.658 mT/(s/m). Using a gradient amplitude of 22 mT/m and a slew rate of 157.1429 mT/m/ms, two trapezoidal gradient lobes were created using the following ramp and flat-top times:

$$t_{Ramp} = G_{crush}/SlewRate = \frac{22\ \text{mT}}{157.1429\ \text{mT/s/ms}} = 0.14\ \text{ms} \quad \textbf{(2.6a)}$$

$$t_{flattop} = A_{crush}/G_{crush} - t_{ramp} = 0.572 \text{ ms (rounded up to 580 µs)} \quad \textbf{(2.6b)}$$

Furthermore, the timing of the gradient lobe used for phase encoding was changed so that it was applied following the application of the refocusing pulse, at the end of the right-hand crusher gradient. This will result in any stimulated echoes generated by imperfect refocusing to undergo spatial encoding in both directions of k-space instead of only being frequency-encoded every TR. When the latter situation occurs, a bright streak oriented in the readout direction may appear on the image and cloud any structure it passes over. (Brown *et al*, 2014) This phenomenon is also known as an FID artifact.

The parameters used to acquire the slices are presented in table 2. These acquisitions were performed on a Siemens Magnetom Trio 3T MRI scanner at the McConnell Brain Imaging Center at the Montreal Neurological Institute. A 12-channel head coil was used as the receiver element for these scans. The resulting images are shown in figure 29.

Table 2: Table of the scan parameters used for the MiniFLASH and MiniSE pulse sequences used in experiments seeking to measure the slice thickness associated with the excitation and the refocusing pulses used in GRESE-EPI.

Parameters	***Values***
TE	20 ms
TR	4000 ms
Receiver bandwidth	260 Hz/pixel
Flip angle	90°
Matrix size	256 x 256
Field of view	256 mm x 256 mm
Slice thickness	3 mm

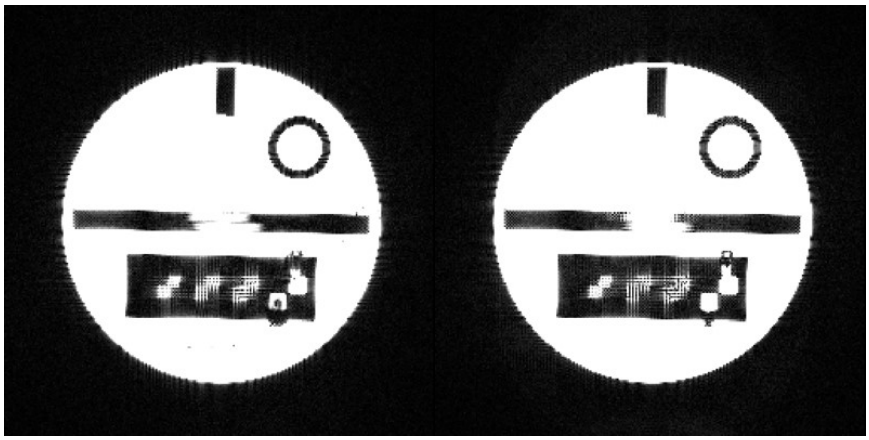

Figure 29: Axial slices of the ACR phantom acquired using the MiniFLASH (left) and MiniSE (right) sequences with the SLR pulse as the excitation pulse.

This experiment was then repeated using the excitation pulse originally used in GRESE-EPI in order to obtain a direct measurement of its thickness. The same parameters as those used for the previous test involving the use of the SLR pulse were employed and slices were acquired using both the MiniFLASH and MiniSE sequences. The results are presented in figure 30.

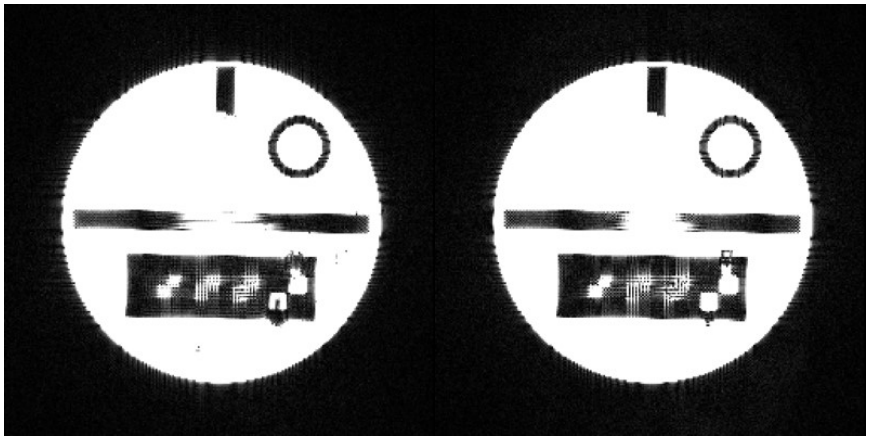

Figure 30: Axial slices of the ACR phantom acquired using the MiniFLASH (left) and MiniSE (right) sequences harbouring the original excitation pulse used in GRESE-EPI.

Due to the in-plane resolution being 1 mm x 1 mm, it is possible to directly measure the lengths of *a* and *b* on the image. As it can be difficult to properly determine the ends of the ramps due to their appearing darker or fragmented on the final image, it is recommended to use the average position of the ramp's end points to calculate the slice thickness. (American College

of Radiology, 2015) The estimated values of the slice thickness associated with the SLR pulse, the excitation pulse used originally used in GRESE-EPI and the refocusing pulse used in conjunction with both excitation pulses are compiled in table 3.

The results of this test indicate that the directly measured values of the slice thickness deviate considerably from those calculated using Bloch equation simulations. Additionally, a mismatch is observed for both pairings of the excitation pulses with the refocusing pulse, with the stock excitation pulse and the SLR pulse being approximately 43% and 9% larger than the refocusing pulse. Various criteria have been proposed to determine the accuracy of the slice thickness using the ACR phantom. The guidelines set forth by the American College of Radiology state that for a slice with an expected thickness of 5 mm, a measured value of 5 ± 0.7 mm is considered acceptable. (American College of Radiology, 2015) Another evaluation criterion, proposed by the American Association of Physicists in Medicine, states that the thickness of a slice is accurate if it falls within 10% of its expected value for slices equal to or larger than 5 mm when using this test. (Jackson, 2010)

Table 3: Table of the values of the slice thickness calculated using each pairing of excitation and refocusing pulses using the ACR phantom method.

RF pulse	***Length of ramp "a"***	***Length of ramp "b"***	***Slice thickness***
SLR excitation pulse	34 mm	38 mm	3.589 mm
Refocusing pulse *(used in tandem w/ SLR pulse)*	31 mm	35 mm	3.288 mm
GRESE-EPI excitation pulse	46 mm	58 mm	5.131 mm
Refocusing pulse *(used in tandem w/ GRESE-EPI pulse)*	32 mm	41 mm	3.5955 mm

While neither value of the slice thickness associated with the excitation pulses tested herein can be considered accurate using the criteria put forth by the AAPM, despite the slice thickness evaluated being thinner than the slices used in quality control tests, the excitation pulse created using MATPULSE is an improvement over the stock excitation pulse due to the smaller mismatch between slice thicknesses when paired with GRESE-EPI's refocusing pulse. This made it a good choice for the BOLD fMRI experiments presented later in this work. It is also possible to notice that the slice thickness of the refocusing pulse changes depending on the width of the slice profile associated with the excitation pulse. This can be ascribed to the previously-discussed fact that the actual slice profile in a SE sequence is the result of a multiplication between the slice profiles of the excitation and refocusing pulses, provided that the FID signals that arise from imperfect refocusing are eliminated using crusher gradients played out both before and after the application of the refocusing pulse. (Schmiedeskamp *et al*, 2012)

2.3 Cerebral venography

As explained in sections 1.3.4 and 1.3.5, a non-negligible amount of BOLD signal is generated within the blood vessels themselves at 3 T and may not be specific to the site of neuronal activation. For this reason, it was necessary to differentiate between the venous vasculature and surrounding parenchymal tissue when attempting to assess the performance of GRE-EPI and SE-EPI in a BOLD fMRI experiment. To do so, susceptibility-weighted imaging (SWI) was employed to acquire high-resolution T2*-weighted images and their corresponding phase images in order to generate cerebral venograms for each participant, the latter of which were used to compartmentalize BOLD signals according to the tissue type of the voxels they originate from. This classification of signals will be touched upon further in section 3.1.2.

SWI uses phase data in addition to magnitude images in order to create maps of the location and size of magnetic field perturbers, i.e. elements presenting a different value of magnetic susceptibility from their surroundings. (Haacke *et al*, 2004; Eriksson, 2011) Specifically, shifts in the value of the local magnetic field caused by magnetic field inhomogeneities can be calculated from the phase data and used to improve the contrast generated by the perturbers on the magnitude images. The paramagnetism exhibited by

deoxyhemoglobin makes cerebral venography a particularly interesting application of this technique. In this work, a series of analysis scripts were coded in MATLAB to perform the image processing steps necessary for the creation of venograms for each participant recruited for the BOLD fMRI experiments presented in the next chapter of this thesis.

Before performing any of these operations on the images, the magnitude images were skull-stripped using the brain extraction tool available in FSL (University of Oxford, Oxford, England) and a binary mask of the brain was created using the resulting image. This mask was applied to the phase data in order to remove the noise outside of the target structure.

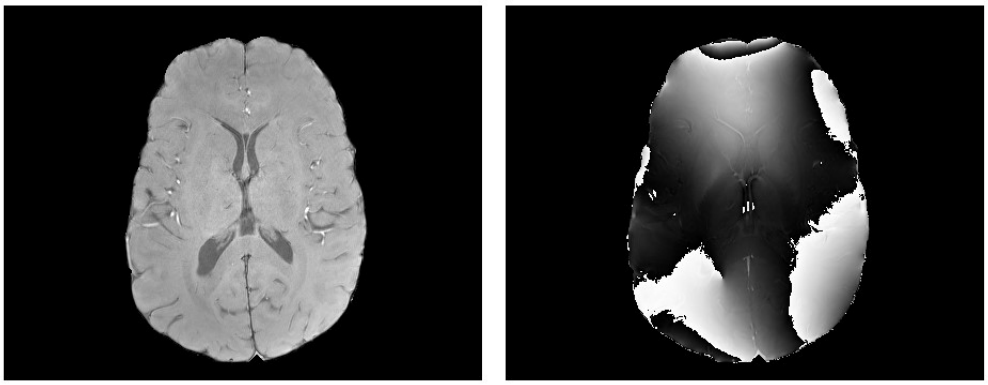

Figure 31: Examples of the magnitude (left) and phase (right) images acquired during SWI. The images presented here were acquired using a TE of 13 ms and the phase image was processed using a binary mask of the brain to remove all noise outside the target structure. Phase wraps are also present in this image, appearing as sudden shifts in the signal intensity between neighbouring pixels. The magnitude image was skull-stripped, as seen above, before generating the binary mask.

The first step in the creation of cerebral venograms is the removal of phase wraps from the data. Caused by large-scale magnetic field inhomogeneity, these artifacts arise on the phase images when the difference between the phase values in two adjacent pixels is greater than 2π. Due to the cyclical nature of this quantity, the values taken on by the pixels in this image are limited to a range of $[-\pi\ \pi]$ despite the fact that the phase at each location may actually exceed these bounds, causing discontinuities to appear when the aforementioned condition is met. (Eriksson, 2011) The removal of these ambiguities is necessary for the generation of venograms as they obscure the microscopic magnetic field variations caused by the presence of perturbers of interest within brain tissue, such as venous vessels. (Li *et al*, 2014)

To eliminate phase wraps from the data, homodyne filtering was implemented in the analysis scripts. (Yang, 2013; Li *et al*, 2014) This operation consists in the application of a low-pass filter to the k-space data of the image set followed by the division of the complex images with their filtered counterparts. A symmetrically-centered 2D Hanning window function was used as the low-pass filter in the analysis scripts (Swanson, 2011):

$$Hann(m,n) = \frac{1}{4}\left(1-\cos\left(\frac{2\pi m}{M}\right)\right)\left(1-\cos\left(\frac{2\pi n}{N}\right)\right) \quad \textbf{(2.7)}$$

Due to the relationship of linear proportionality between the spatial density of the phase wraps and the echo time, the adaptive filter method proposed by (Denk *et al*, 2010) was used instead of a fixed filter width for the multi-echo SWI acquisitions made during the fMRI scans in order to eliminate the phase wraps. In this technique, the dimensions of the low-pass filter are scaled alongside the echo time starting from a reference value of 20% of the dimensions of k-space for TE = 13 ms. The filter size is then increased by the following increment for the next dataset in the series:

$$HannSize = \frac{0.05}{7*TE+0.107} \quad \textbf{(2.8)}$$

Before the filter can be applied to the image data, the phase and magnitude images are combined to produce a complex image. Its Fourier transform is subsequently computed and multiplied with the low-pass filter described by equation 2.7. The inverse Fourier transform of the filtered dataset is then calculated and used to divide the original complex image to complete the homodyne filtering step.

The filtered images were then used to create a phase mask in order to accentuate the contrast produced by the field perturbers by reducing the intensity of pixels corresponding to certain phase values. The mask can be designed to supress either positive or negative phase values, but negative masks are commonly used for cerebral venography. (Eriksson, 2011) In this case, the mask is created by setting pixels for which the phase value is superior to zero to 1 while pixels presenting phase values below zero adopt a value situated between 0 and 1 according to a specified function:

$$M(x,y) = \begin{cases} 0, & \varphi(x,y) < -\pi \\ \frac{(\pi+\varphi(x,y))}{\pi}, & -\pi \leq \varphi(x,y) \leq 0 \\ 1, & \varphi(x,y) > 0 \end{cases} \quad \textbf{(2.9)}$$

Equation 2.9 describes a linear phase mask, but non-linear functions can also be used for the delineation of magnetic susceptibility perturbers in the magnitude image. In this analysis pipeline, a Hanning function was used to create the phase mask:

$$M(x,y) = \begin{cases} 0, & \varphi(x,y) < -\pi \\ \frac{(1+\cos\left(\frac{\pi * \varphi(x,y)}{\pi}\right)}{2}, & -\pi \leq \varphi(x,y) \leq 0 \\ 1, & \varphi(x,y) > 0 \end{cases} \quad \textbf{(2.10)}$$

The use of a non-linear phase mask with a fixed filter width is expected to produce venograms with improved CNR for paramagnetic perturbers compared to venograms generated using a linear phase mask. (Quinn *et al*, 2014) The phase mask is then multiplied with the magnitude image a number of times in order to increase the visibility of the structures of interest. It has been shown that 4 multiplications are necessary to maximize CNR when the linear phase mask is used (Haacke *et al*, 2004) and 11 when the Hanning filter is applied to the images. (Quinn *et al*, 2014) Homodyne filtering and phase mask multiplication is repeated for each set of magnitude and phase images acquired during multi-echo SWI and the results are averaged to produce the subject's final venogram. (Denk *et al*, 2010)

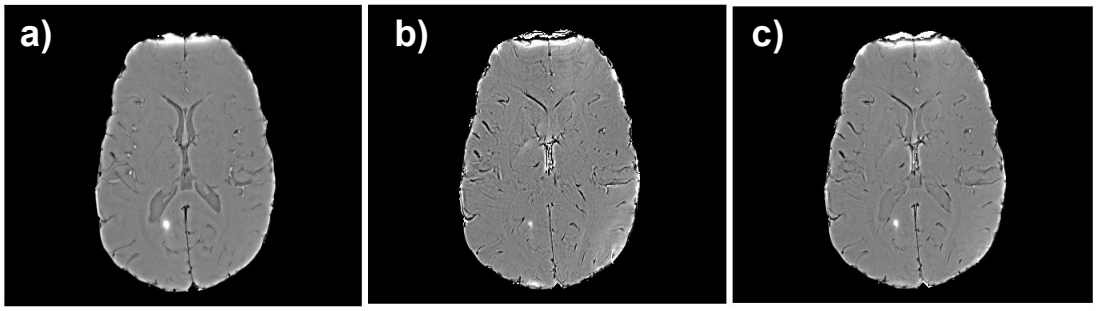

Figure 32: Examples of venograms generated using datasets acquired at TE = 13 ms (a) and TE = 41 ms (b), in addition to the final venogram generated by averaging 5 sets of processed SWI images acquired at different echo times. The venograms shown in this figure were acquired during the scan protocol described in section 3.1.1 for one participant. Images (a) and (b) were used to produce (c). All venograms were generated using a non-linear phase mask function as well as the adaptive filter method.

2.4 Development of a pCASL sequence

In this section, the steps taken to construct an ASL sequence featuring a pseudo-continuous tagging scheme for its application in a CBF quantification experiment presented in the next chapter of this thesis are described. Any ASL sequence can be broken down into three major components: a tagging/control module, the post-label delay and an imaging, or readout, module. To construct the pCASL sequence used in this work, a tagging/control module operating in the unbalanced configuration was developed and inserted into a stock GRE-EPI sequence furnished by Siemens Healthcare. The design of a Q2TIPS saturation mechanism implemented in a PICORE-type PASL sequence was studied for the creation of the pCASL's tagging module due to the shared use of a train of RF pulses applied at specific locations to modulate the longitudinal magnetization of flowing spins in perfusion imaging. Certain key functionalities of this saturation mechanism were retained or reverse-engineered during the development of the final product.

2.4.1 Creation of a tagging unit

The first step in recreating the pseudo-continuous tagging scheme presented in section 1.3.10 was the creation of a tagging unit composed of an RF pulse, a slice-selection gradient and a spoiler gradient. This was done to replicate the events occurring in one peak-to-peak RF pulse cycle within the train of labelling pulses and, by proxy, the conditions necessary for flow-driven inversion on a miniature scale. The design of each one of these three components is not trivial and must meet certain specifications to ensure the proper functioning of the tagging module.

The shape of the tagging unit's RF pulse is one of the crucial factors that must be addressed when designing a pCASL sequence. While the envelope of CASL's inversion pulse is a rectangle function, it is not desirable to divide it into a series of evenly-spaced rectangular pulses when passing to a pseudo-continuous labelling scheme. The use of such pulses results in the formation of aliased labelling planes that will impact the sequence's inversion efficiency. (Dai *et al*, 2008) The nth labelling plane is located at a distance z from the original plane, with z being equal to:

$$z = \frac{n}{(\gamma G_{avg} \Delta t)} \tag{2.11}$$

Where G_{avg} is the value of the slice-selection gradient normally used in CASL and Δt, the duration of a peak-to-peak RF pulse cycle. To avoid the extraneous modulation of the magnetization of arterial spins caused by multiple labelling planes, Hanning function-shaped pulses were designed for use in the tagging unit. Pulses with this shape are recommended for use in pCASL due to the rapid drop-off in their frequency responses compared to rectangular pulses. (Dai *et al*, 2008; Debacker, 2014) The pulse envelope can be described using the following equation:

$$F(t) = \begin{cases} 0.5 + 0.5\cos(2\pi t), & |t| \leq 0.5 \\ 0, & |t| > 0.5 \end{cases} \tag{2.12}$$

The Hanning pulse destined for use in the pCASL sequence was created in MATLAB using 500 values of t, as a pulse with a duration δ of 500 µs was desired; the minimum step time permitted by the scanner's RF amplifier is equal to 1 µs. The pulse's waveform is shown in figure 33.

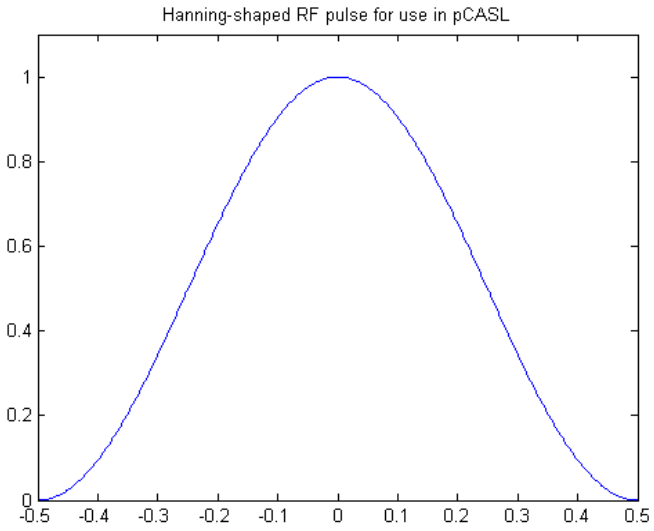

Figure 33: Envelope of a Hanning-shaped tagging pulse designed for use in a pCASL sequence.

It has also been demonstrated that the flip angle of the tagging pulses will have an effect on the sequence's inversion efficiency. Through computer simulations and experiments carried

out *in vivo*, the optimal value for this parameter has been shown to be situated between 20° and 30°. (Wu *et al*, 2007) Consequently, the Hanning pulse was implemented with a flip angle of 25°. The choice of an optimal flip angle also ensures that the average value of B_1 during a peak-to-peak RF pulse cycle is controlled for, as evidenced by the relationship between these two variables expressed in equation 1.15. (Wu *et al*, 2007; Dai *et al*, 2008)

However, the modifications made to the tagging pulse's shape are not sufficient to fully suppress the aliased labelling planes. A strong slice-selection gradient must be used to narrow the pulse's slice profile and reduce the effect of the aliased labelling planes on flowing blood water spins. A gradient strength of 10 mT/m is recommended for this purpose (Alsop *et al*, 2015), but any value can be chosen as long as the following criterion is fulfilled:

$$\frac{G_{slice}}{G_{avg}} \gg \frac{\Delta t}{\delta} \tag{2.13}$$

As G_{avg} is habitually valued at 1 mT/m in CASL, the following parameters were used to design the tagging unit:

- G_{slice}: 9 mT/m
- Δt: 1500 µs
- δ: 500 µs
- Ramp times for G_{slice} and G_{spoil}: 100 µs for both the ramp-up and ramp-down times.
- Flat-top times for G_{slice} and G_{spoil}: 500 µs

Because the sum of the durations of G_{slice} and G_{spoil} is equal to 1400 µs, a delay was added to the end of the tagging unit to achieve the desired Δt of 1500 µs.

The values selected for G_{slice} and Δt fulfill the criterion expressed in equation 2.13 as the ratio of gradient amplitudes is 3 times larger than the ratio of the duration of a peak-to-peak RF pulse cycle to the duration of a single pulse ($9 \gg 3$). Additionally, these values have been selected for the design of pCASL sequences that have successfully been implemented and employed in *in vivo* perfusion imaging experiments. (Dai *et al*, 2008)

To determine the value of G_{spoil} necessary to achieve a G_{avg} of 1 mT/m, the method used in (Debacker, 2014) was employed. Put simply, the tagging unit was broken down into a series of

geometrical shapes and an equation with one unknown was posed to determine the area underneath the spoiler gradient's lobe. This breakdown of the tagging unit into smaller pieces is illustrated on figure 34 and the corresponding equations for the area of each shape are formulated below.

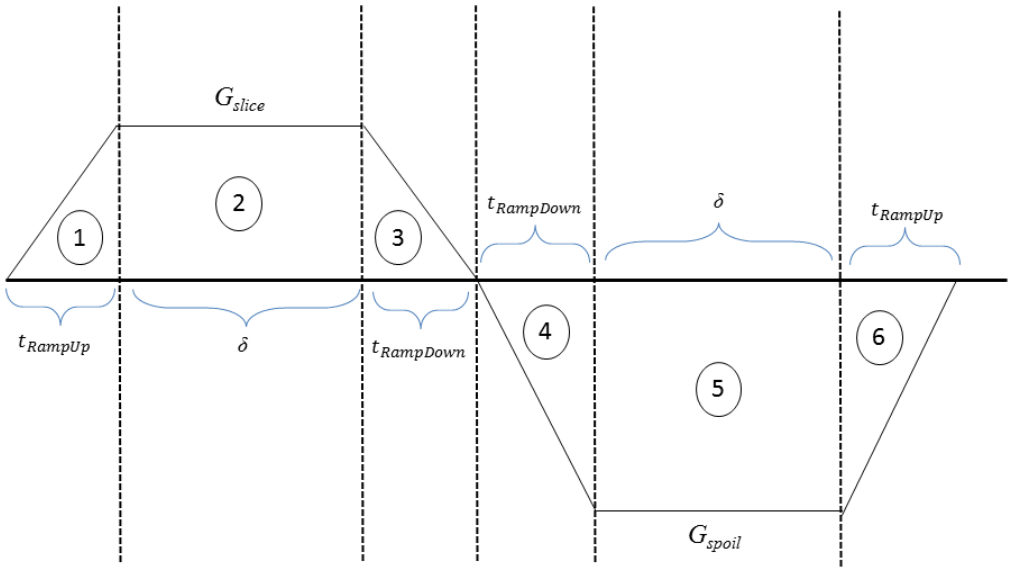

Figure 34: Decomposition of the tagging unit's gradient lobes into a series of geometric shapes in order to determine the value of G_{spoil} that will result in the application of the correct value of G_{avg} at runtime.

$$G_{avg} = \frac{A_1+A_2+A_3+A_4+A_5+A_6}{\Delta t} \quad \textbf{(2.14a)}$$

$$A_1 = A_3 = \left(\frac{t_{RampUp} * G_{slice}}{2}\right) \quad \textbf{(2.14b)}$$

$$A_4 = A_6 = \left(\frac{t_{RampDown} * G_{spoil}}{2}\right) \quad \textbf{(2.14c)}$$

$$A_2 = (G_{slice} * \delta) \quad \textbf{(2.14d)}$$

$$A_5 = \left(G_{spoil} * \delta\right) \quad \textbf{(2.14e)}$$

$$G_{avg} * \Delta t = 2\left(\frac{t_{RampUp} * G_{slice}}{2}\right) + 2\left(\frac{t_{RampDown} * G_{spoil}}{2}\right) + (G_{slice} * \delta) + \left(G_{spoil} * \delta\right) \quad \textbf{(2.14f)}$$

By replacing each variable in equation 2.14f by its corresponding parameter value, a solution was found for G_{spoil}:

$$G_{spoil} = -6.5\ \mathrm{mT/m}$$

2.4.2 Sequential application of multiple tagging units

The second step taken to implement the pseudo-continuous tagging mechanism was the chaining of multiple tagging units in order to create a train of labelling pulses with a duration equal to that of a typical inversion pulse used in CASL. An iterative loop was created for this purpose along with the functions necessary for phase cycling, switching between labelling and control conditions and playing out each tagging unit with the correct value of Δt.

The number of iterations to be performed by the loop, i.e. the number of tagging units to be played out during the labelling and control experiments, can be obtained by dividing the duration of the tagging period by Δt. As specified in sub-section 1.3.10, phase cycling is necessary to ensure that arterial spins are inverted adiabatically; the phase of each pulse must be adjusted to offset the phase accumulated by flowing spins due to the imbalance between the moments of G_{slice} and G_{spoil}. (Jahanian *et al*, 2011) The phase increment is a function of multiple variables, such as the strength of G_{avg}, Δt and the distance between the labelling plane and the isocenter of the scanner's magnet, Δz:

$$\Delta\varphi = G_{avg} * \Delta t * \gamma * \Delta z \qquad \textbf{(2.15)}$$

In this sequence, the phase of each Hanning pulse is reset to zero before playing out its corresponding tagging unit. To circumvent this pitfall, $\Delta\varphi$ was multiplied by N, the current tagging unit's position in the chain, to ensure that the correct phase increment was added to each pulse. In this case, the first value taken on by N is zero.

As this pCASL sequence was implemented in the unbalanced configuration, additional functions were added into the loop to modify the parameters of the spoiler gradient during the control scans. As labelling and control experiments are conducted in an alternating manner in ASL, it is possible to use a repetition counter to evaluate whether the current measurement

period is odd-numbered or even-numbered and assign it a specific task based on this information, as was the case for GRESE-EPI. For this sequence, spin tagging was performed during odd-numbered measurement periods. During an even-numbered measurement period, G_{spoil} was set to -9 mT/m to produce a G_{avg} of 0 mT/m and $\Delta\varphi$ was made to alternate between 0° and 180° to ensure that the average value of B_1 would also be equal to zero for the control condition. The PLD is then played out at the end of the loop, after the last tagging unit in the chain is played out.

2.4.3 Customization of the pCASL sequence

Once the design and implementation of the tagging module was completed, a number of special parameters were defined to give the experimenter additional control over the variables impacting the pCASL sequence's inversion efficiency. Among these were:

- The position of the labelling plane, Δx
- The duration of the tagging process, $(N*\Delta t)$
- The PLD
- G_{avg}
- The labelling pulse's flip angle
- Δt

The first element in this list is particularly important as anatomical variability will require the position of the labelling plane to be adjusted from one individual to the next for perfusion imaging experiments. In the pCASL sequence presented here, the user may input a position for the labelling plane that is defined as the distance which separates it from the center of the imaging slab. To implement this functionality, a function used to apply frequency shifts to pulses destined for off-center excitation in a PICORE Q2TIPS sequence was incorporated into the pCASL sequence's code. The frequency shift is calculated using the following formula:

$$\Delta\omega = \gamma * G_{slice} * \Delta z + 0{,}5 \qquad \textbf{(2.16)}$$

In this equation, the frequency shift is calculated using the distance separating the labelling plane from the magnet's isocenter. To find the correct value of Δz which allows for the

desired position of the labelling plane, the distance separating the imaging slab's center slice from the isocenter, $\Delta z_{CenterSlice}$, first needed to be found. As the slab's slices are arranged in the order they are to be acquired in, it becomes possible to divide the total number of slices by 2 to obtain the index of the center slice so that the sequence can automatically retrieve this slice's position relative to the isocenter. Δz can then be obtained through the following equation:

$$\Delta z = \Delta z_{CenterSlice} - \Delta x \quad \textbf{(2.17)}$$

The additional factor of 0.5 was left in the formula to round up the value of the frequency shift for data type conversion between different variables initialized in the sequence code. Modifications were then made to the GRE-EPI sequence's looping architecture to accommodate the insertion of the pseudo-continuous tagging/control module in each TR. As such, the timing of the elements needed for signal acquisition were reviewed and adjusted accordingly. As was the case for GRESE-EPI and MiniSE, the energy calculation formula was also reviewed to take into account the addition of a given number of tagging pulses per TR and ensure that SAR measurements were conducted properly at the outset of each scan.

Chapter 3. Experimental protocols and data analysis

3.1 Comparative analysis of GRE and SE BOLD

3.1.1 Scan protocol

To compare the performance of GRE-EPI and SE-EPI in the context of a BOLD fMRI experiment involving a sensory stimulus and the use of the updated GRESE-EPI sequence featuring excitation and refocusing pulses whose slice profiles are tentatively matched, the fMRI experiment described in section 2.1.2 was reprised and four healthy adult males between the ages of 20 and 30 years were recruited as participants in this study. Each subject was screened for health issues and compliance with the MRI environment and informed consent was obtained in each case. All scans were performed at the McConnell Brain Imaging Center of the Montreal Neurological Institute on a Siemens Magnetom Trio 3T scanner. A 32-channel head coil was used as the receiver element in each experiment.

Two fMRI scans were performed for each subject in order to study GRE and SE BOLD when the TE of both imaging techniques are optimized and when they are set to the TE used for GRE imaging. The scan protocol presented in table 1 was reused for both experiments and the echo times were set to 75 ms for SE-EPI and 30 ms for GRE-EPI in the optimal TE scan. For the equivalent TE scan, partial Fourier acquisition (k = 7/8) was used to lower the TE for SE-EPI to 30 ms. The number of slices in the image slab was decreased from 30 to 18 due to the restrictions imposed by the long echo time used in optimized SE-EPI. While the simulations of the slice profile were carried out with TE = 99 ms, a shorter TE was used in practice due to the need of achieving good spatial coverage of the regions to be investigated during the fMRI scans. TEs of 75 ms have previously been employed in SE BOLD fMRI for a field strength of 3 T. (Yeh *et al,* 2009) Additionally, the receiver bandwidth was decreased from 2441 Hz/pixel to 2298 Hz/pixel in order to reduce the intensity of the N/2 ghosts, which are prominent on the EPI data presented on figure 20, and to prevent phantom activation from being detected in these regions.

In EPI, the receiver bandwidth is usually set to a value which minimizes the echo spacing in order to reduce the effects of T2 blurring, i.e. the effects of relaxation occurring as k-space is

being filled. (Bernstein *et al*, 2004; Giannelli *et al*, 2010) However, the use of the minimum echo spacing requires the polarity of the readout gradients to be flipped extremely rapidly, which may lead to the generation of eddy currents responsible for the heightened visibility of the Nyquist ghosts. It is therefore preferable, in certain cases, to use a suboptimal echo spacing in order to lessen the impact of these artifacts on the images. (Giannelli *et al*, 2010)

A set of high-resolution T1-weighted anatomical images were also acquired for each subject before the fMRI trials using an MPRAGE sequence to help position the image slab used in GRESE-EPI over each participant's visual cortex. The scan parameters were the same as those used for the pilot fMRI scans described in section 2.1.2, except for subject 1, for whom a field of view of 256 mm x 256 mm was used, along with a matrix size of 256 x 256. The functional images were acquired using an orientation of -30° relative to the AC-PC line.

SWI was also performed on each participant in order to gather the data necessary for the generation of cerebral venograms which would in turn allow for the facilitated discernment of venous vessels in the brain. The parameters used to acquire these datasets were the following: TE (multi-echo scan with 5 TEs) = {13 ms, 20 ms, 27 ms, 34 ms, 41 ms}, TR = 48 ms, flip angle = 17°, field of view = 260 mm x 204 mm, matrix size = 448 x 350, receiver bandwidth = 151 Hz/pixel, GRAPPA factor = 2, slice thickness = 1.3 mm, number of slices = 120, distance factor = 20%. Phase and slice partial Fourier values were set to 6/8.

3.1.2 Data analysis

GLM analysis was performed in order to generate the activation maps using the same procedure outlined in section 2.1.2. Maps of the effect size of the activation, expressed as a percentage of the baseline signal, were also computed at this time for each subject's GRE and SE datasets. To evaluate the BOLD signal change detected using both GRE-EPI and SE-EPI, the effect size was calculated in venous and non-venous structures for the reasons outlined at the beginning of section 2.3. To do so, binary vein masks were created for each participant using their respective venograms. The processed SWI volumes were first thresholded using an upper limit determined by visual inspection in order to set the intensity of all non-venous structures to zero while retaining most of the information concerning the location of the venous structures

within the brain tissue. The thresholded SWI datasets were then downsampled to a resolution of 3 mm x 3 mm x 3 mm using the volume resampling tool available in Neurolens before being binarized. Each participant's percent effect size map was used as the template for the downsampling operation performed on their respective thresholded venograms. These steps are pictured on figure 35.

To quantify the percent effect size arising from the parenchymal tissue, subject-specific functional ROIs, examples of which are shown at figure 36, were created for each participant by selecting voxels found to overlap on the corrected t-maps generated using the GRE and SE images acquired during one experiment to restrict the analysis to a common region of activation. (Bandettini *et al*, 1994) These ROIs were then summed with the participants' respective binary vein masks to produce multi-value vein masks that were subsequently used to retrieve the individual values of the percent effect size in both types of tissue voxels (veins and parenchyma) in the percent effect size maps generated using the GRE and SE datasets within the region of activation common to GRE and SE data. Group averages of the percent effect size in both tissue compartments using both imaging techniques were then computed using the values compiled for each participant.

The same steps were then taken to compute the average t-score in both types of tissue voxels for the activation maps generated using GRE datasets and SE datasets. Two multi-value vein masks were created for each participant using the activation maps generated during the fMRI experiments involving optimal and matched TEs. The data from both these experiments were analyzed separately and all analyses were carried out in native space.

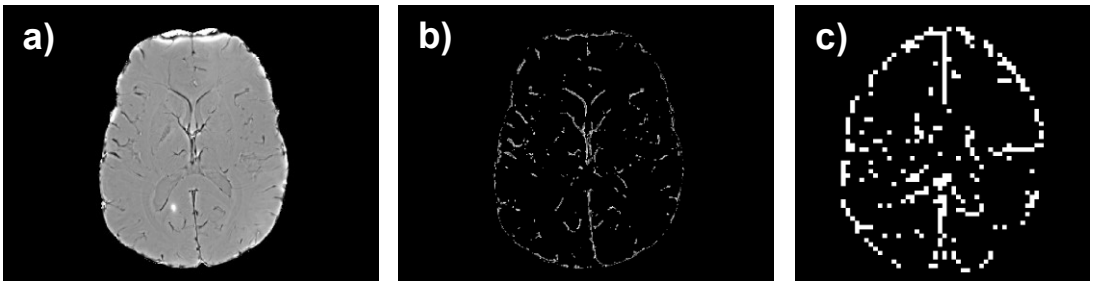

Figure 35: Steps taken to create a binary vein mask by using a subject's venogram, as generated using the steps outlined in section 2.2 using the non-linear phase mask function and the adaptive filter method. The venogram, shown in a) is first thresholded using a value that was determined through visual inspection of the data in order to set the intensity of all non-venous structures to zero. This new image volume, shown in b), is then downsampled to the resolution of the respective subject's EPI data. The maps of the percent effect size for the same participant from which the data was obtained was used as the sampling template for this operation. The final result is shown in c).

Figure 36: Examples of the multi-value vein masks used for the analysis of brain activation. These masks were created for one individual having undergone both fMRI experiments described in section 3.1.1. The voxels belonging to the venous vasculature found within the common region of activation appear as white on the images and the voxels classified as parenchymal tissue appear in light grey. Black and dark grey voxels are either non-venous structures or vessels which are found outside the subject-specific functional ROI; the individual t-scores and percent effect size values detected in the latter regions were not considered during data analysis.

3.2 Comparison of two pCASL sequences

3.2.1 Scan protocol

To assess the performance of the pCASL sequence developed in this work, it was compared to an externally-developed pCASL sequence originally presented in (Wu *et al*, 2007) and whose efficacy in terms of CBF quantification has been thoroughly demonstrated in other studies. (Tancredi *et al,* 2012; Tancredi *et al*, 2015) Three male subjects between the ages of 20 and 30 years were recruited for this experiment. Each subject was screened for health issues and compliance with the MR environment. Informed consent was obtained in each case and all experiments were conducted at the McConnell Brain Imaging Centre of the Montreal Neurological Institute on a Siemens Magnetom Trio 3T MRI scanner. A 32-channel head coil was used as the receiver element for all scans. To ensure an adequate comparison between the two sequences, the scan parameters were matched as closely as possible to those presented in table 4. The values presented therein were selected based on a previous study conducted on a demographic group similar to the one used for this experiment. (Tancredi *et al,* 2015)

Table 4: Table of the scan parameters used to test the pCASL sequence's imaging capabilities in the context of a whole-brain CBF quantification experiment at rest.

Parameters	***Values***
TE	8.4 ms
TR	4120 ms
Receiver bandwidth	3256 Hz/pixel
Matrix size	64 x 64
Field of view	288 mm x 288 mm
Slice thickness	4.5 mm
Number of slices	25
Distance factor	11% of the slice thickness
Measurements	144
Tagging duration	2 s
PLD	0.9 s
GRAPPA factor	2
Partial Fourier factor	7/8
Total scan time	10 minutes

The pCASL scans were preceded by a time-of-flight (TOF) angiography to optimize the position of the labelling plane for each subject. To ensure that the magnetization of blood water spins is properly inverted, the labelling plane must be placed above the bifurcation of the common carotid arteries and perpendicular to the internal carotids and vertebral arteries. Care must also be taken to avoid placing the labelling plane in a region of the neck where flowing spins are liable to pass through it multiple times. This is particularly problematic at the level of the C2 vertebra, where the vertebral arteries curve laterally and vertically to pass through the transverse foramen of C1 before curving posteriorly to run along the superior surface of the atlas to enter the skull. (Cacciola *et al*, 2004) The labelling plane should therefore avoid being placed in a region covering the arching of the vertebral arteries. The parameters used for TOF angiography were the following: TE = 3.85 ms, TR = 22 ms, matrix size = 256 x 232, field of view = 256 mm x 232 mm, number of slices = 81, slice thickness = 1 mm, distance factor = -20.83%, GRAPPA factor = 2, receiver bandwidth = 164 Hz/pixel, flip angle = 18°. The labelling plane was set 100 mm away from the center of the imaging slab for subject 1 and 95 mm away

from the center of the imaging slab for subjects 2 and 3. The slice partial Fourier value was set to 7/8.

A set of high-resolution T1-weighted images were acquired at this time using an MPRAGE sequence to assist with the positioning of the imaging volume for the pCASL scan. The parameters for this sequence were the same as the ones used in the GRESE-EPI experiments for subject 1. (FOV = 240 mm x 256 mm, matrix size = 240 x 256) A field of view of 248 mm x 256 mm was used for subjects 2 and 3, along with a matrix size of 248 x 256. 176 slices were acquired during subject 1's anatomical scan, as opposed to 192 slices for subjects 2 and 3. The pCASL images were acquired using a transverse orientation for both the in-house and externally-developed sequences.

3.2.2 Data analysis

Maps of CBF were computed using the ASL quantification tools included in the Neurolens software package. To compute CBF in each voxel, the equation used in (Wang *et al*, 2003) was used:

$$\Delta M = \frac{2M_0(CBF)\alpha}{\lambda/(T1_{blood})}\left(e^{-\left(\frac{PLD}{T1_{blood}}\right)} - e^{-\left(\frac{\tau_{tag}+PLD}{T1_{blood}}\right)}\right) \quad \textbf{(3.1)}$$

M_0 represents the equilibrium magnetization in the brain, τ_{tag}, the duration of the labelling period and λ, the blood/tissue water partition coefficient. The value selected for the latter parameter was 0.9 and the T1 of blood was set to 1.49 s. The sequence's inversion efficiency is designated by the variable α in equation 3.1 and was set to 0.94, which was previously determined in the literature through Bloch equation simulations. (Pohmann *et al*, 2010)

As per the theory of CBF quantification, ΔM was obtained by pairwise subtraction of image volumes (even minus odd) to remove the signal produced by static tissues in both the tagging and control conditions. An estimate of M_0 was obtained using pairwise addition of the even and odd measurements. The effect size of these volumes was calculated to obtain the final values of ΔM and M_0. The estimation of CBF in different compartments of the brain was

accomplished using a set of analysis scripts developed by Dr. Clément Debacker that made use of functions available in Neurolens.

To generate masks for the different parts of the brain targeted in this experiment, the BET and FAST tools available in FSL were used for skull-stripping and segmentation of the T1-weighted anatomical images. Masks of the gray matter and the white matter were created in addition to a mixel-type mask that was used to estimate whole-brain CBF. Each mask was resampled to the resolution of the pCASL data sets for quantitative analysis of the CBF maps.

The pCASL datasets were subjected to preprocessing before CBF quantification and functions available in Neurolens were called upon for intensity normalization, motion correction and spatial filtering of the image volumes. A Gaussian kernel with a FWHM of 6 mm was employed for the latter step. Individual mean values of CBF in each part of the brain for each participant were obtained using weighted ROI averaging with the previously-described brain tissue masks as inputs. The calculation of the standard deviation for these average values of CBF was done using functions contained in the minctools software package. (Montreal Neurological Institute, Montreal, Quebec, Canada) Group averages of gray matter, white matter and whole-brain CBF were computed by using each subject's resampled brain tissue masks to pool together the values of CBF belonging to each tissue type and computing the average value of the pooled data.

Chapter 4. Results

4.1 Comparative analysis of GRE and SE BOLD

Examples of the images acquired using GRESE-EPI during the fMRI experiments involving optimal and matched TEs are presented on figures 37 and 38 for all four subjects along with the corresponding activation maps, the latter of which were corrected for FDR with a threshold of 0.001.

Examples of the percent effect size maps are presented on figure 39 for the experiment involving optimal TEs and on figure 40 for the experiment involving matched TEs. The images shown on figures 39 and 40 correspond to the slices presented in figures 37 and 38 for both the GRE and SE datasets.

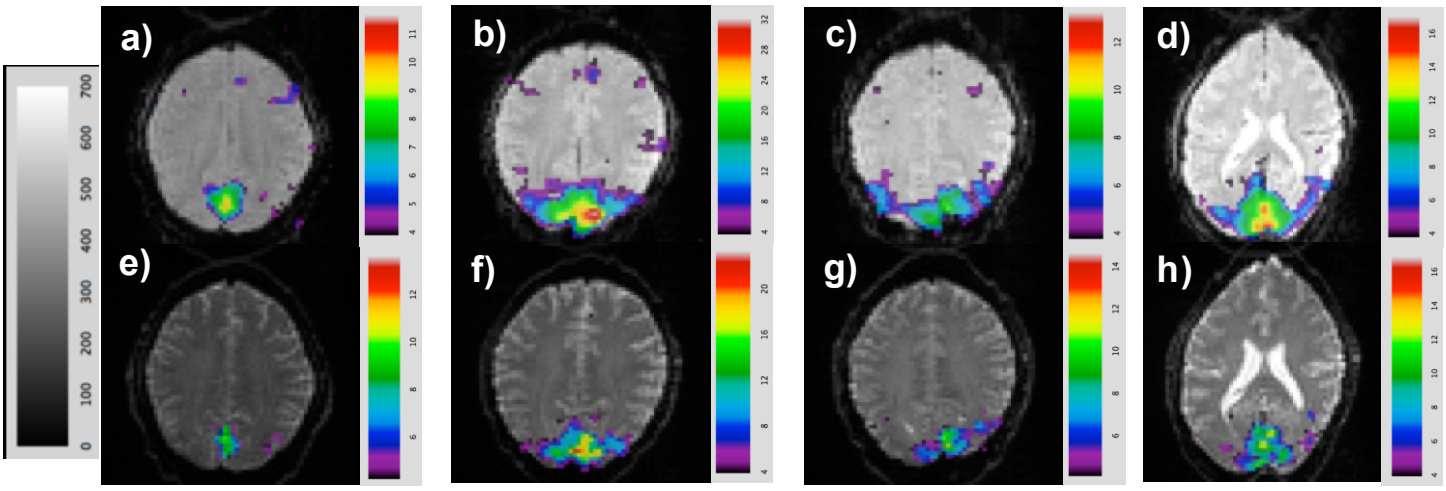

Figure 37: Examples of images acquired using GRESE-EPI during an fMRI experiment involving a visual stimulus using optimized values for GRE-EPI and SE-EPI. (TE_1 = 30 ms, TE_2 = 75 ms) GRE data for subjects 1 (a), 2 (b), 3 (c) and 4 (d) are shown from left to right in the top row. SE data for subjects 1 (e), 2 (f), 3 (g) and 4 (h) are shown from left to right in the bottom row. The color bars indicate the t-score values. The greyscale bar indicates the signal intensity of the brain images. The slices shown for subject 4 do not come from the same position in the imaging slab as those shown for subjects 1, 2 and 3.

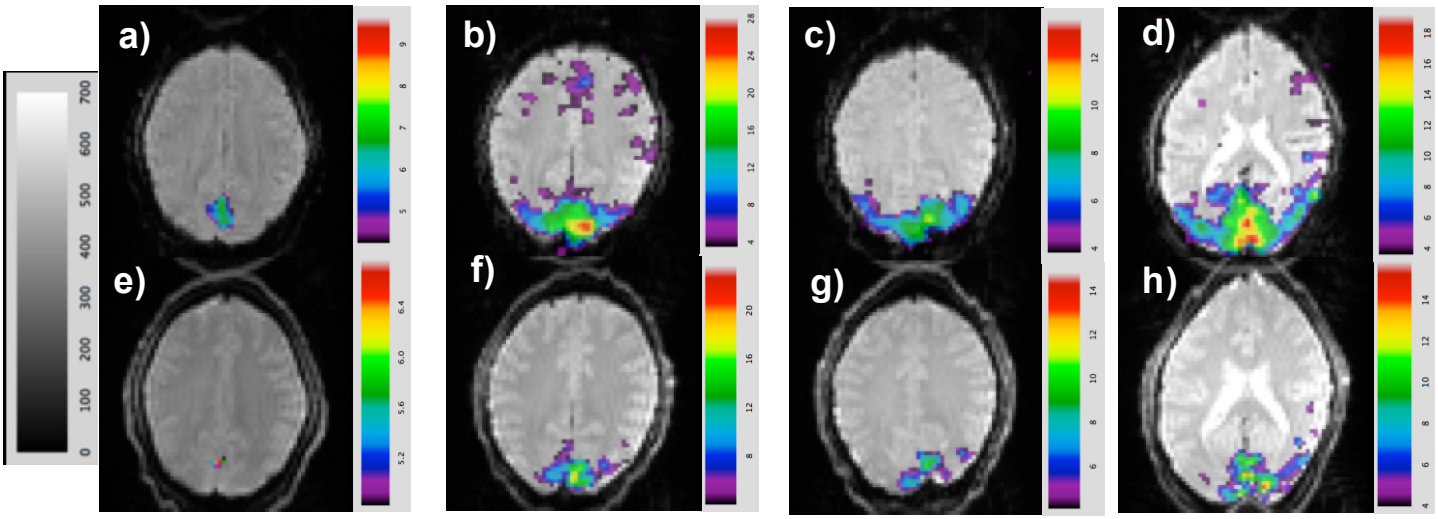

Figure 38: Examples of images acquired using GRESE-EPI during an fMRI experiment involving a visual stimulus using matched values for GRE-EPI and SE-EPI. ($TE_1 = TE_2 = 30$ ms) GRE data for subjects 1 (a), 2 (b), 3 (c) and 4 (d) are shown from left to right in the top row. SE data for subjects 1 (e), 2 (f), 3 (g) and 4 (h) are shown from left to right in the bottom row. The color bars indicate the t-score values. The greyscale bar indicates the signal intensity of the brain images. The slices shown for subject 4 do not come from the same position in the imaging slab as those shown for subjects 1, 2 and 3.

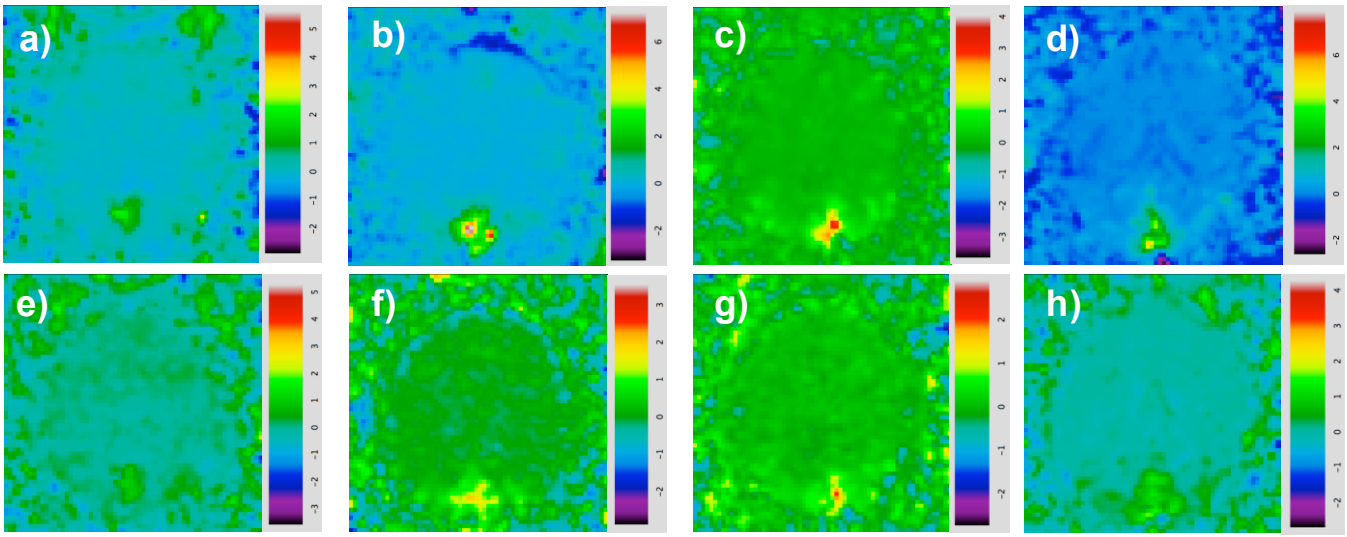

Figure 39: Examples of the percent effect size maps generated using each subject's GRE and SE data acquired using GRESE-EPI during an fMRI experiment involving the use of a visual stimulus using optimized TEs for SE-EPI and GRE-EPI. The percent effect size maps generated using GRE data from subjects 1 (a), 2 (b), 3 (c) and 4 (d) are presented in the top row, from left to right. The percent effect size maps generated using SE data from subjects 1 (e), 2 (f), 3 (g) and 4 (h) are presented in the bottom row, from left to right. The color bars indicate the percent effect size values. The slices shown in this figure correspond to those shown in figure 37.

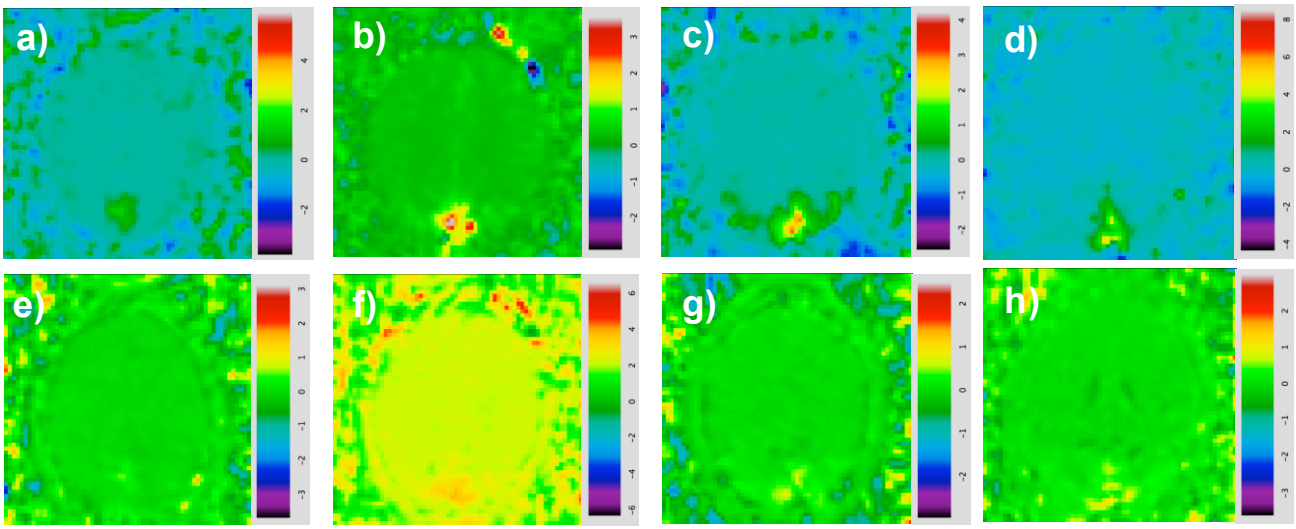

Figure 40: Examples of the percent effect size maps generated using each subject's GRE and SE data acquired using GRESE-EPI during an fMRI experiment involving the use of a visual stimulus using matched TEs for SE-EPI and GRE-EPI. The percent effect size maps generated using GRE data from subjects 1 (a), 2 (b), 3 (c) and 4 (d) are presented in the top row, from left to right. The percent effect size maps generated using SE data from subjects 1 (e), 2 (f), 3 (g) and 4 (h) are presented in the bottom row, from left to right. The color bars indicate the percent effect size values. The slices shown in this figure correspond to those shown in figure 38.

Histograms of the average percent effect size across all subjects in the venous and parenchymal compartments for GRE and SE data are presented on figure 41 for the fMRI experiment involving optimal TEs and on figure 42 for the experiment involving matched TEs. To check for differences between the values acquired using GRE-EPI and SE-EPI, a paired t-test with unequal variances was used and the results for which $p < 0.05$ were considered statistically significant. Group analysis was carried out on subjects 2, 3 and 4 for each BOLD fMRI experiment. Subject 1 was excluded from these analyses as post-hoc investigation of the data revealed that severe clipping of the excitation pulse's waveform occurred, thereby modifying its flip angle. Waveform clipping occurs when the scanner is unable to deliver the necessary voltage to generate a pulse with the correct values of B_1 in order to play it out with an expected flip angle. The maximum voltage capable of being produced by the scanner used for the experiments described in this thesis is equal to 800 volts. To calculate the value of B_{1Max} associated with an RF pulse, the ratio of the voltage used to play out the pulse during a scan session and the reference voltage calculated by the scanner at this time is multiplied by 11.75 μT, the value of B_{1Max} used to play out a rectangular pulse with a flip angle of 180° and a duration of 1 ms with the aforementioned reference voltage. For subject 1, B_{1Max} was found to be equal to 15.76 μT

instead of the expected value of 19.99 μT. Waveform clipping also occurred for subject 3, but the difference between the expected and actual values of B_{1Max} was found to be roughly equal to 0.05 μT, making it possible to use this subject's datasets for group analysis.

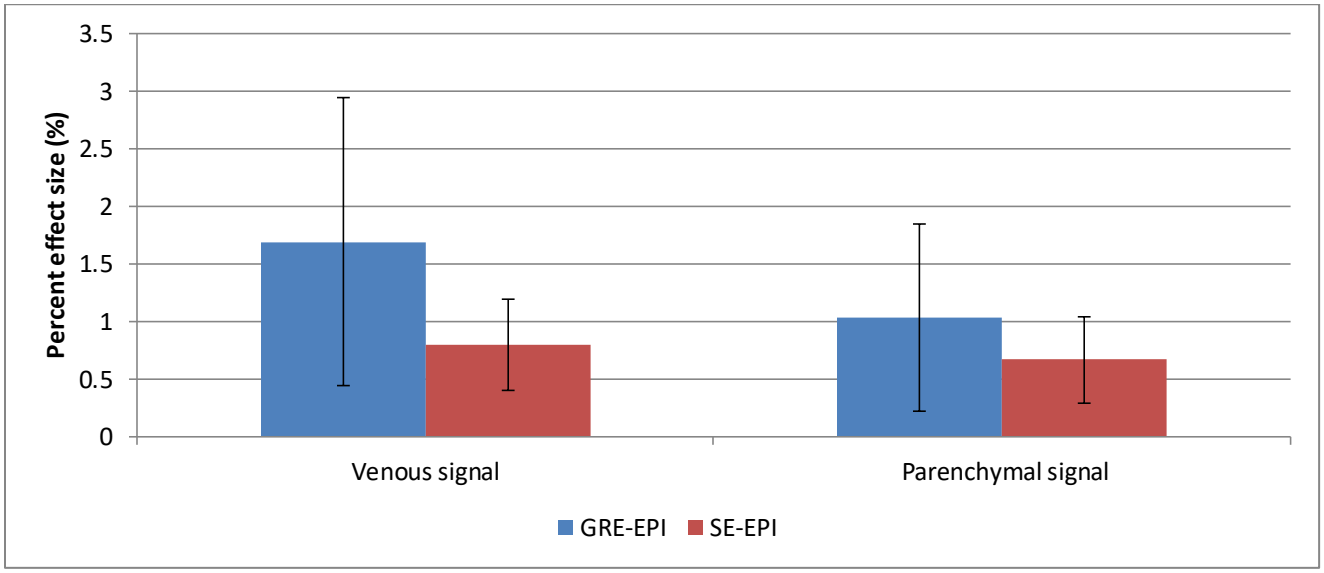

Figure 41: Histogram of the average percent effect size detected in the venous vasculature and parenchymal tissue in a common region of activation for data acquired using GRE-EPI and SE-EPI with the GRESE-EPI pulse sequence using optimal TEs for both acquisition techniques in an fMRI scan involving a visual stimulation paradigm. The error bars represent the standard deviation and data from subjects 2, 3 and 4 were used to compute the average values.

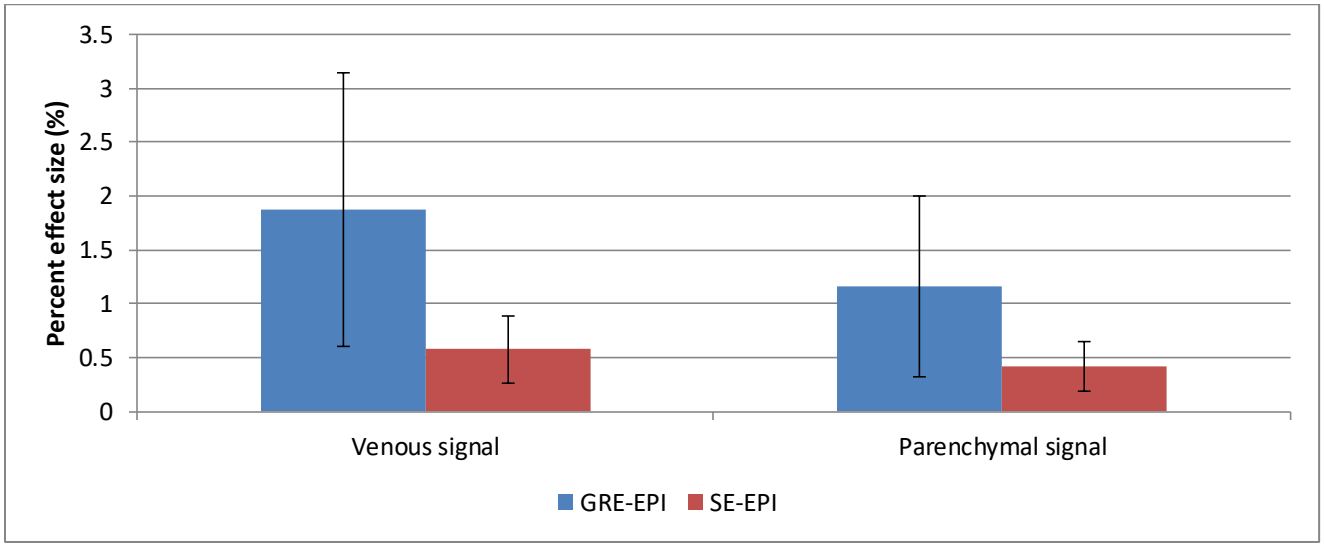

Figure 42: Histogram of the average percent effect size detected in the venous vasculature and parenchymal tissue in a common region of activation for data acquired using GRE-EPI and SE-EPI with the GRESE-EPI pulse sequence using matched TEs for both acquisition techniques in an fMRI experiment involving a visual stimulation paradigm. The error bars represent the standard deviation and data from subjects 2, 3 and 4 were used to compute the average values.

When optimal TEs are used in GRESE-EPI, the average percent effect size in vessels is found to be equal to 1.6917% ± 1.2476% for GRE data while the average percent effect size is equal to 0.7948% ± 0.3996% for SE data. For this same experiment, the average percent effect size in the parenchyma was found to be equal to 1.0384% ± 0.8118% for GRE data and equal to 0.6674% ± 0.3796% for SE data. The results of the paired t-test indicate that these differences are statistically significant, revealing that the percent effect size detected using GRE-EPI in this BOLD fMRI experiment is higher than when SE-EPI is used. Furthermore, it is possible to remark that the values of the effect size are larger in voxels classified as blood vessels in both GRE and SE datasets, which may indicate the intravascular compartment's large contribution to the BOLD signal at a magnetic field strength of B_0 = 3 T. However, only a gross classification of voxels as separate tissues is possible in this work due to the use of voxels presenting a size of 3 mm x 3 mm x 3 mm within the functional datasets, which can result in partial voluming.

A similar result to what was observed for the fMRI experiment conducted using optimal echo times was found when the TE of SE-EPI was lowered to 30 ms. In this experiment, the average percent effect size computed in the veins is equal to 1.8766% ± 1.2672% for images acquired using GRE-EPI and equal to 0.5779% ± 0.3144% for images acquired using SE-EPI. In parenchyma, the average percent effect size was found to be equal to 1.1637% ± 0.8343% for GRE data and equal to 0.4182% ± 0.2302% in SE data. While the values of the SE data obtained in both experiments were not directly compared, lower values of BOLD signal change were expected for SE-EPI experiments carried out with TEs lower than the T2 of brain tissue. (Bandettini *et al*, 1994)

This analysis was also performed on each subject's uncorrected t-maps to check for differences between the average t-score computed in veins and parenchyma for both imaging techniques for all participants. GRE and SE data from subjects 2, 3 and 4 was reused for this purpose and the histograms depicting the average t-score in each compartment for both imaging techniques and experiments are shown in figures 43 and 44.

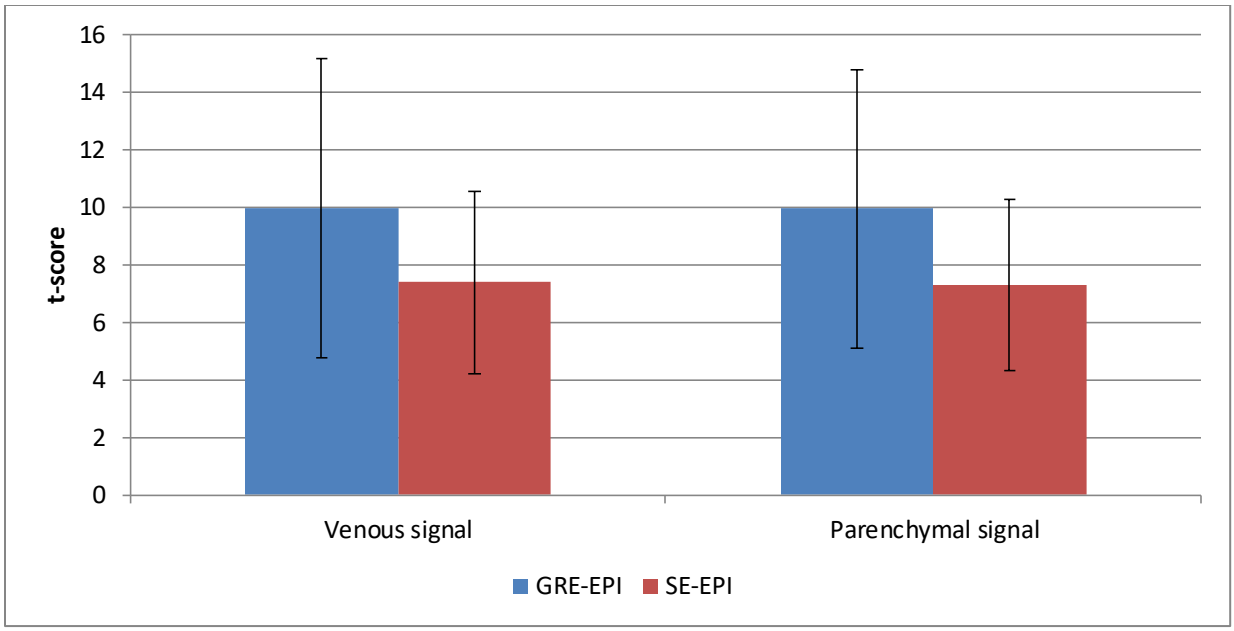

Figure 43: Histogram of the average t-score detected in the venous vasculature and parenchymal tissue in a common region of activation for data acquired using GRE-EPI and SE-EPI with the GRESE-EPI pulse sequence using optimal TEs for both acquisition techniques in an fMRI scan involving a visual stimulation paradigm. The error bars represent the standard deviation and data from subjects 2, 3 and 4 were used to compute the average values.

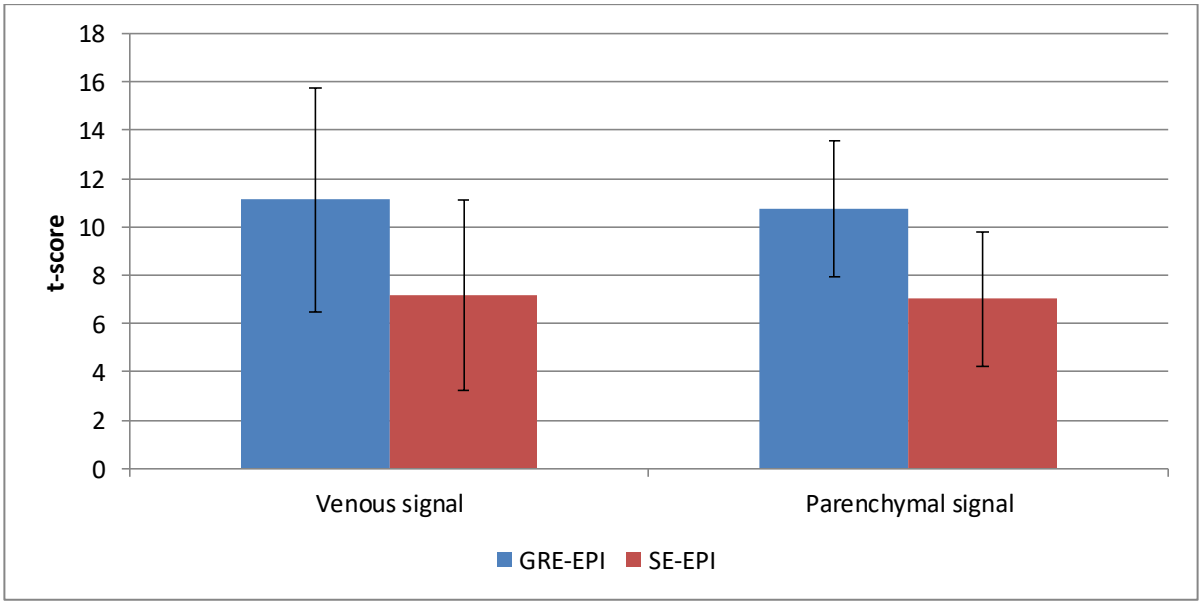

Figure 44: Histogram of the average t-score detected in the venous vasculature and parenchymal tissue in a common region of activation for data acquired using GRE-EPI and SE-EPI with the GRESE-EPI pulse sequence using matched TEs for both acquisition techniques in an fMRI experiment involving a visual stimulation paradigm. The error bars represent the standard deviation and data from subjects 2, 3 and 4 were used to compute the average values.

In venous voxels, the average t-score was found to be equal to 9.9678 ± 5.219 and 7.3847 ± 3.1913 for uncorrected t-maps respectively generated using GRE and SE images obtained during the fMRI experiment involving the use of optimized TEs. In parenchymal voxels, these values were found equal to 9.945 ± 4.8206 and 7.2969 ± 2.9816 for these same GRE and SE datasets. When the TEs for GRESE-EPI's GRE and SE imaging modules were both set to 30 ms, the average t-score computed in venous voxels was found to be equal to 11.1236 ± 4.6199 for data acquired using GRE-EPI and equal to 7.1836 ± 3.9468 for data acquired using SE-EPI. The average t-score calculated in the parenchymal voxels was found to be equal to 10.7464 ± 2.8314 when GRE-EPI was used and equal to 7.0112 ± 2.7527 for data acquired using SE-EPI.

The differences found between the average t-scores originating from the t-maps computed using GRE and SE data were also found to be statistically significant for $p < 0.05$ for both tissue types in both experiments, with the t-scores recorded from regions of activation detected using GRE-EPI being higher than in the SE-EPI activation maps. This is in good agreement with previous findings reported in the literature. (Schmidt *et al,* 2005) However, the average t-scores calculated in the cited study were obtained using pre-determined anatomical regions of interest and not in functional ROIs created using each participant's data. Nevertheless, the average t-scores computed therein were found to be higher in image sets acquired using GRE-EPI, as was the case in this work.

4.2 CBF quantification using two pCASL sequences

Examples of the EPI data acquired using both the in-house and externally-developed pCASL sequences for all 3 subjects are presented on figures 46 and 47 in addition to the CBF maps corresponding to these images.

The individual mean values of whole-brain, gray matter and white matter CBF computed using both pCASL sequences for all three subjects are compiled in table 5. A histogram presenting the group average values of CBF in these three tissue types is presented at figure 45 and the standard deviation is used as the error term. To test for differences between the CBF values acquired using both pCASL sequences, paired t-tests were used on the pooled values of CBF and results for which $p < 0.05$ were considered statistically significant.

Table 5: Table of the average gray matter, white matter and whole-brain CBF in 3 subjects using the pCASL sequence developed in this work and an externally-developed pCASL sequence. The standard deviation is shown here as the error term. These values were obtained using a set of analysis scripts created by Dr. Clément Debacker.

	Subject 1		***Subject 2***		***Subject 3***	
	MNI pCASL	***External pCASL***	***MNI pCASL***	***External pCASL***	***MNI pCASL***	***External pCASL***
Whole brain	56.57 ± 19.51	62.58 ± 23.16	41.55 ± 24.18	44.77 ± 15.04	45.60 ± 16.11	49.02 ± 16.51
Gray matter	65.29 ± 18.15	72.42 ± 22.02	48.50 ± 21.66	52.15 ± 14.71	53.38 ± 16.19	58.21 ± 16.57
White matter	42.48 ± 18.48	46.58 ± 20.41	31.05 ± 17.83	33.76 ± 15.35	34.24 ± 17.44	35.49 ± 18.08

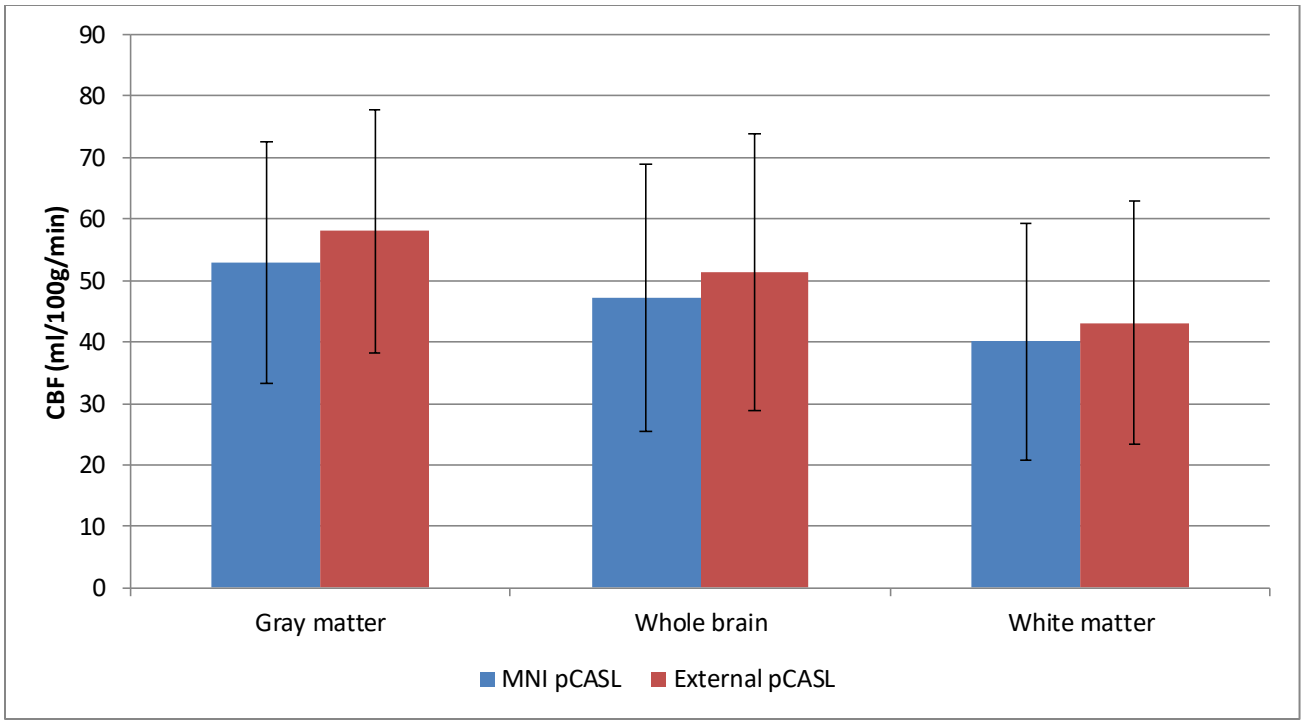

Figure 45: Histogram of the average gray matter, white matter and whole-brain CBF for all 3 subjects computed using data acquired with the in-house (MNI) pCASL sequence and the externally-developed pCASL sequence. The error bars represent the standard deviation.

A statistically significant difference was found for the values of CBF computed using both pCASL techniques in all tissue types, with the CBF values acquired using the externally-developed pCASL sequence being larger than the values computed using the data acquired with the in-house pCASL sequence. Using the pCASL sequence presented in this dissertation, the group average values of CBF were found to be equal to 52.9538 ± 19.6905 ml/100g/min in gray matter and equal to 47.0893 ± 21.7291 ml/100g/min in the brain. For the externally-developed pCASL sequence, gray matter and whole-brain CBF values were found to be equal to 58.0077 ± 19.7751 ml/100g/min and 51.4232 ± 22.4528 ml/100g/min. However, all of these values are situated with the range of physiologically accepted values for both tissue compartments, which are defined as 40 – 100 ml/100g/min in gray matter and 40 – 60 ml/100g/min across the brain. (Mota Nunes, 2015)

The individual and grouped mean values of white matter CBF, the latter of which were found to be equal to 40.0455 ± 19.2673 ml/100 g/min and 43.0477 ± 19.7910 ml/100 g/min for

datasets respectively acquired using the in-house and externally-developed pCASL sequences, were found to be higher than values of white matter CBF commonly reported in the literature, which are approximately equal to 25 ml/100 g/min. (Tinker *et al*, 2012) Other perfusion imaging studies involving the use of pCASL at a magnetic field strength of B_0 = 3 T have reported values of white matter CBF equal to 18.5 – 27.5 ml/100 g/min, (Wu *et al*, 2013)

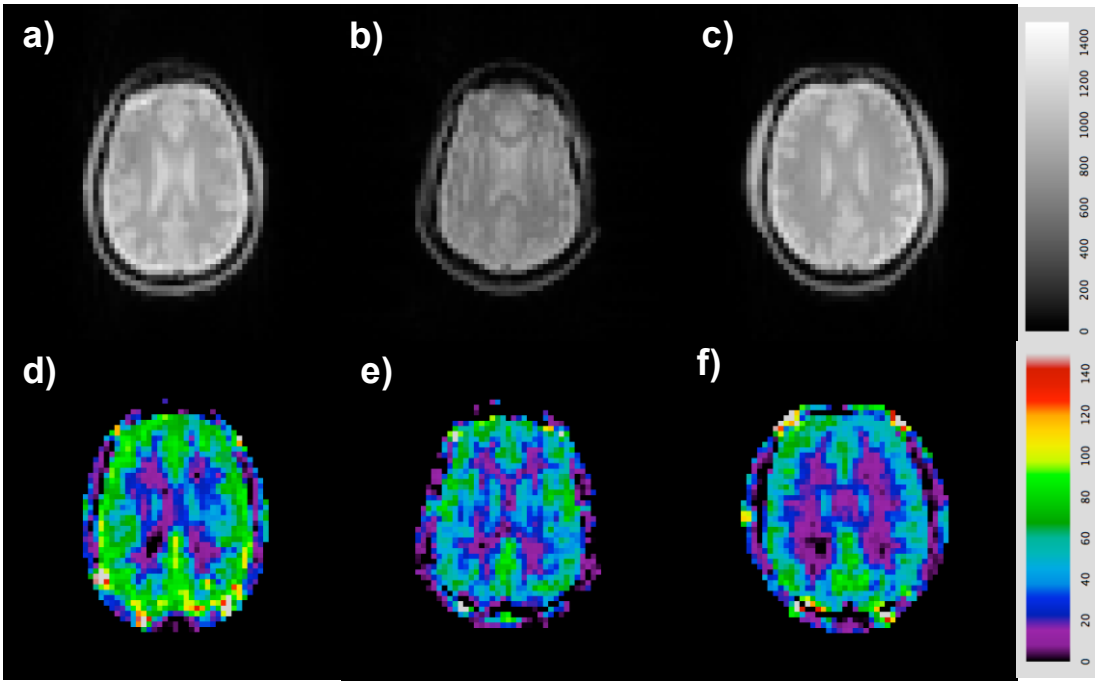

Figure 46: Examples of images acquired using the pCASL sequence developed in this work for 3 subjects (top row) along with the corresponding CBF maps. (bottom row) One pair of images is shown for subjects 1 (a, d), 2 (b, e) and 3 (c, f). The greyscale bars indicate the signal intensity of the EPI data while the color bar indicates the values of CBF in units of ml/100g/min.

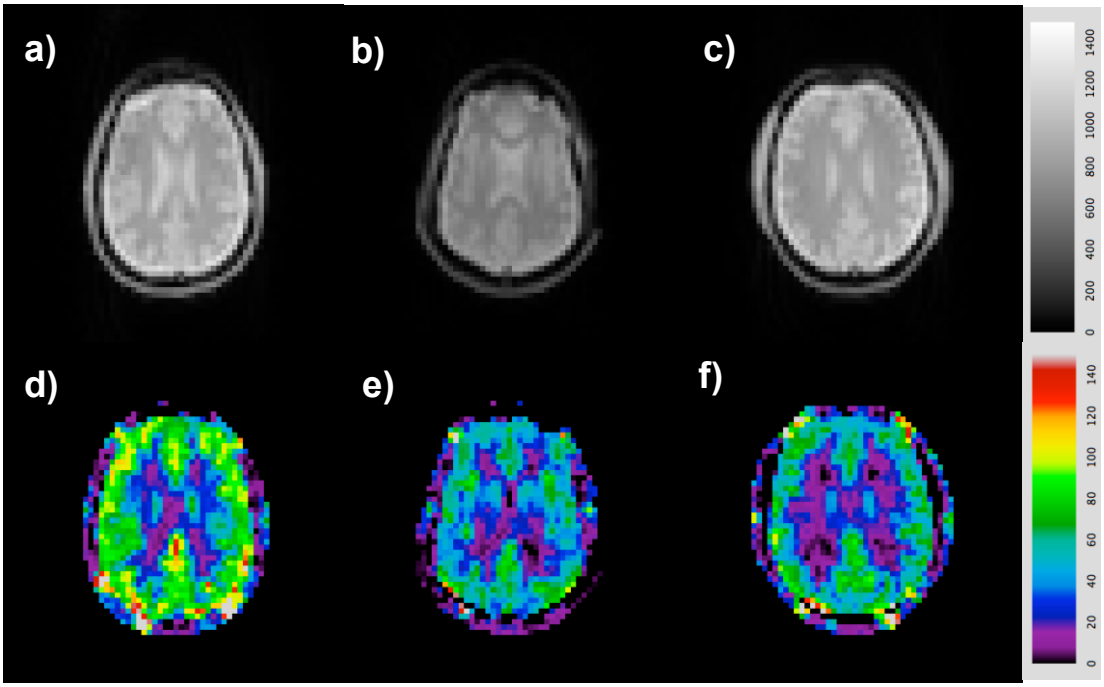

Figure 47: Examples of images acquired using an externally-developed pCASL sequence for 3 subjects (top row) along with the corresponding CBF maps. (bottom row) One pair of images is shown for subjects 1 (a, d), 2 (b, e) and 3 (c, f). The greyscale bars indicate the signal intensity of the EPI data while the color bar indicates the values of CBF in units of ml/100g/min.

Chapter 5. Discussion

5.1 Development of the GRESE-EPI sequence

In this work, an EPI pulse sequence was developed permitting the interleaved acquisition of images while utilizing both GRE- and SE-generating mechanisms during a single scan session. To develop this new pulse sequence, the workings of an SE-EPI sequence were studied to allow its conversion into a GRE-EPI sequence during even-numbered measurement periods while conserving its original functionalities during odd-numbered measurement periods. For this purpose, not only were the timing and polarity of the gradients necessary for signal encoding modified, but a new excitation pulse was also created in MATPULSE using the SLR algorithm to ensure that both the excitation and refocusing pulses would affect the same slice volumes during the scan session.

The slice profile of the newly-created pulse was evaluated using two different Bloch equation simulators and the slice thickness associated with this pulse was empirically measured using a standardized method for quality control in MRI. The latter experiment was also performed to evaluate the slice thickness of the excitation pulse originally incorporated into the SE-EPI sequence used to construct the GRESE-EPI technique. The results of this test have shown that the width of the slice profile associated with the stock excitation pulse was much larger than the expected thickness, making it ill-suited for combined GRE and SE imaging. The SLR pulse, while still presenting a slice profile that is wider than the expected thickness, was found to be 9% larger than the refocusing pulse, rendering it suitable for use in the fMRI experiments described in this work, with the caveat that a gap should be placed between each slice in the image volume.

However, it has been shown in the literature that even excitation and refocusing pulse pairs presenting closely-matched profiles in simulations will have differing thicknesses and become unmatched when used in a scan session due to phenomena that arise at runtime, such as the generation of eddy currents and imperfections related to the scanner's RF amplifier. To offset these problems, a special parameter can be incorporated into the pulse sequence to control the thickness of the slice profile associated with either the excitation or the refocusing pulse independently from the other. Unfortunately, this may not be enough to resolve the problem of

unmatched slice profiles as the nature of the previously-described phenomena may change the shape of the pulse in different ways from one scan to the next. (Schmiedeskamp *et al*, 2012)

While the use of the ACR phantom is a standardized way of measuring the slice thickness in MRI, it can often be difficult to determine the exact locations of the ramps' end-points on the final image. While the ACR recommends that an approximate position be selected to determine the lengths of the ramps and, by proxy, the slice thickness, this can add an amount of user-dependent uncertainty to the measurement, thus compromising its repeatability. An alternative method of measuring the slice thickness should therefore be used to cross-validate the results obtained using the ACR method whenever possible. One other way of measuring the slice thickness involves the use of a pulse sequence modified to play out the RF pulse whose thickness is to be evaluated in a direction orthogonal to the image plane before acquiring the image proper. This will result in the appearance of a saturation band on the image whose width is equal to the slice thickness and can be calculated using a line profile of the image.

Furthermore, while the performance of both excitation pulses was evaluated in terms of the disparity between the expected and actual values of the slice thickness in the ACR experiment, it is also desirable to verify that the excitation and refocusing pulses used in combined GRE/SE imaging techniques possess overlapping slice profiles. This is a helpful method of ascertaining that both pulses will affect similar volumes, despite any differences between the actual and simulated slice profiles at runtime for the reasons outlined previously. (Schmiedeskamp *et al*, 2012) Indeed, the empirical measurements of the slice thickness carried out in this work have provided information only on the width of the slice profiles associated with the excitation pulses as well as the combination of each excitation pulse's slice profile with the refocusing pulse's. This was sufficient for the purposes of the experiments outlined in this thesis, but the method employed herein may not offer a complete picture of the disparity that may exist between the slices profiles associated with the excitation and refocusing RF pulses.

5.2 Comparative analysis of GRE and SE BOLD

The GRESE-EPI pulse sequence developed in this work was used in the context of fMRI experiments involving a sensory stimulus in order to determine the performance of both GRE-

EPI and SE-EPI in terms of their ability to detect signal changes related to neuronal activation in response to the aforementioned stimulus. A block-design trial was devised for this purpose and a flashing black-and-white checkerboard was used to elicit robust activation in the brain's visual cortex. Two fMRI experiments were conducted for this purpose. In the first, a pair of TEs set to the T2 and T2* values of gray matter were respectively used to acquire brain images using SE-EPI and GRE-EPI to maximize BOLD CNR. In the second, these TEs were matched and set to the TE normally used for GRE BOLD imaging at B_0 = 3 T. Activation maps and maps of the effect size expressed as a percentage of the baseline signal were generated using GLM analysis.

Binary masks of the venous vasculature and parenchymal tissue were created by combining the participants' cerebral venograms, created using images acquired during a SWI scan, with subject-specific functional ROIs delineating a common region of activation on the t-maps generated using the GRE and SE datasets for each BOLD fMRI experiment, corrected for FDR with a threshold of 0.001. BOLD signal changes were investigated in voxels determined as belonging to the venous vasculature and parenchymal tissue within this functional ROI. Group averages of the percent effect size and t-scores in both tissue types were subsequently computed for datasets acquired using GRE-EPI and SE-EPI in both fMRI trials. The difference between the average percent effect size and average t-score obtained in each tissue type was found to be superior for datasets acquired using GRE-EPI for both fMRI trials and the difference between these values and those obtained using datasets acquired with SE-EPI has been found to be significant for $p < 0.05$.

While the values here are not directly comparable to findings in the literature due to the use of the percent effect size to assess the strength of BOLD activation instead of a direct measurement of the BOLD percent signal change, the superiority of BOLD signal changes detected using GRE imaging techniques have been documented in the literature, albeit for similar comparative studies carried out at different field strengths and involving different stimuli to elicit neuronal activation. (Schmidt *et al*, 2005; Harmer *et al*, 2012; Budde *et al*, 2014) However, differences between the performances of GRE-EPI and SE-EPI are often reported as z-scores instead of t-scores and the former values have been shown to be 3 times smaller when SE-EPI is used than when GRE-EPI is used in a functional scan. (Norris *et al*, 2002)

The use of subject-specific functional ROIs has been previously reported in the literature in comparative studies seeking to evaluate the difference between the performances of GRE-EPI and SE-EPI in the context of a functional scan. (Bandettini *et al,* 1994; Glielmi *et al*, 2010) To create these functional ROIs, however, it is recommended that a functional localizer scan be conducted ahead of the fMRI trials in order to determine the voxels in which activation in response to a given stimulus is detected in order to create the ROI. (Poldrack *et al,* 2011) By simply selecting the overlapping voxels between two regions of activation, a certain amount of statistical bias can be inserted into the final results. Another method used to confine the region in which the analysis is to be conducted to the same number of voxels is the use of separate statistical thresholds for the correction of activation maps generated using GRE and SE data. (Harmer *et al*, 2012) This is done to take the difference in BOLD CNR between GRE and SE imaging methods into consideration.

Other steps could be taken to improve upon and optimize the BOLD signal analysis process presented in this work, such as the registration of the activation and percent effect size maps to an anatomical template before proceeding with the rest of the analysis. Automatic or semi-automatic segmentation methods could also be employed to generate the thresholded venograms used for tissue-specific BOLD signal analysis. However, due to the downsampling operation performed to be able to use the venogram on the functional datasets, partial voluming will compromise the delineation between tissue voxels and parenchymal voxels made on the processed SWI volumes, which are normally acquired at a higher resolution than the functional scans. As the cerebral cortex possesses a normal thickness of approximately 2 mm, it is reasonable to surmise that voxels with a size of 3 mm x 3 mm x 3 mm classified as "parenchyma" or "gray matter" may also contain blood vessels, white matter and cerebrospinal fluid.

5.3 CBF quantification using two pCASL sequences

In this work, the steps taken to design and develop an ASL sequence featuring a pseudo-continuous tagging mechanism were outlined. To assess the performance of the final product, an experiment was devised to quantify whole-brain, gray matter and white matter CBF in humans at

rest. A second, externally-developed pCASL sequence was also used at this time as a performance benchmark against which the in-house sequence was to be compared in terms of the resulting CBF values. In this experiment, the pCASL sequence originally presented in (Wu *et al,* 2007), whose efficacy in quantifying CBF has been well-documented in the literature, was selected as the benchmark. The results of this experiment have shown that the mean values of gray matter, white matter and whole-brain CBF calculated using data acquired with the in-house pCASL sequence were found to be inferior to those computed using data acquired with the externally-developed pCASL sequence. These differences were found to be significant for $p < 0.05$ for all three tissue types. However, the CBF values derived from data acquired using the in-house pCASL sequence fall within a physiologically-acceptable range of values for gray matter and whole-brain CBF. Values of CBF computed in the white matter are elevated compared to values reported in the literature when using a similar ASL technique at the same magnetic field strength used for the experiments carried out in this thesis.

The differences between the CBF values computed using these two sequences can potentially be ascribed to the design choices that have guided the development of these sequences in addition to the CBF quantification process itself. To construct the tagging unit at the heart of the pCASL sequence presented in this work, certain values selected for the parameters used to design the slice-selection and spoiler gradient lobes, as well as the shape of the tagging pulse, were based on previously-reported values and pulses used for the creation of similar sequences used in perfusion imaging experiments. (Dai *et al*, 2008; Debacker, 2014) However, these parameters may still be optimized to improve the sequence's inversion efficiency. The duration of one peak-to-peak RF pulse cycle, set to 1500 μs in the pCASL sequence presented in this work, could be shortened to a duration that falls below 1 ms as the minimization of this parameter confers upon the sequence increased insensitivity towards resonance frequency offsets at the level of the labelling plane. (Alsop *et al*, 2015) In contrast, the externally-developed pCASL sequence was designed using a peak-to-peak RF pulse duration of approximately 920 μs. Both sequences also make use of Hanning-shaped pulses for the purpose of spin tagging, but differences in their shapes could also account for a potential disparity between the sequences' inversion efficiencies and, consequently, the observed discrepancy between the CBF values computed in each type of brain tissue studied in this work. The amplitude of the slice-selection gradients deployed alongside the tagging pulses also differed

between both pCASL sequences tested in this work; G_{slice} was designed with an amplitude of 9 mT/m in the in-house sequence whereas this parameter was made equal to 6 mT/m in the externally-developed sequence. This design choice could ultimately have repercussions on the tagging process and on the labelling plane itself, resulting in differences between both sequences' inversion efficiencies.

Another salient difference between the two perfusion imaging techniques used in this experiment lies in the mode in which they operate. While the in-house pCASL sequence was designed to operate in the "unbalanced" configuration, its externally-developed counterpart functions as a "balanced" pCASL sequence. As stated previously, the design of both sequence types increases their vulnerability to artifacts or other unwanted effects that can compromise the final CBF measurements. The balanced pCASL sequence's vulnerability to magnetic field inhomogeneity at the level of the labelling plane has been touched upon previously in this work, but the design of an unbalanced pCASL sequence makes this type uniquely susceptible to a number of unwanted effects. Notably, the changes made to G_{spoil} between the tagging and control periods may result in the generation of eddy currents responsible for the apparition of artifacts between both tagged and control image sets, such as shifts in the phase-encoding direction. (Wu *et al*, 2007) In the cited study, however, the unbalanced configuration was achieved by modulating the duration of G_{slice}. It should be stressed at this point that the end goal of this study was not to perform a rigorous comparison between the balanced and unbalanced forms of the pCASL technique, but rather to evaluate the performance of a newly-created perfusion imaging sequence while using a similar sequence which has been widely used in perfusion imaging studies.

Despite the balanced variant's theorized vulnerability to magnetic field inhomogeneity at the level of the labelling plane, studies have shown that the impact of these off-resonance effects are similar in both pCASL types when the unwanted phase shift imparted onto flowing spins does not exceed 90°. (Jung *et al*, 2010) This phase tracking error can still affect a pCASL sequence's inversion efficiency if not controlled for, thereby negatively affecting CBF quantification. Several methods have been proposed to remedy this problem, such as multi-phase pCASL and optimized pCASL. These techniques involve data acquisition using numerous phase offsets in between the tag and control conditions in order to obtain measurements of the phase

tracking errors in each feeding artery and the corrected values of the ASL signal. (Shin *et al*, 2012) In multi-phase pCASL, these evenly-spaced offsets are valued between 0° and 180° and the values of the variables of interest are calculated in a voxel-by-voxel manner by fitting the raw data on an inversion response curve. (Jung *et al*, 2010) Optimized pCASL functions similarly to multi-phase pCASL, but pre-scans, including multi-phase pCASL scans, are used to measure the phase tracking errors at the labelling plane. Modifications such as updating the tagging pulse phase schedule and the implementation of in-plane magnetic field gradients are then made to the pCASL sequence at runtime to correct for these errors, bypassing the post-hoc curve fitting step employed in multi-phase pCASL. (Shin *et al*, 2012)

To establish a better comparison between the CBF values obtained using both pCASL sequences utilized in this work, the inversion efficiency of each perfusion imaging technique must also be calculated. An assumed value of 0.94 was used herein and elsewhere in the literature for CBF quantification in gray matter (Mota Nunes, 2015), but a direct measurement of this parameter is preferable due to the existing imperfections in the scanning environment that may cause this value to deviate from an expected value derived from simulations. In this project, an unreported attempt was made to quantify the labelling efficiency using the method presented in (Aslan *et al,* 2010). This method involves the use of a phase contrast velocity image to first obtain a measurement of CBF by integrating blood flow velocity over the cross-sections of the internal carotids and vertebral arteries in the neck. This value is then equated to an averaged value of whole-brain CBF computed using a standard pCASL scan and the division of these quantities yields the pCASL sequence's inversion efficiency. When this technique was used on the three subjects recruited for the CBF quantification described in section 3.2.1, values of the labelling efficiency approaching or surpassing 100% were obtained, which is not physically possible. Similar values were found in (Aslan *et al*, 2010), indicating that this technique may present a high level of inter-subject variability. Errors in the measurements of the inversion efficiency may also be introduced when selecting the position of the phase contrast velocity image during the scan session, as well as during the creation of the mask of the vessel cross-sections required for the computation of whole-brain CBF derived from values of the blood flow velocity. The sample size used in the cited study was also larger than what was used in this work and 10 subjects were used to estimate the average labelling efficiency, found to be equal to 0.86 ± 0.06 (standard deviation). It would therefore be helpful to develop an alternative technique to

quantify the inversion efficiency for future comparative studies involving the use of the two sequences used in this thesis.

Differences in the individual mean values of CBF in the 3 tissue compartments investigated in this experiment can potentially be ascribed to differences in the position of the labelling plane relative to the AC-PC line. In perfusion imaging studies involving the use of pCASL, it is customary to position this plane below both the circle of Willis and the basilar artery, in a region where the four main feeding arteries, i.e. the internal carotids and vertebral arteries, will be intersected at a right angle, especially when multi-phase or optimized pCASL techniques are used. (Jung *et al*, 2010; Shin *et al*, 2012) However, it has been shown that there exists an optimal position at which the tagging plane can be placed in order to maximize the averaged MRI signal intensity, situated at roughly 84 – 85 mm from the AC-PC line. (Aslan *et al*, 2010) However, empirical examination of the effect of the labelling plane's position on ASL signal has shown that signal intensity values are roughly similar to the optimal values when spin tagging occurs in a region found between 74 and 94 mm below the AC-PC line. (Aslan *et al*, 2010) The difference between the number of slices acquired during subject 1's anatomical scan and the number of slices acquired during subject 2 and subject 3's scans could also have had an impact on CBF quantification and could explain subject 1's elevated CBF values relative to those of the cohort's two other subjects.

It is worth noting that difficulties were encountered when attempting to position the labelling plane during subject 2's scan due to the subject's anatomy. The final placement of the labelling plane was selected in a region where it would intersect one of the feeding arteries, which may have had adverse effects on the spin tagging process. However, the resulting values of CBF are still within normal physiological bounds despite the deactivation of raw filtering when the in-house sequence was used, which could account for the ringing artifacts seen on figure 46b). The relatively high values of white matter CBF, common to all 3 participants, could be due to the choice of the PLD used in this experiment. While a short PLD was used for the experiments conducted for this dissertation, longer durations are recommended to allow the tagged blood to enter the imaging volume and diffuse into brain tissue. Delay times of 500 to 1500 μs have been found to be sufficient to allow the delivery of tagged blood to gray matter, but longer PLDs, on the order of 2 seconds, are recommended for CBF quantification of white

matter or in subjects affected by a vascular pathology. (Alsop *et al*, 2015) Experiments carried out to quantify blood flow in this tissue type using pCASL have made use of PLDs in the range of 1000 to 2200 ms. (Wu *et al*, 2013)

6. Conclusion and future work

In this work, the steps taken to design and develop an EPI sequence allowing for combined GRE and SE imaging as well as a pseudo-continuous arterial spin labelling technique were presented and experiments carried out in BOLD and perfusion fMRI were conducted to assess the performance of both sequences and study the generation of functional contrasts in MRI.

Future experiments carried out using these two sequences will focus on unreported work carried out over the course of this project using additional functionalities incorporated into the previously-described sequences which were not touched upon in this dissertation. The GRESE-EPI presented herein, for example, is also capable of functioning as an asymmetric spin-echo sequence. Using this capability, measurements of the reversible relaxation rate, R2', can be made for gray matter and used in the context of a calibrated fMRI scan in order to retrieve quantitative information on metabolic changes that accompany neuronal activation. (Hoge, 2012; Blockley *et al*, 2013)

A variant of the pCASL sequence presented in this work was also created to acquire images of brain perfusion using multiple values of the PLD. This will allow for the calculation of the arterial transit time, a parameter describing the time necessary for a tagged bolus of blood to reach parenchymal tissue within the brain in an ASL experiment. (Qiu *et al*, 2010) The calculation of this parameter will allow for the optimization of scan protocols used in perfusion imaging studies due to the computation of subject-specific PLD values. In multi-subject studies, the choice of a given PLD may not be optimal for all participants due to variability in each patient's physiology which could lengthen the time necessary for the tagged bolus to reach the imaging slab.

7. References

- M. Bernstein *et al*, *Handbook of MRI Pulse Sequences.* Burlington, MA: Elsevier, 2004
- R. W. Brown *et al*, *Magnetic Resonance Imaging: Physical Principles and Sequence Design,* 2nd edition, Hoboken, NJ: Wiley, 2014
- R. B. Buxton, *Introduction to Functional Magnetic Resonance Imaging*, 2nd edition, New York, NY: Cambridge, 2009
- R. A. Poldrack *et al*, *Handbook of Functional MRI data analysis,* New York, NY: Cambridge, 2011
- D. G. Nishimura, *Principles of Magnetic Resonance Imaging,* edition 1.1, self-published, 2010
- J. L. Prince and J. M. Links, *Medical Imaging: Signals and Systems,* Upper Saddle River, NJ: Prentice Pearson Hall, 2006
- S. A. Huettel *et al*, *Functional Magnetic Resonance Imaging*, 3rd edition, Sunderland, MA: Sinauer, 2014
- E. N. Marieb, *Anatomie et Physiologie humaines,* 3rd edition (translated from English by R. Lachaîne), Saint-Laurent, Québec, Canada : ERPI, 2005
- D. W. McRobbie, *From Picture to Proton,* 1st edition, Cambridge, United Kingdom: Cambridge, 2002
- E. C. Wong *et al,* "Quantitative Imaging of Perfusion Using a Single Subtraction (QUIPSS and QUIPSS II)", *Magn. Reson. Med*., vol. 39, no. 5, pp. 702-8, May 1998
- WM. Luh *et al*, "QUIPSS II with thin-slice TI1 periodic saturation: a method for improving accuracy of quantitative perfusion imaging using pulsed arterial spin labeling", *Magn. Reson. Med.,* vol 41, no. 6, pp. 1246-54, Jun. 1999
- WC. Wu *et al*, "A Theoretical and Experimental Investigation of the Tagging Efficiency of Pseudocontinuous Arterial Spin Labeling", *Magn. Reson. Med.*, vol. 58, no. 5, pp. 1020-27. Nov. 2007
- W. Dai *et al*, "Continuous flow-driven inversion for arterial spin labeling using pulsed radio frequency and gradient fields", *Magn. Reson. Med,* vol. 60, no. 6, pp. 1488-97. Dec. 2008

- H. Jahanian *et al*, "B_0 field inhomogeneity considerations in pseudo-continuous arterial spin labeling (pCASL): effects on tagging efficiency and correction strategy", *NMR Biomed,* vol. 24, no. 10, pp. 1202-9. Dec. 2011

- Y. Jung *et al*, "Multiphase Pseudocontinuous Arterial Spin Labeling (MP-PCASL) for robust quantification of cerebral blood flow", *Magn. Reson. Med*, vol. 64, no. 3, pp. 799-810. Sep. 2010

- D. D. Shin *et al*, "Pseudocontinuous Arterial Spin Labeling with Optimized Tagging Efficiency", *Magn. Reson. Med.,* vol 68, no. 4, pp. 1135-44. Oct. 2012

- F. B. Tancredi *et al*, "Comparison of Pulsed and Pseudocontinuous Arterial Spin-Labeling for Measuring CO_2-Induced Cerebrovascular Reactivity," *J. Magn. Reson. Imaging,* vol. 36, no. 2, pp. 312-21. Aug. 2012

- D. C. Alsop *et al*, "Recommended Implementation of Arterial Spin-Labeled Perfusion MRI for Clinical Applications: A Consensus of the ISMRM Perfusion study group and the European Consortium for ASL in Dementia", *Magn. Reson. Med.*, vol. 73, no. 1, pp. 1-15. Jan. 2015

- P. A. Bandettini *et al*, "Spin-echo and gradient-echo EPI of human brain activation using BOLD contrast: a comparative study at 1.5 T", vol. 7, nos. 1-2, pp. 12-20. Mar. 1994

- SP. Lee *et al*, "Diffusion-weighted Spin-echo fMRI at 9.4 T: Microvascular/Tissue contribution to BOLD signal changes," *Magn Reson. Med.*, vol. 42, no. 5, pp. 919-28. Nov. 1999.

- JM. Oja *et al*, "Venous blood effects in spin-echo fMRI of human brain", *Magn. Reson. Med.,* vol. 42, no. 4, pp. 617-26. Oct. 1999

- D. G. Norris, "An investigation of the value of Spin-Echo-Based fMRI using a Stroop Color-Word Matching task and EPI at 3 T", *NeuroImage,* vol. 15, no. 3, pp. 719-26. Mar. 2002

- SP. Lee, "Comparison of Diffusion-weighted High-resolution CBF and Spin-echo BOLD fMRI at 9.4 T", vol. 47, no. 4, pp. 736-41. Apr. 2002

- T. Q. Duong *et al*, "Microvascular BOLD contribution at 4 and 7 T in the human brain: Gradient-echo and Spin-echo fMRI with suppression of blood effects,", *Magn. Reson. Med.*, vol. 49, no. 6, pp. 1019-27. Jun. 2003

- C. F. Schmidt *et al*, "Comparison of fMRI activation as measured with gradient- and spin-echo EPI during visual activation", *NeuroImage*, vol. 26, no. 3, pp. 852-9. Jul. 2005

- MY Yeh *et al,* "Resolving temporal differences of hemodynamic response with event-related spin-echo BOLD fMRI at 3T: Compating to Gradient-echo BOLD," in *World Congress on Medical Physics and Biomedical Engineering*, Munich, Germany, 2009, pp. 132-4

- C. B. Glielmi *et al*, "Simultaneous acquisition of gradient echo/spin echo BOLD and perfusion with a separate labeling coil," *Magn. Reson. Med.,* vol. 64, no. 6, pp. 1827-31. Dec. 2010

- J. Harmer *et al*, "Spatial location and strength of BOLD activation in high-spatial-resolution fMRI of the motor cortex: a comparison of spin echo and gradient echo fMRI at 7T," *NMR Biomed*, vol. 25, no. 5, pp. 717-25. May 2012

- D. G. Norris, "Spin-echo fMRI: The poor relation?", *NeuroImage*, vol. 62, no. 2, pp.1109-15. Aug. 2012

- J. Budde *et al*, "Functional MRI in human subjects with gradient-echo and spin-echo at 9.4 T," *Magn. Reson. Med.*, vol. 71, no. 1, pp. 209-18. Jan. 2014

- E. M. Haacke *et al*, "Susceptibility weighted imaging (SWI)", *Magn. Reson. Med.*, vol. 52, no. 3, pp. 612-18. Sep. 2004

- C. Denk and A. Rauscher, "Susceptibility Weighted Imaging with Multiple Echoes", *J. Magn. Reson. Imaging,* vol. 31, no. 1, pp. 185-91. Jan. 2010

- M. P. Quinn *et al*, "Comparison of multiecho postprocessing schemes for SWI with use of linear and nonlinear mask functions," *AJNR Am J Neuroradiol*, vol. 35, no. 1, pp. 38-44. Jan 2014

- J. Pauly *et al*, "Parameter relations for the Shinnar-LeRoux Selective Excitation Pulse design algorithm," *IEEE Trans Med Imaging*, vol. 10, no. 1, pp. 53-65. 1991

- G. B. Matson, "An integrated program for amplitude-modulated RF pulse generation and re-mapping with shaped gradients," *Magn. Reson. Imaging,* vol. 12, no. 8, pp. 1205-25. 1994

- G. J. Stanisz *et al*, "T1, T2 relaxation and magnetization transfer in tissue at 3T," *Magn. Reson Med.,* vol. 54, no. 3, pp. 507-12. Sep. 2005

- H. Schmiedeskamp *et al*, "Compensation of slice profile mismatch in combined spin- and gradient-echo echo-planar imaging pulse sequences," *Magn. Reson. Med*, vol. 67, no. 2, pp. 378-88. Feb. 2012

- C. Habas, “Fondements physiologiques de l’IRM fonctionnelle,” *J. Radiol.*, vol. 83, no. 11, pp. 1737-41. Nov. 2002

- K. Uludag *et al*, “Basic principles of functional MRI” in *Clinical Magnetic Resonance Imaging,* 3rd edition, by R. R. Edelman *et al*. Naughton Project Management: England, 2005.

- SG. Kim and P. A. Bandettini, “Principles of Functional MRI” from *Functional MRI*, New York, NY: Springer, 2006, pp. 3-23

- SG. Kim and S. Ogawa, “Biophysical and physiological origins of blood oxygenation level-dependent fMRI signals,” *J Cereb. Blood Flow Metab,* vol. 32, no. 7, pp. 1188-206. Jul. 2012

- R. B. Buxton, “The physics of functional magnetic resonance imaging (fMRI),” *Rep. Prog. Phys,* vol. 76, no. 9, pp.1-30. Sep. 2013

- P. Jezzard and A. Toosey, “Functional MRI” in *MR Imaging of White Matter Diseases of the Brain and Spinal Cord*, M. Filippi *et al*. New York, NY: Springer, 2005

- M. Giannelli *et al,* “Characterization of Nyquist ghost in EPI-fMRI acquisition sequences implemented on two clinical 1.5 T MR scanner systems: effect of readout bandwidth and echo spacing,” *J. Appl. Clin. Med. Phys.*, vol. 11, no. 4, p. 3237. Jul. 2010

- S. Shipp, “Structure and function of the cerebral cortex,” *Curr. Biol.,* vol. 17, no. 12, pp. 443-9. Jun. 2007

- N. Li *et al*, “Quantitative assessment of susceptibility weighted imaging processing methods,” *J. Magn. Reson. Imaging,* vol. 40, no. 6, pp. 1463-1473. Dec. 2014

- S. Eriksson, “A study of susceptibility-weighted MRI including a comparison of two different implementations,” M.S. thesis, Dept. of Medical Radiation Physics, Lund University, Sweden, 2011.

- F. Cacciola *et al*, “Vertebral artery in relationship to C1-C2 vertebrae: An anatomical study,” *Neurol. India*, vol. 52, no. 2, pp. 178-84. Jun. 2004

- S. Faro *et al*, *Functional neuroradiology: Principles and clinical applications*. 1st edition, New York, NY: Springer, 2011

- E. C. Wong, “An introduction to ASL labeling techniques”, *J. Magn. Reson. Imaging,* vol. 40, no. 1, pp. 1-10. Jul. 2014

- R. Ouwerkerk, “Sodium MRI”, *Methods Mol. Biol.*, vol. 711, pp. 175-201. 2011

- J. Ruiz-Cabello, "Fluorine (F^{19}) MRS and MRI in biomedicine", *NMR Biomed*, vol. 24, no. 2, pp. 114-29. Feb. 2011

- J. Papp, *Quality management in the imaging sciences*, 5th edition. Elsevier Health Sciences, 2014.

- *2015 Magnetic Resonance Imaging: Quality control manual*, American College of Radiology, Reston, VA. 2015.

- R. Pohmann *et al*, "Theoretical and experimental evaluation of continuous arterial spin labeling techniques," *Magn. Reson. Med.*, vol. 63, no. 2, pp. 438-46. Feb. 2010

- C. F. Mota Nunes, "Sequence optimization in pseudo-continuous arterial spin labeling," M.S. thesis, Faculty of Sciences and Technology, University of Coimbra, Portugal, 2015.

- J. Wang *et al*, "Arterial transit time imaging with flow encoding Arterial Spin Tagging," *Magn. Reson. Med.,* vol. 50, no. 3, pp. 599-607. Sep. 2003

- J. Chen and B. Pike, "BOLD-specific cerebral blood volume and blood flow changes during neuronal activation in humans," *NMR Biomed,* vol. 22, no. 10, Dec. 2009

- F. B. Tancredi *et al*, "Test–retest reliability of cerebral blood flow and blood oxygenation level-dependent responses to hypercapnia and hyperoxia using dual-echo pseudo-continuous arterial spin labeling and step changes in the fractional composition of inspired gases," *J. Magn. Reson. Imaging*, vol. 42, no. 2, pp. 1144-57. Oct. 2015

- M. S. Shiroishi *et al*, "Principles of T2*-weighted dynamic susceptibility contrast MRI technique in brain tumor imaging," *J. Magn. Reson. Imaging*, vol. 41, no. 2, Feb 2015.

- G. Duhamel *et al*, "Pseudocontinuous Arterial Spin Labeling (pCASL) at very high field (11.75 T) for mouse brain perfusion imaging," *Proceedings of the international society for magnetic resonance in medicine,* Montréal, Québec, Canada, 2011, p. 371

- YJ Kim and TC Mamisch, *Hip Magnetic resonance imaging*, 1st edition. Springer, 2013

- T. T. Liu and G. G. Brown, "Measurement of cerebral perfusion with arterial spin labeling: Part 1. Methods", *Neuropsychol. Soc.,* vol. 13, no. 3, pp. 517-25. May 2007

- L. Zhao *et al*, "Reduced Field-of-View MRI With Two-Dimensional Spatially-Selective RF Excitation and UNFOLD," *Magn. Reson. Med,* vol. 53, no. 5, pp. 1118-25. May 2005

- R. A. de Graaf, *In vivo NMR Spectroscopy: Principles and techniques,* 2nd edition.

- L. Pauling and C. D. Coryell, "The magnetic properties and structure of hemoglobin, oxyhemoglobin and carbonmonoyhemoglobin," *Proc. Natl. Acad. Sci. U.S.A.,* vol. 22, no. 4, pp. 210-16. Apr. 1936

- J. Pauly, "The art of RF pulse design for MRS," *Proceedings of the international society for magnetic resonance in medicine,* Seattle, WA, USA, 2006.

- B. Sabouri, "Dynamic magnetic resonance spectroscopy of phosphate energetics during muscle exercise and recovery," M.S. thesis, Faculty of Biomedical Engineering, Université de Montréal, Montréal, Québec, Canada, 2014

- A. Berman, "Development of a functional magnetic resonance imaging simulator: Deterministic simulation of the transverse magnetization in microvasculature," M.S. thesis, Medical Physics unit, McGill University, Montréal, Québec, Canada, 2012

- G. K. Yang, "Computing Magnetic Susceptibility Maps from Gradient recalled echo MRI for use in multiple sclerosis studies," M.S. thesis, Dept. of Electrical and Computer Engineering, Ohio State University, Columbus, OH, USA, 2013

- R. Grubb *et al*, "The effects of changes in $PaCO_2$ cerebral blood volume, blood flow, and vascular mean transit time," *Stroke,* vol. 5, pp. 630-9, 1974

- P. T. Fox and M. E. Raichle, "Focal physiological uncoupling of cerebral blood flow and oxidative metabolism during somatosensory stimulation in human subjects," *Proc. Natl. Acad. Sci. U.S.A,* vol. 83, no. 4, pp. 1140-4

- D. A. Yablonskiy and E. M. Haacke, "Theory of NMR signal behavior in magnetically inhomogeneous tissues: the static dephasing regime," *Magn. Reson. Med.*, vol 32, no. 6, pp. 749-63. Dec. 1994

- R. B. Buxton *et al,* "A General Kinetic Model for Quantitative Perfusion Imaging with Arterial Spin Labeling," *Magn. Reson. Med.,* vol. 40, no. 3, pp. 383-96. Sep. 1998

- C. Debacker, "Développement de l'imagerie de perfusion cérébrale par marquage des spins artériels," Ph.D. thesis, École doctorale de physique, Université de Grenoble, Grenoble, France, 2014

- PG. Henry, "Spectroscopie RMN *in vivo* du cerveau à 3 Tesla : développements méthodologiques pour l'étude de modèles animaux de la maladie de Huntington," Ph.D. thesis, Spécialité : Neurosciences, Université de Paris 6, Paris, France, 2000

- O. C. Andronesi *et al,* "Low-power adiabatic sequences for in-vivo localized two-dimensional chemical shift correlated MR spectroscopy," *Magn. Reson. Med.,* vol. 64, no. 6, pp. 1542-56. Dec. 2010

- J. M. Pollock, "Arterial Spin Labeled MRI Perfusion Imaging: Clinical Applications," *Magn. Reson. Imaging Clin. N. Am,* vol. 17, no. 2, pp. 315-338. May 2009

- R. A. Lerski, "An evaluation using computer simulation of two methods of slice profile determination in MRI," *Phys. Med. Biol.,* vol. 34, no. 12, pp. 1931-37, 1989

- S. Aslan *et al*, "Estimation of labeling efficiency in pseudocontinuous arterial spin labeling," *Magn. Reson. Med.*, vol. 63, no. 3, pp. 765-71. Mar. 2010

- E. F. Jackson, "Acceptance testing for quality assurance procedures for magnetic resonance imaging facilities," AAPM, Alexandria, VA, USA, AAPM report No. 100, Dec. 2010

- J. L. Boxerman, "The intravascular contribution to fMRI signal change: Monte Carlo modeling and diffusion-weighted studies in vivo," *Magn. Reson. Med.,* vol. 34, no. 1, pp. 4-10, Jul. 1995

- S. Ogawa *et al*, "Functional brain mapping by blood-oxygenation level-dependent contrast magnetic resonance imaging," *Biophys. J.,* vol. 64, no. 3, pp. 803-12, Mar. 1993

- J. Tinker and W. Zapol, *Care of the critically-ill patient*, 2nd edition. Springer Science & Business Media, 2012

- WC. Wu *et al*, "Measurement of cerebral white matter perfusion using pseudocontinuous arterial spin labeling 3T Magnetic Resonance Imaging – an experimental and theoretical investigation of feasibility," *PLoS One,* vol. 8, no. 12, pp. 1-12. Dec. 2013

- J. A. Detre, "Arterial Spin Labeled Perfusion MRI," *MAGNETOM Flash,* issue 38, pp. 6-9. Apr. 2008

- M. Qiu *et al*, "Arterial transit time effects in pulsed arterial spin labeling CBF mapping: insight from a PET and MR study in normal human subjects," *Magn. Reson. Med.*, vol. 63, no. 2, pp. 374-384. Feb. 2010

- R. D. Hoge, "Calibrated fMRI," *Neuroimage*, vol. 62, no. 2, pp. 930-7. Aug. 2012

- N. P. Blockley *et al*, "A review of calibrated blood oxygenation level-dependent (BOLD) methods for the measurement of task-induced changes in brain oxygen metabolism," *NMR Biomed,* vol. 26, no. 8, pp. 987-1003. Aug. 2013

- *Advanced Design System 1.5: Digital Filter Designer*, Agilent Technologies, Santa Clara, CA, pp. 4-1, 4-31. Dec. 2000

- D. C. Swanson, *Signal Processing for Intelligent Sensor Systems with MATLAB®,* 2nd edition, Boca Raton, FL: CRC Press, 2011.

- [1]: By Interiot – Neuron.svg, CC BY-SA 3.0, https://commons.wikimedia.org/w/index.php?curid=1474927 (Sourced on August 31st 2016)

- [2]: By OpenStax College - Anatomy & Physiology, Connexions Web site. http://cnx.org/content/col11496/1.6/, Jun 19, 2013., CC BY 3.0, https://commons.wikimedia.org/w/index.php?curid=30148272 (Sourced on August 31st 2016)

- [3]: By Rhcastilhos - Gray519.png, Public Domain, https://commons.wikimedia.org/w/index.php?curid=1597012 (Sourced on August 31st 2016)